SOL-GEL SYNTHESIZED NANOMATERIALS FOR ENVIRONMENTAL APPLICATIONS

by

XIANGXIN YANG

B. Sc., University of Petroleum, Beijing, China, 1998

M. S., Research Institute of Petroleum Processing, Beijing, China, 2001

AN ABSTRACT OF A DISSERTATION

Submitted in partial fulfillment of the requirements for the degree

DOCTOR OF PHILOSOPHY

Department of Chemical Engineering

College of Engineering

KANSAS STATE UNIVERSITY

Manhattan, Kansas

2008

Abstract

Over the past decade, nanomaterials have been the subject of enormous interest. Their defining characteristic is a very small size in the range of 1-100 nm. Due to their nanometer size, nanomaterials are known to have unique mechanical, thermal, biological, optical and chemical properties, together with the potential for wide-ranging industrial applications. Here, we synthesized nanocrystalline metal oxides through the sol-gel process and used these materials as desulfurization adsorbents and photocatalysts.

Deep desulfurization of fuels has received more and more attention worldwide, not only because of health and environmental consideration but also due to the need for producing ultra-low-sulfur fuels, which can only be achieved under severe operating conditions at high cost using hydrodesulfurization (HDS). Consequently, development of new and affordable deep desulfurization processes to satisfy the decreasing limit of sulfur content in fuels is a big challenge. Sol-gel derived Cu/Al_2O_3 and Zn/Al_2O_3 adsorbents have been demonstrated to be effective in the removal of thiophene from a model solution. Results showed that Cu^+ was the active site and thermal treatment under vacuum was critical for Zn/Al_2O_3 since a defective, less crystalline spinel led to stronger interaction between zinc ions and thiophene molecules in the adsorption process. The kinetic study suggested that most of the adsorption occurred in the first 30 min, and adsorption equilibrium was attained after 1.5 h. Both adsorbents showed good regenerative property.

TiO_2 is considered the most promising photocatalyst due to its high efficiency, chemical stability, non-toxicity, and low cost for degradation and complete mineralization of

organic pollutants. However, the use of TiO_2 is impaired because it requires ultraviolet (UV) activation (λ<387 nm). The shift of optical response of TiO_2 from the UV to the visible light region would have a profound positive effect on the efficient use of solar energy in photocatalytic reactions. We shifted the optical response of TiO_2 and improved the photocatalytic efficiency through size modification and transition metal ion and nonmetal atom doping. Experimental results showed that C and V co-doped TiO_2 catalysts had much higher activity than commercial P25 TiO_2 towards the degradation of acetaldehyde under visible light irradiation. For the first time, we reported that activities were comparable in the dark and under visible light irradiation for co-doped TiO_2 with 2.0 wt% V. C and N co-doped TiO_2 exhibited higher activity for the degradation of methylene blue than pure TiO_2 under visible light and UV irradiation. Possible mechanisms were discussed based on the experimental results.

SOL-GEL SYNTHESIZED NANOMATERIALS FOR ENVIRONMENTAL APPLICATIONS

by

XIANGXIN YANG

B. Sc., University of Petroleum, Beijing, China, 1998

M. S., Research Institute of Petroleum Processing, Beijing, China, 2001

A DISSERTATION

Submitted in partial fulfillment of the requirements for the degree

DOCTOR OF PHILOSOPHY

Department of Chemical Engineering

College of Engineering

KANSAS STATE UNIVERSITY

Manhattan, Kansas

2008

Approved by:

Major Professor
Dr. Larry E. Erickson

Copyright

XIANGXIN YANG

2008

Abstract

Over the past decade, nanomaterials have been the subject of enormous interest. Their defining characteristic is a very small size in the range of 1-100 nm. Due to their nanometer size, nanomaterials are known to have unique mechanical, thermal, biological, optical and chemical properties, together with the potential for wide-ranging industrial applications. Here, we synthesized nanocrystalline metal oxides through the sol-gel process and used these materials as desulfurization adsorbents and photocatalysts.

Deep desulfurization of fuels has received more and more attention worldwide, not only because of health and environmental consideration but also due to the need for producing ultra-low-sulfur fuels, which can only be achieved under severe operating conditions at high cost using hydrodesulfurization (HDS). Consequently, development of new and affordable deep desulfurization processes to satisfy the decreasing limit of sulfur content in fuels is a big challenge. Sol-gel derived Cu/Al_2O_3 and Zn/Al_2O_3 adsorbents have been demonstrated to be effective in the removal of thiophene from a model solution. Results showed that Cu^+ was the active site and thermal treatment under vacuum was critical for Zn/Al_2O_3 since a defective, less crystalline spinel led to stronger interaction between zinc ions and thiophene molecules in the adsorption process. The kinetic study suggested that most of the adsorption occurred in the first 30 min, and adsorption equilibrium was attained after 1.5 h. Both adsorbents showed good regenerative property.

TiO_2 is considered the most promising photocatalyst due to its high efficiency, chemical stability, non-toxicity, and low cost for degradation and complete mineralization of

organic pollutants. However, the use of TiO_2 is impaired because it requires ultraviolet (UV) activation (λ<387 nm). The shift of optical response of TiO_2 from the UV to the visible light region would have a profound positive effect on the efficient use of solar energy in photocatalytic reactions. We shifted the optical response of TiO_2 and improved the photocatalytic efficiency through size modification and transition metal ion and nonmetal atom doping. Experimental results showed that C and V co-doped TiO_2 catalysts had much higher activity than commercial P25 TiO_2 towards the degradation of acetaldehyde under visible light irradiation. For the first time, we reported that activities were comparable in the dark and under visible light irradiation for co-doped TiO_2 with 2.0 wt% V. C and N co-doped TiO_2 exhibited higher activity for the degradation of methylene blue than pure TiO_2 under visible light and UV irradiation. Possible mechanisms are discussed based on the experimental results.

Table of Contents

List of Figures

List of Tables

Acknowledgements

I would like to express my deepest appreciation to my advisors, Dr. Larry Erickson and Dr. Kenneth Klabunde, without whom I would never have made it this far. Their support, patience, and understanding are invaluable. Under their guidance, I was given the freedom to do the research in my own way and I greatly appreciated that freedom.

I am profoundly grateful to all my colleagues in Dr. Klabunde's research group who provided a friendly environment to work and study, Dr. Jeevanandam Pethaiyan, Dr. Ranjit Koodali, Dr. Shalini Rodriguez, Dr. Alexander Smetana, Dr. Johanna Haggstrom, Zhiqiang Yang, Yen-Ting Kou, Luther Mahoney, Sreeram Cingarapu, Erin Beavers, Dambar Hamal. I am particularly grateful to Dr. Jeevanandam Pethaiyan for his invaluable help and discussion about desulfurization experiments and other subjects.

Dr. Keith Hohn, Dr. Ronaldo Maghirang, and Dr. Bruce Law are gratefully acknowledged for taking time to serve on my PhD committee. Dr. Hohn and Dr. Maghiring are thanked for their time and effort spent proofreading manuscripts and for their valuable suggestions and comments.

To my wife Chundi, who did the XPS and IR analysis and has always supported me. Her love, patience, and help during the past few years have been determinant for the good

development of my work. For her valuable suggestions and comments during the preparation of this manuscript, my deepest gratitude!

The financial support from the Army Research Office, NanoScale Corporation, and Targeted Excellence Program at Kansas State University is gratefully appreciated.

Preface

Environmental pollution and damage on a global scale have drawn much attention to clean chemical technologies, materials, and processes. This research contributes to the study and development of new nanomaterials by sol-gel processes for environmental protection. Namely, nanocrystalline metal oxides are investigated as adsorbents for fuel desulfurization and as photocatalysts for the degradation of pollutants in air and water.

There are seven chapters. The first chapter begins with the sol-gel process, including sol-gel chemistry, advantages, and applications. The second chapter is an overview of desulfurization technologies. Chapter three and Chapter four describe Cu/Al_2O_3 and Zn/Al_2O_3 adsorbents, respectively. Each chapter is arranged along the following lines: synthesis of adsorbents, adsorptive desulfurization experiments, adsorbent characterization, mechanistic study, and adsorbent regeneration. In Chapter five, photocatalysis on TiO_2 is reviewed, including the photocatalytic process, characteristics of TiO_2 catalyst, methods to improve photocatalytic efficiency, and modifications to shift the optical response of TiO_2 from ultraviolet (UV) to the visible light region. Transition metal ion (V) and nonmetal atom (C) doped TiO_2 is the subject of Chapter six. Chapter seven describes nonmetal atoms (C and N) doped TiO_2. Specific details of synthesis, characterization, and photocatalytic experiments are discussed in these two chapters.

The content of this research is partially published:

Xiangxin Yang, Chundi Cao, Larry Erickson, Keith Hohn, Renaldo Maghirang, Kenneth Klabunde. “Synthesis of visible-light-active TiO_2-based photocatalysts by carbon and nitrogen doping”, *Journal of Catalysis*, submitted.

Xiangxin Yang, Chundi Cao, Larry Erickson, Keith Hohn, Renaldo Maghirang, Kenneth Klabunde. “Highly visible light active C-, V-doped TiO_2 catalyst for the degradation of acetaldehyde”, *Journal of Catalysis* 2007, 252(2), 296-302

Xiangxin Yang, Chundi Cao, Kenneth Klabunde, Keith Hohn, Larry Erickson. “Adsorptive desulfurization with xerogel derived zinc-based nanocrystalline aluminum oxide”, *Industrial & Engineering Chemistry Research* 2007, 46(14), 4819-4823

Xiangxin Yang, Keith Hohn, Larry Erickson, P. Jeevanandam, Kenneth Klabunde. “Sol-gel Cu-Al_2O_3 adsorbent for selective adsorption of thiophene out of hydrocarbon”, *Industrial & Engineering Chemistry Research* 2006, 45(18), 6169-6174

CHAPTER 1 Sol-gel Process

1.1 Introduction

The sol-gel process, which is reviewed in this chapter, has become a widely used method during the last several decades. Basically the sol-gel process designates a type of solid materials synthesis procedure by chemical reactions in a liquid at low temperature.[1] In a typical sol-gel process, independent solid colloidal particles ranging from 1 nm to 1 micrometer are formed from the hydrolysis and condensation of the precursors, which are usually inorganic metal salts or metal organic compounds such as metal alkoxides. It is usually easy to maintain such particles in a dispersed state in the solvent, in which case a colloidal suspension also termed a sol is obtained. In the second step, these colloidal particles can be made to link with each other by further sol condensation, while they are still in the solvent, so as to build a three-dimensional open grid, termed gel.[1] The transformation of a sol to a gel constitutes the gelation process.

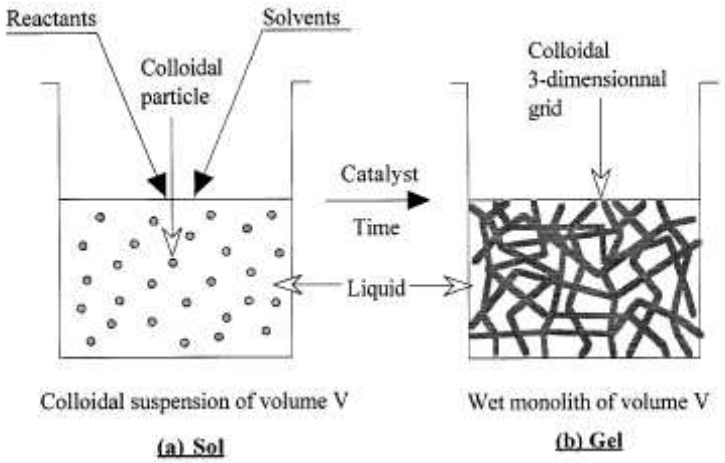

Figure 1.1 The sol-gel process[1]

1.2 Sol-gel chemistry

Sol-gel chemistry is based on the hydrolysis and condensation of precursors. Most work in the sol-gel field has been performed by the use of alkoxides as precursors. Alkoxides provide a convenient source for “inorganic” monomers which in most cases are soluble in a variety of solvents, especially alcohol. Alcohols enable a convenient addition of water to start the reaction. Another advantage of the alkoxide route is the possibility to control rates by controlling hydrolysis and condensation by chemical means.[2] With an alkoxide as a precursor, sol-gel chemistry can be simplified in terms of the following reaction equations.[3]

(1) Hydrolysis (hydroxylation) of metal alkoxides:

$$-M-OR + H_2O \longrightarrow -M-OH + ROH$$

As shown in Figure 1.2, the mechanism involves nucleophilic attack of a negatively charged $HO^{\delta-}$ group onto a positively charged metal $M^{\delta+}$ and transfer of a proton from the water to a negatively charged OR group of the metal and release of the resulting ROH molecule. As soon as reactive hydroxyl groups are obtained, the formation of branched oligomers and polymers with a metal oxo based skeleton and reactive residual hydroxo and alkoxy groups occurs through a polycondensation process.

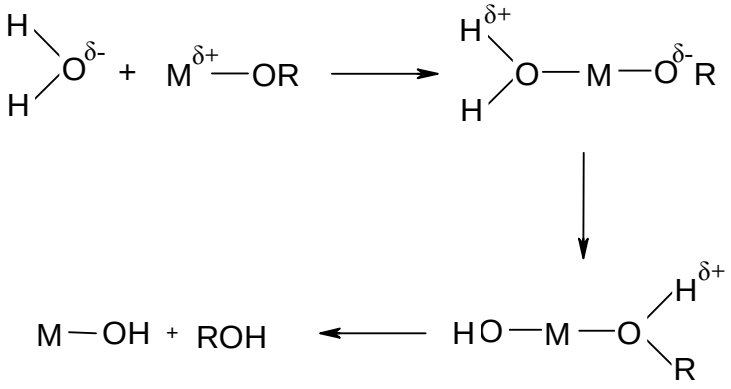

Figure 1.2 The hydrolysis of alkoxide in sol-gel process[3]

(2) Condensation:

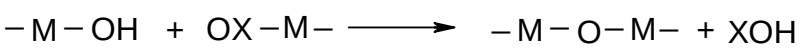

In this case X means either an H or R (an alkyl group). Oxolation is also a three step nucleophilic substitution reaction which occurs through the elimination of H_2O or ROH. Generally, under a stoichiometric hydrolysis ratio ($H_2O/M < 2$), the alcohol producing condensation is favored, whereas the water forming condensation is favored for large hydrolysis ratios ($H_2O/M >> 2$).

The hydrolysis and condensation are responsible in the transformation of metal alkoxide precursors to a metal oxo macromolecular network. The recombination of these metal oxo polymers leads to the production of well dispersed structures which occupy the whole volume. When these oxo polymers reach macroscopic sizes, the reaction bath becomes a gel, inside which, the solvent, reaction byproducts and free polymer are trapped. If the polymerized structures do not reach macroscopic sizes, sols are produced. Precipitates are formed if the reactions produce dense rather well dispersed structures.[4,5]

1.3 Transformation of wet gel

A general flowchart for a complete sol-gel process is shown in Figure 1.3.[1,6] A gel forms because of the condensation of hydrolyzed species into a three-dimensional polymeric network. Any factor that affects either or both of these reactions is likely to impact the properties of the gel. These factors, generally referred to as sol-gel parameters, includes type of precursor, type of solvent, water content, acid or base content, precursor concentration, and temperature.[7] These parameters affect the structure of the initial gel and, in turn, the properties of the material at all subsequent processing steps. After gelation, the wet gel can be optionally aged in its mother liquor, or in another solvent, and washed. The time between the formation of a gel and its drying, known as aging, is also an important parameter. A gel is not static during aging but can continue to undergo hydrolysis and condensation.[8] Furthermore, syneresis, which is the expulsion of solvent due to gel shrinkage, and coarsening, which is the dissolution and reprecipitation of particles, can occur. These phenomena can affect both the chemical and structural properties of the gel after its initial formation. Then it must be dried to remove the solvent.

Table 1-1 showed a summary of the key steps in a sol-gel process which includes the aim of each step along with experimental parameters that can be manipulated.

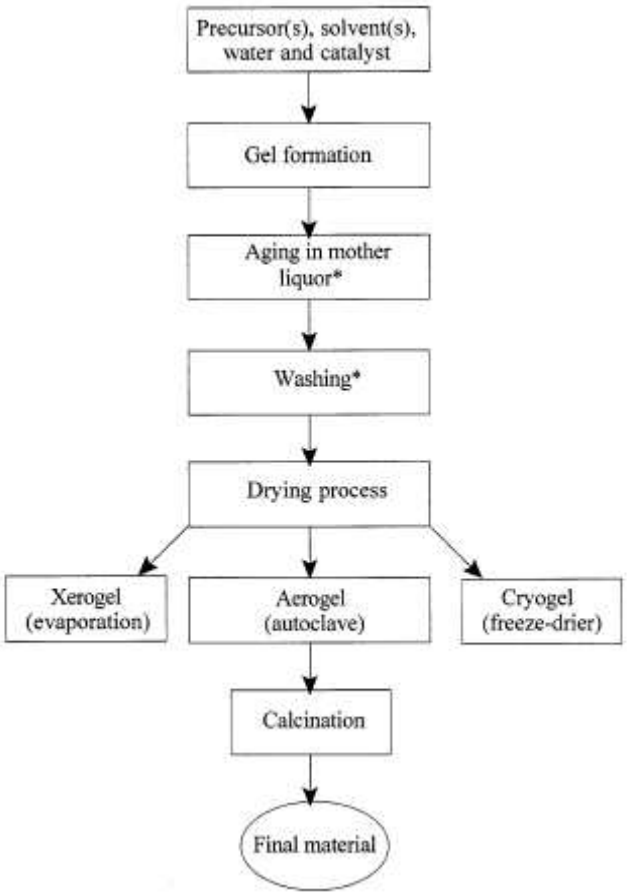

Figure 1.3 Sol-gel and drying flowchart (* the aging and washing steps are optional) [1,6]

Table 1-1 Important parameters in the various steps of a sol-gel process[1,2,3,4,5]

Step	Purpose	Important parameters
Solution chemistry	To form gel	Type of precursor; Type of solvent; Water content; Precursor concentration; Temperature; pH
Aging	To allow a gel to undergo changes in properties	Time; Temperature; Composition of the pore liquid; Aging environment;
Drying	To remove solvent from a gel	Drying method (evaporative, supercritical, and freeze drying); Temperature and heating rate; Pressure and pressurization rate; Time;
Calcination	To change the physical/chemical properties of the solid, often resulting in crystallization and densification	Temperature and heating rate; Time; Gaseous environment (inert, reactive gases);

1.3.1 Aerogel

One important parameter that affects a sol-gel product is the drying condition. Due to the surface tension of the liquid, a capillary pressure gradient is present in the pore walls and this may be able to collapse most of the pore volume when solvent is removed. One convenient way to avoid pore collapse is to remove the liquid from the pores above the

critical temperature (Tc) and critical pressure (Pc) of the fluid, namely, supercritical drying.[1,4] Under supercritical conditions, there is no longer a distinction between the liquid and vapor phases: the densities become equal; there is no liquid-vapor interface and no capillary pressure. This type of drying prevents the formation a liquid-vapor meniscus which recedes during the emptying of the pores in the wet gels. The resulting dried gel, called an aerogel, has a pore volume similar to that of the wet gel.[1]

Practically, supercritical drying consists of heating the wet gel in a closed container, so that the pressure and temperature exceed the critical temperature, *T*c, and critical pressure, *P*c, of the liquid entrapped in the pores inside the gel.

The critical conditions are very different depending on the fluid which impregnates the wet gel. Table 1-2 contains values of T_c and P_c for several fluids.[4] Presently, one distinguishes high-temperature supercritical drying (or HOT) in alcohol from low temperature supercritical drying (COLD) in CO_2.[1] Both methods are different in the sense that the hot method is accompanied by a kind of a rather poorly controlled aging process during the temperature and pressure increase used to attain the chosen supercritical conditions. The resulting materials thus are generally hydrophobic since their surfaces are covered by alkoxy groups. On the other hand, the cold method does not favor such processes, and as a consequence, it leads to more hydrophilic solids.[1] A possible supercritical drying path in the phase diagram of CO_2 is presented in Figure 1.4, the pressure and temperature are increased in such a way that the phase boundary is not

crossed; once the critical point is passed, the solvent is vented at constant temperature (>Tc).

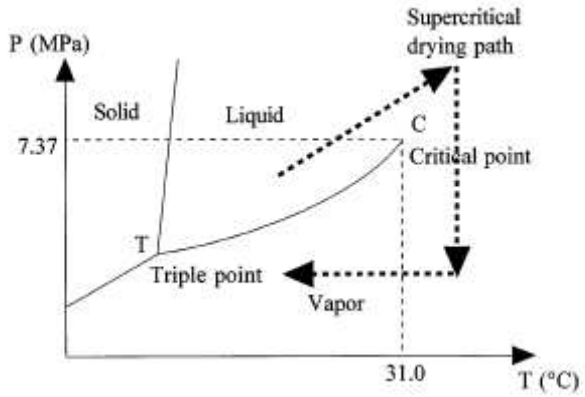

Figure 1.4 Example of a possible drying path in the pressure (P) Temperature (T) phase diagram of CO_2[1]

Table 1-2 Critical point parameters of common fluids[4]

Substance	formula	T_c (ºC)	P_c (MPa)
Carbon dioxide	CO_2	31.0	22.04
Water	H_2O	374.1	7.37
Acetone	$(CH_3)_2CO$	235.0	4.66
Methanol	CH_3OH	239.4	8.09
Ethanol	CH_3CH_2OH	243.0	6.3

1.3.2 Xerogel

Conventional evaporative drying induces capillary pressure associated with the liquid-vapor interface within a pore, causing shrinkage of the gel network. In a sample with a

distribution of pore sizes, the resultant differential capillary pressure often collapses the porous network during drying. The dried sample often has low surface area and pore volume.

Surfactants can be added to the liquid to decrease the capillary stresses. It has been reported for an alkoxide-derived gel that shrinkage is reduced by surfactants, though it is not necessarily eliminated.[9] Techniques other than supercritical drying can also be used to obtain high surface area and pore volume materials. One of them is the addition of "drying control chemical additives" (DCCA) such as glycerol, formamide, dimethyl formamide, oxalic acid, and tetramethylammonium hydroxide.[10,11,12] It was reported that uncracked dry monoliths can be obtained, with a relative pore volume up 97.4%, equivalent to the best aerogels obtained by supercritical drying.[13] The explanation provided for this drying behavior is that a uniform pore size distribution is formed. In turn, this minimizes the differential drying shrinkage.

1.3.3 Cryogel

Another way of avoiding the presence of liquid-vapor interface is to freeze the pore liquid and sublime the resulting solid under vacuum. In this method, the gel liquid is first frozen and thereafter dried by sublimation. Therefore, the formation of a liquid-vapor meniscus is prevented. The materials obtained are then also termed cryogels. Their surface area and mesopore volume tend to be smaller than those of aerogels, although they remain significant.[1,4] However, freeze-drying does not permit the preparation of monolithic gels. The reason is that the growing crystals reject the gel network, pushing it out of the way until it is stretched to the breaking point. It is this phenomenon that allows gels to be used

as hosts for crystal growth: the gel is so effectively excluded that crystals nucleated in the pore liquid are not contaminated with the gel phase; the crystals can grow up to a size of a few millimeters before the strain is so great that macroscopic fractures appear in the gel.[4] Nevertheless, the gel network may eventually be destroyed by the nucleation and growth of solvent crystals, which tend to produce very large pores. To attenuate this event, a rapid freeze process known as flash freezing has been developed. It is also important that the solvent has a low expansion coefficient and a high pressure of sublimation.[1]

1.4 Applications of sol-gel method

Applications for sol-gel process derive from the various special shapes obtained directly from the gel state (monoliths, films, fibers, and monosized powders) combined with compositional and microstructural control and low processing temperatures. Compared with other methods, such as the solid-state method, the advantages of using sol-gel process include[2,7]:

(1) The use of synthetic chemicals rather than minerals enables high purity materials to be synthesized.

(2) It involves the use of liquid solutions as mixtures of raw materials. Since the mixing is with low viscosity liquids, homogenization can be achieved at a molecular level in a short time.

(3) Since the precursors are well mixed in the solutions, they are likely to be equally well-mixed at the molecular level when the gel is formed; thus on heating the gel, chemical reaction will be easy and at a low temperature.

(4) Changing physical characteristics such as pore size distribution and pore volume can be achieved.

(5) Incorporating multiple components in a single step can be achieved.

(6) Producing different physical forms of samples is manageable.

It is clear that the sol-gel process has a lot to offer in the area of applications. Since the sol-gel prepared catalytic materials always involve several components (active metal ions on the oxide support) or the introduction of dopants (metal or non-metal) into the oxide, we will focus on these two applications.

1.4.1 Multi-component system

Many conventional catalyst preparations involve several steps because most active catalysts contain more than one component. For example, in a two-component system, the preparation of supported oxides consists of first forming the support, followed by the introduction of second component. However, sol-gel preparation allows the introduction of two components in a single step. The minor component can either participate directly in the sol-gel chemistry, in which case there is control over the structural and compositional homogeneity of the product, forming a mixed oxide (both existed in the bulk) or not participate, in which case it is simply encapsulated in the gel network of the major component, forming a supported oxide (one is supported on the surface of the other).

These materials are of catalytic interest because they often display acid strengths that are significantly higher than either of the component oxides. [14] In a mixed oxide, the acidic properties are related to the homogeneous mixing of the two component oxides.

However, conventional mixed oxide preparation techniques do not always produce molecularly homogeneous materials. For example, heating a mechanical mixture of two oxides to high temperature often results in a sample that has low surface area and pore volume. Coprecipitation does not favor molecular homogeneity because hydroxides of different metallic cations generally do not precipitate at the same pH.[15] However, because both hydrolysis and condensation are nucleophilic substitution reactions, the sol-gel preparation of mixed oxides offers good control of mixing because of its ability to alter relative precursor reactivity. The following four strategies have been used to match precursor reactivity.[7,16,17]

(1) Using a precursor containing a different alkoxy group.

(2) Prehydrolysis of a less reactive precursor with water.

(3) Slowing down a more reactive precursor by replacing some of its alkoxy groups with different ligands in an approach known as chemical modification. Acetic acid and acetylacetone are two common chemical modifiers.

(4) Performing the preparation at a different temperature.

Silicon alkoxide has been widely used in the preparation of multi-component materials. Because silicon alkoxide has much lower reactivity than titanium alkoxide, Schraml-Marth et al.[18] prepared titania-silica mixed gel with the pre-hydrolysis of the silicon alkoxide. In comparison, they prepared other samples by completely hydrolyzing each of the two alkoxides before mixing. Based on the characterization of the microstructure of these samples, they found that the latter samples contain domains of titania crystallites embedded in an amorphous silica matrix, while the former samples contain no such

domains and are better mixed at the molecular level. The difference was due to a better match in precursor reactivity from the prehydrolysis. Differences in the distribution of two components in a mixed oxide lead to differences in catalytic properties. Miller et al.[19] recently found that titania-silica aerogels prepared with prehydrolysis of the silicon alkoxide are about a factor of 3 more active in isomerizing 1-butene than those prepared without prehydrolysis. The higher activity was attributed to more acid sites contained in the more homogeneous sample derived from prehydrolysis. During the study of selective catalytic reduction of NO with NH_3 on V/TiO_2-SiO_2, Handy et al.[20] found that the sample prepared without prehydrolysis was active and the sample with prehydrolysis was not. The authors suggested that because of well mixing with prehydrolysis, the support was more like silica itself, so the interaction between support and vanadia would be weaker with a subsequent less stable vanadia in an active form. Without prehydrolysis, the separated titania crystallite present in the support interacted strongly with vanadia, thereby stabilizing active vanadia.

1.4.2 Doping

Homogenization achieved at a molecular level in sol-gel process can also be used to introduce dopants into oxides. Chen et al.[21] prepare N co-doped TiO2 by mixing titanium tetra-n-butyl oxide, urea, and tetrabutylammonium hydroxide in the sol-gel step. From X-ray photoelectron spectroscopy (XPS) measurements and lattice parameter analysis, the authors found that nitrogen atoms were incorporated into the lattice of TiO_2 through substituting the sites of oxygen atoms. Cong et al.[22] also synthesized N-doped TiO2 by a sol-gel process. Analysis by Raman and XPS indicated that nitrogen was doped effectively and most nitrogen dopants might be present in the chemical environment of

Ti-O-N and O-Ti-N. Both catalysts showed higher activity for the degradation of organic pollutants under visible light irradiation compared with the undoped TiO_2 or commercial P25 TiO_2. Yu et al.[23] introduced vanadium ion into the lattice of TiO_2 by a sol-gel method. The results suggested that vanadium dopant replaced some Ti ions and formed Ti-V-O structure. The substitution enhanced the adsorption of hydroxide ions onto the surface of the catalyst. More hydroxyl radicals then can be generated and this resulted in a higher activity. Ward et al[24] prepared zirconia-sulfate aerogels by mixing sulfuric acid directly with the zirconium alkoxide in one step. From X-ray diffraction and infrared measurements, these authors found that sulfate ions are initially trapped in the bulk of the aerogel and then expelled onto the surface and transformed into an active surface species that promotes strong Bransted acidity. These sulfate groups created Bransted acidity which is necessary for n-butane isomerization. These results establish the relationship between crystallinity, sulfate structure and content, and the acidity and activity of this important class of solid superacids. Lopez et al.[25] reported the homogeneous hydrolysis of magnesium alkoxide in a solution containing ethanol, water, and LiCl to prepare Li/MgO catalyst. Compared with conventional impregnation method, the authors found that sol-gel derived catalyst was more highly hydroxylated and showed higher selectivity toward olefin formation. It was obvious that the way of introduction of Li affected the nature of active sites of the catalysts.

1.5 Conclusions

In the past several decades, sol-gel process has been increasingly applied to synthesize materials. The parameters in the various steps of a sol-gel process provide opportunities for exceptional control of the sol-gel product's structural and chemical properties, and

this control allows people to study the effects of composition, homogeneity, and pore structure on the performance of materials.

References

[1] A. C. Pierre, G. M. Pajonk, Chem. Rev., 102 (2002) 4243

[2] H. Schmidt, Journal of non-crystalline solids, 100 (1988) 51

[3] J. Livage, C. Sanchez, Journal of non-crystalline solids, 145 (1992) 11

[4] C. J. Brinker, G. W. Scherer, Sol-gel science, the physics and chemistry of sol-gel processing, 1990, Academic.

[5] C. Sanchez, F. Ribot, New Journal of Chemistry, 18 (1994) 1007

[6] G. M. Pajonk, Heterogeneous Chemistry Reviews, 2 (1995) 129

[7] D. A. Ward, E. I. Ko, Ind. Eng. Chem. Res., 34 (1995) 421

[8] G. W. Scherer, Journal of non-crystalline Solids, 100 (1988) 77

[9] J. Zarzycki, M. Prassas, J. Phalippou, J. Mater. Sci., 17 (1982) 3371

[10] H. Chen, E. Ruckenstein, Journal of Colloid Interface Science, 145 (1991) 581

[11] J. B. Chan, J. Jonas, Journal of Non-crystalline Solids, 126 (1990) 79

[12] C. Roger, M. J. Hampden-Smith, Journal of Material Chemistry, 2 (1992) 1111

[13] L. L. Hench, Science of Ceramic Chemical Processing, Wiley, New York, 1986

[14] H. H. Kung, J. Solid State Chem. 52 (1984) 191

[15] P. Courty, C. Marcilly, Preparation of catalysts; B. Delmon, P. A. Jacobs, G. Poncelet, Eds.; Elsevier Science; Amsterdam, 1976; p119

[16] B. E. Yoldas, Appl. Opt. 21 (1982) 2960

[17] K. L. Walther, A. Wokaun, B. E. Handy, A. Baiker, J. Non-Cryst. Solids 134 (1991) 47

[18] M. Schraml-Marth, K. L. Walther, A. Wokaun, B. E. Handy, A. Baiker, J. Non-Csyst. Solids 143 (1992) 93

[19] J. B. Miller, S. T. Johnston, E. I. Ko, J. Catal. 150 (1994) 311

[20] B. E. Handy, A. Baiker, M. Schramal-Marth, A. Wokaun, J. Catal. 133 (1992) 1

[21] D. Chen, Z. Jiang, J. Geng, Q. Wang, D. Yang, Ind. Eng. Chem. Res. 46 (2007) 2741

[22] Y. Cong, J. Zhang, F. Chen, M. Anpo, J. Phys. Chem. C 111 (2007) 6976

[23] J. Yu, J. Lin, R. Kwok, Journal of Photochemistry and Photobiology A: Chemistry 111 (1997) 199

[24] D. A. Ward, E. I. Ko, J. Catal. 150 (1994) 18

[25] T. Lopez, R. Gomez, A. Ramirex-Solis, E. Poulain, O. Novaro, J. Mo. Catal. 88 (1994) 71

CHAPTER 2 Overview on desulfurization

2.1 Introduction

Due to environmental mandates, refineries are facing the challenge of producing increasingly cleaner fuels. The primary focus of the new regulations is the reduction of sulfur in gasoline or diesel fuel because sulfur oxide emissions generated by vehicle engines contribute to acid rain, poison catalysts in catalytic converters, and are an integral component in the cycle of atmospheric gas chemistry that leads to ozone production and smog.[1,2,3,4] As a result, the sulfur content in fuels has been gradually tightened. The problem of deep removal of sulfur has become more serious due to the lower and lower limit of sulfur content in the final product by regulatory specifications, and the higher and higher sulfur contents in the crude oil. Interest in ultra-low sulfur fuels is also driven by fuel cells because of their high energy density, ready availability, safety and ease for storage. However, catalysts used in the fuel processor are very sulfur sensitive. For example, fuels for proton exchange membrane fuel cell applications required the use of a fuel with sulfur content less than 1 ppm in order not to poison and deactivate the reformer catalyst.[5]

The state of the art in desulfurization technology is hydrodesulfurization (HDS), which has been used worldwide. In this process, under high temperature (300-340°C) and high pressure (20-100 atm of H_2), sulfur-containing compounds are converted to H_2S and corresponding hydrocarbon on $CoMo/Al_2O_3$ or $NiMo/Al_2O_3$ catalysts.[6] The reactivity of organosulfur compounds varies widely depending on their structure and local sulfur atom

environment.[7] Figure 2.1 presents a qualitative relationship between the type and size of sulfur molecules in various distillate fuel fractions and their relative reactivity.[2] HDS process is highly efficient in removing thiols, sulfides, and disulfides because of higher electron density on the sulfur atom and weaker C-S bond, but less effective for thiophenes and thiophene derivatives. The least reactive is the dibenzothiophene with methyl groups at the 4- and 6-positions. Therefore, in deep HDS, the conversion of these more and more refractory key substituted dibenzothiophenes largely determines the required operating conditions for the production of ultralow-sulfur fuels. This can only be achieved under severe reaction conditions with respect to pressure, temperature, and residence time, which significantly increases the cost of HDS. To reduce the sulfur content of diesel from 500 to 15 ppm, an estimate showed that the HDS reactor size needed to be increased by a factor of 7.[4] Another estimate showed that in order to reduce the sulfur level in diesel from 300 to less than 10 ppm, the HDS reactor volume needed to be increased by a factor of about 15 at 600 psi, or by a factor of 5 at 1000 psi.[8] Also, more severe conditions result in undesired side reactions, increased coke formation and subsequent catalyst deactivation. Consequently, development of new and affordable deep desulfurization processes for removing the refractory sulfur compounds is one of the major challenges for refineries and fuel-cell research.

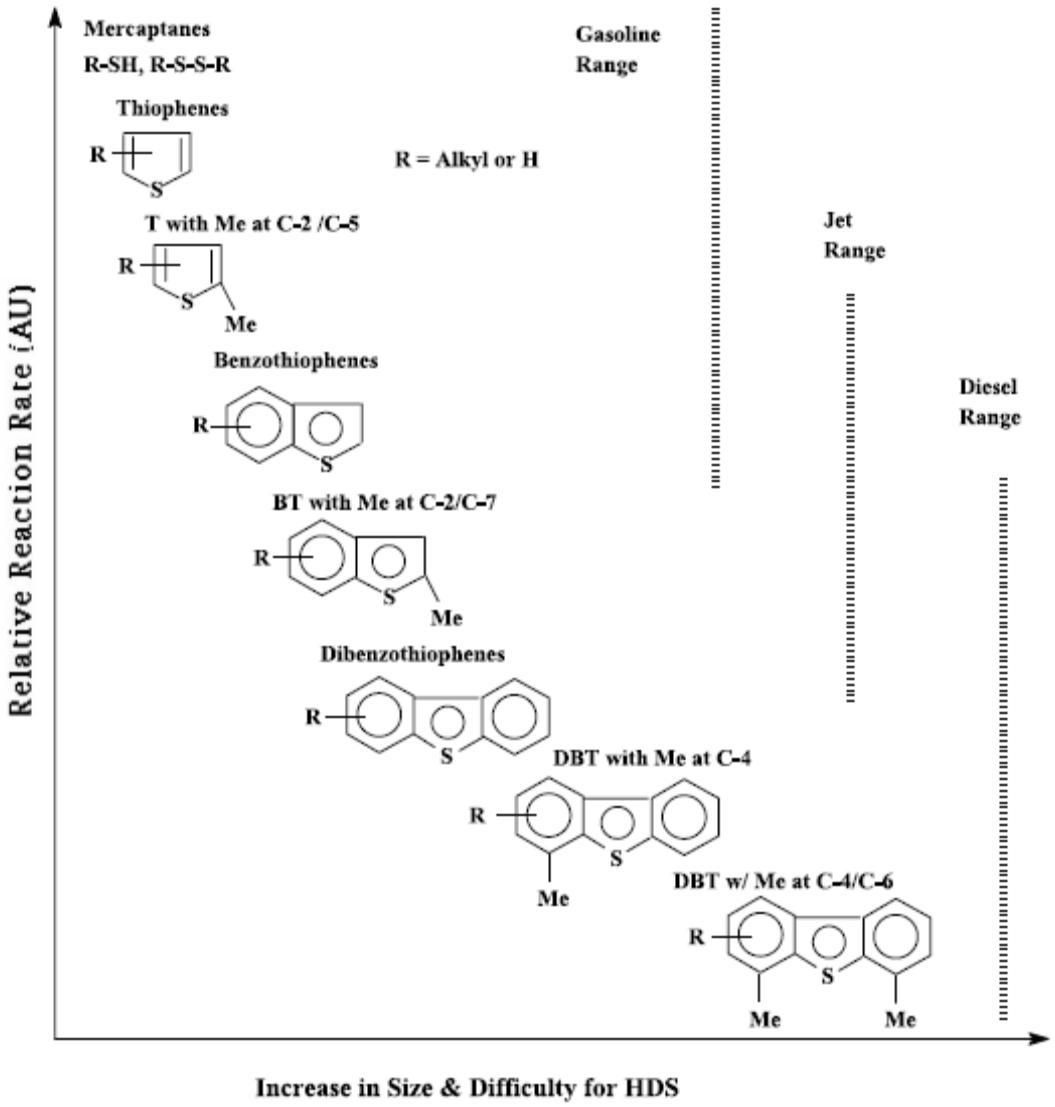

Figure 2.1 Reactivity of various organic sulfur compounds in HDS versus their ring size and positions of alkyl substitutions on the ring[2]

2.2 “Non-HDS” based desulfurization technologies

Faced with severely high costs of environmental compliance, a number of new technologies that do not use hydrogen for catalytic decomposition of organosulfur compounds have been contemplated.

2.2.1 Desulfurization via extraction[3]

Extractive desulfurization is based on the fact that organosulfur compounds are more soluble than hydrocarbons in an appropriate solvent. The general process flow is shown in Figure 2.2. In a mixing tank, the sulfur compounds are transferred from the fuel oil into the solvent due to their higher solubility in the solvent. Subsequently, the solvent–fuel mixture is fed into a separator in which hydrocarbons are separated from the solvent. The desulfurized hydrocarbon stream is used either as a component to be blended into the final product or as a feed for further transformations. The organosulfur compounds are separated by distillation and the solvent is recycled. The most attractive feature of extractive desulfurization is its applicability at low temperature and low pressure. The mixing tank can even operate at ambient conditions. The process does not change the chemical structure of the fuel oil components. To make the process efficient, the solvent must be carefully selected to satisfy a number of requirements. The organosulfur compounds must be highly soluble in the solvent. The solvent must have a boiling temperature different than that of the sulfur containing compounds, and it must be inexpensive to ensure economic feasibility of the process. Solvents of different nature have been tried, among which acetone, ethanol, polyethylene glycols, and nitrogen containing solvents showed a reasonable level of desulfurization of 50–90% sulfur removal, depending on the number of extraction cycles.

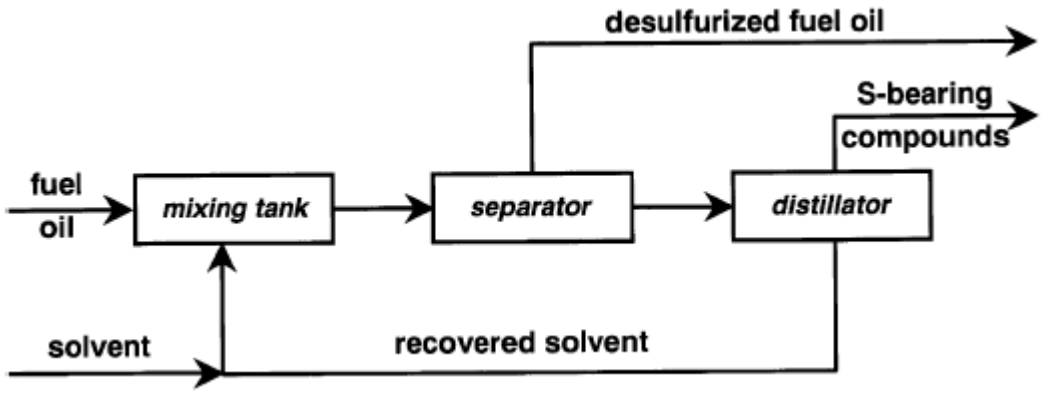

Figure 2.2 General process flow of extractive desulfurization[3]

2.2.2 Desulfurization via precipitation[3]

Desulfurization by precipitation is based on the formation of insoluble charge-transfer complexes and subsequent removal through filtration. Experiments were reported for 4,6-dimethyldibenzothiophene in hexane and gas oil, using 2,4,5,7-tetranitro-9-fluorene (acting as p-acceptor). A suspension of the p-acceptor and sulfur containing gas oil was stirred in a batch reactor where insoluble charge-transfer complexes between p-acceptor and 4,6-dimethyldibenzothiophene formed. The consecutive steps include filtration to remove the formed complex from gas oil and the recovery of the p-acceptor excess using a solid adsorbent. The disadvantage is low selectivity for sulfur compound removal because of the competition in complex formation between sulfur compounds and other non-sulfur aromatics or nitrogen compounds. Moreover, a large excess over stoichiometric amount of p-acceptor is used to provide good complexing and this excess should be removed from the oil stream afterwards.

2.2.3 Desulfurization via oxidation

Desulfurization by selective oxidation usually consists of two main steps: oxidation of sulfur compounds and subsequent purification. One of the main advantages of the oxidative desulfurization process is that some sulfur compounds, which are among the most resistant to HDS due to their steric hindrance, show a high reactivity towards oxidation. Selective oxidation followed by distillation is an option since the oxidation of sulfur compounds to sulfoxides or sulfones increases their boiling temperature. Oxidation followed by thermal decomposition of oxidized sulfur compounds was reported: sulfur is released mainly as SO_2 at low temperatures, and some H_2S is fomed if the temperature of decomposition is above 300 °C.[3] The photooxidation method showed high selectivity to remove sulfur compounds.[9,10,11] Sulfur containing hydrocarbons are suspended in an aqueous-soluble solvent and irradiated by UV or visible light, resulting in the oxidation of the sulfur compounds. The polar compounds formed are rejected by the non-polar hydrocarbon phase and are concentrated in the solvent. Therefore, the solvent and the hydrocarbon phases are separated. Acetonitrile was a good solvent candidate since it can provide relatively high solubility of initial and oxidized sulfur compounds. Also, the photochemical reaction rate could be enhanced by a photosensitizer. The combination of solvent and photosensitizer has to be optimized to increase the rate of the organosulfur compounds photo-transformation, making the process technically and economically feasible. Ultrasound has been reported effective in the oxidation of sulfur in the thiophenic compounds, forming sulfoxides and sulfones. Subsequently, the sulfoxides and sulfones are removed by solvent extraction.[12,13]

2.2.4 Desulfurization via bioprocess[14]

Biological transformation of sulfur-containing compounds in fuels is based on a biocatalyst that has the specific pathway that enables it to clip sulfur from sulfur heterocyclic compounds. Rhodococcus species are considered the most promising microbial biocatalyst to selectively remove sulfur from substituted and unsubstituted dibenzothiophene in the fuels, including sulfur compounds that hindered chemical catalysis and resisted removal by mild hydrotreatment. The biological pathway involves four enzymatic steps as shown in Figure 2.3. This bioprocess results in the production of water-soluble end products, namely sulfate, that can be extracted from the fuel. Organic sulfur free compounds remain in the fuel.

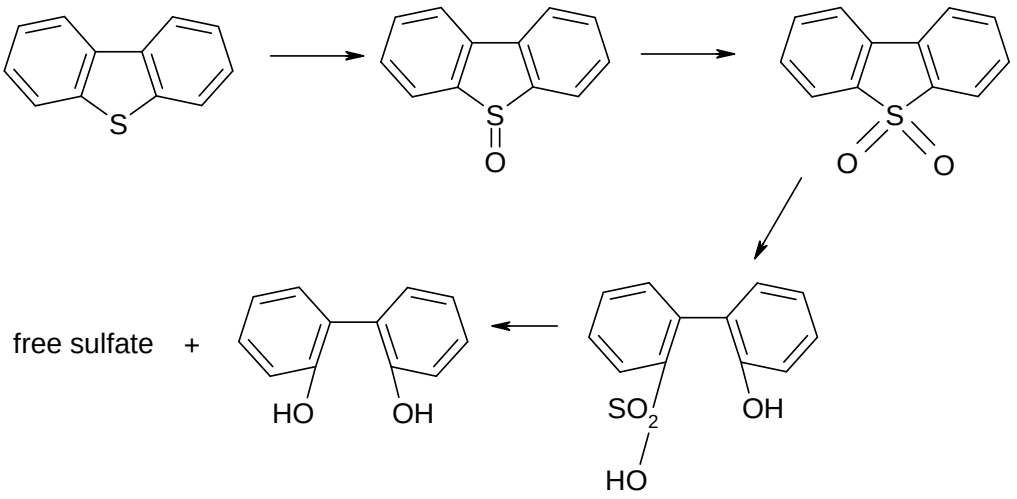

Figure 2.3 The 4S pathway for the selective removal of sulfur from dibenzothiophene[14]

2.2.5 Desulfurization via adsorption

One of the new approaches for desulfurization is adsorption, which selectively removes sulfur compounds at ambient pressure and temperature from fuels. This method might be

the most economical way for the removal of sulfur compounds from fuels. The fuel is contacted with a solid sorbent which selectively adsorbs organosulfur compounds from refinery streams. Efficiency of the desulfurization is mainly determined by the sorbent properties: its adsorption capacity, selectivity for the organosulfur compounds, durability and regenerability.

An adsorption-based desulfurization technology called IRVAD is targeted to remove a wide spectrum of organosulfur compounds from various refinery streams.[15] A simplified process scheme is shown in Figure 2.4. The process uses an alumina-based sorbent to counter-currently contact a sulfur-rich hydrocarbon stream. The desulfurized hydrocarbon stream is produced at the top of the adsorber whereas the spent sorbent is withdrawn at the bottom. The spent sorbent is circulated into the reactivator where organosulfur compounds and some adsorbed hydrocarbons are desorbed from the sorbent surface. The process operates up to 240 ºC with a hydrocarbon/sorbent weight ration of about 1.4.

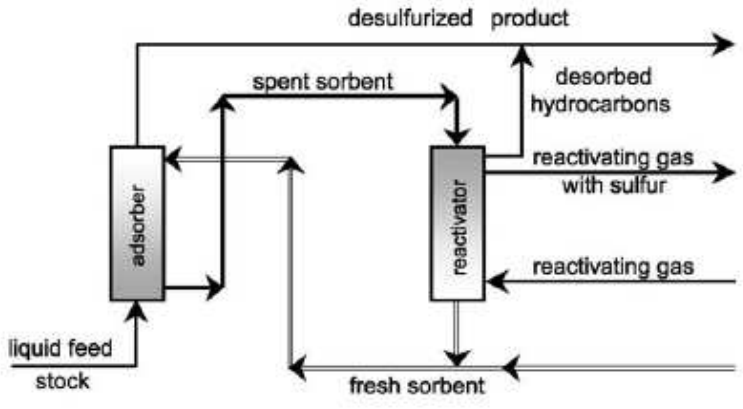

Figure 2.4 Simplified adsorptive desulfurization process flow[3]

There is an ongoing effort to develop new adsorbents to remove the thiophenic compounds from commercial fuels either via π-complexation[16], van der Waals and electrostatic interactions[17,18], or reactive adsorption by chemisorption at elevated temperatures.[19,20,21] A series of adsorbents based on the principle of π-complexation were reported by Yang and coworkers.[22,23,24,25] The π-complexation bonds are stronger than van der Waals interactions, but they are also weak enough to be broken by moderate changes in temperature or pressure, providing the opportunity for selective adsorption of sulfur compounds from fuels. The authors found that Cu(I)-zeolite Y, Ag-zeolite Y, and $CuCl/Al_2O_3$ were highly selective toward thiophene and their derivatives, and fuels with sulfur content less than 0.2 ppmw could be obtained. Song et al.[2,26] explored selective adsorption to remove sulfur (PSU-SARS) from fuels over metal, metal sulfides, metal oxides, and zeolite-based adsorbents under ambient temperature and pressure. The scientific basis behind the approach for PSU-SARS is that there exists site-specific interactions between the sulfur atom of the thiophenic compound and metal species these are seen in existing organometallic complexes. These adsorbents had been used to selectively remove sulfur from gasoline, diesel fuel, and jet fuel for producing ultraclean transportation fuels and for fuel-cell applications. The temperatures for various application environments range from room temperature to about 250 ºC. Adsorption of thiophene and benzothiophene in an organic model solution of hydrodesulfurized gasoline was studied by Xue et al. using metal-ion-exchanged Y-zeolite adsorbents at 80 °C. Ce Y-zeolite showed high adsorptive capacities for both sulfur compounds.[27] The general desulfurization pathway of sulfur removal by reactive adsorption desulfurization can be described by the following scheme: [1,2,3]

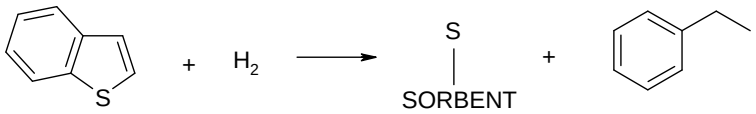

The sulfur atom is removed from the molecule and is bound by the sorbent under operating conditions at 340-410 ºC and 2-20 bar. The sorbent is regenerated with air (forming SO_2), followed by reduction with H_2. The corresponding hydrocarbon part is returned to the final product stream without any structural changes.

2.3 Nanocrystalline adsorbents

Nanocrystalline metal oxides are of current interest and they constitute a novel family of inorganic porous materials.[28,29] They generally posses high surface areas and readily form aggregates either in powder or consolidated pellet forms. The metal oxide nanocrystals can be prepared in unique shapes and they exhibit remarkably different chemical properties. For example, nanocrystalline MgO adsorbs about 6 molecules of SO_2 per nm^2 area while commercial MgO adsorbs only 2 molecules of SO_2 per nm^2.[30] The unique properties of nanocrystalline metal oxides might be exploited for the adsorption of sulfur compounds from fuels, too. The possible advantages of adsorbents based on nanocrystalline oxides compared with other conventional adsorbents are: open pore structure with a high pore volume so the adsorbate molecules can enter and exit easily, high surface area, unlimited loading level of metal ions, and various mixed nanocrystalline metal oxides could be prepared with varying acidic/basic nature that will suit a particular application.[31] In the following two chapters, experimental work with nanocrystalline Cu/Al_2O_3 and Zn/Al_2O_3 will be described.

References

[1] A. J. Hernandez-Maldonado, R. T. Yang, Catalysis Reviews, 46 (2004) 111

[2] C. Song, Catalysis Today**,** 86 (2003) 211

[3] I V. Babich, J. A. Moulijn, Fuel, 82 (2003) 607

[4] D. D. Whitehurst, T. Isoda, I. Mochida, Advances in Catalysis**,** 42 (1998) 345

[5] J. H. Kim, X. Ma, A. Zhou, C. Song, Catalysis Today, 111 (2006) 74

[6] B. C. Gates, J. R. Katzer, G. C. Schuit, Chemistry of Catalysis Processes, McGraw-Hill, New York, 1979

[7] I. Mochida, K. H. Choi, Journal of the Japan Petroleum Institute, 47 (2004) 145

[8] G. Parkinson, Chem. Eng., 108 (2001) 37

[9] Y. Shiraishi, Y. Taki, T. Hirai, I. Komasawa, Ind. Eng. Chem. Res., 37 (1998) 203

[10] Y. Shiraishi, Y. Taki, T. Hirai, I. Komasawa, Ind. Eng. Chem. Res., 38 (1999) 3310

[11] Y. Shiraishi, Y. Taki, T. Hirai, I. Komasawa, Ind. Eng. Chem. Res., 38 (1999) 4538

[12] H. Mei, B. Mei, T. Yen, Fuel, 82 (2003) 405

[13] T. Yen, H. Mei, S. Lu, US Patent (2002) 6,402,939

[14] B. L. McFarland, D. J. Boron, W. Deever, J. A. Meyder, A. R. Johnson, R. M. Atlas, Critical Reviews in Microbiology, 24 (1998) 99

[15] R. L. Irvine, US Patent 5,730,860 (1998)

[16] R. T. Yang, Adsorbents: Fundamentals and Applications, Wiley, New York, 2003, Chap. 10

[17] A. S. Salem, Ind. Eng. Chem. Res., 33 (1994) 336

[18] A. S. Salem, H. S. Hamid, Chem. Eng. Technol., 20 (1997) 342

[19] G. P. Khare, U. S. Patent 6,274,533 (2001)

[20] G. P. Khare, U. S. Patent 6,184,176 (2001)

[21] S. Velu, X. Ma, C. Song, Ind. Eng. Chem. Res., 42 (2003) 5293

[22] R. T. Yang, A. J. Hermandez-Maldonado, F. H. Yang, Science, 301 (2003) 79

[23] A. J. Hermandez-Maldonado, S. D. Stamatis, R. T. Yang, A. Z. He, W. Cannella, Ind. Eng. Chem. Res., 43 (2004) 769

[24] R. T. Yang, A. Takahashi, F. H. Yang, Ind. Eng. Chem. Res., 40 (2001) 6236

[25] A. J. Hermandez-Maldonado, R. T. Yang, Ind. Eng. Chem. Res., 42 (2003) 3103

[26] X. Ma, L. Sun, C. Song, Catalysis Today, 77 (2002) 107

[27] M. Xue, R. Chritrakar, K. Skane, J. Colloid Interface Sci., 285 (2005) 487

[28] K. J. Klabunde, J. Stark, O. Koper, C. Mohs, D. G. Park, S. Decker, Y. Jiang, I. Lagadic, D. Zhang, J. Phys. Chem., 100 (1996) 12142

[29] E. Lucas, S. Decker, A. Khaleel, A. Seitz, S. Fultz, A. Ponce, W. Li, C. Carnes, K. J. Klabunde, Chem. Eur. J., 7 (2001) 2505

[30] J. V. Stark, D. G. Park, I. Lagadic, K. J. Klabunde, Chem. Mater., 8 (1996) 1904

[31] P. Jeevanandam, K.J. Klabunde, S.H. Tetzler, Microporous and Mesoporous Materials, 79 (2005)

CHAPTER 3 Cu-based nanoscrystalline Al_2O_3 adsorbent

3.1 Introduction

This chapter will focus on preparing and characterizing alumina-supported copper adsorbent, followed by experimental testing of desulfurization activities. In particular, this work includes descriptions:

1. To prepare Cu/Al_2O_3 adsorbents with different copper loading by sol-gel.
2. To characterize the adsorbents.
3. To run the desulfurization experiments.

3.2 Preparation of Cu/Al_2O_3 adsorbent

The Cu/Al_2O_3 adsorbents were prepared by the sol-gel/aerogel process using cupric nitrate and aluminum isopropoxide (98.0%, Aldrich). As shown in Figure 3.1, the general procedure for the preparation consisted of the following steps. An appropriate amount (0.076, 0.198, and 0.424 g corresponding to 2, 5, and 10 wt% of Cu respectively) $Cu(NO_3)_2$ $5/2H_2O$ was dissolved in 19 ml ethanol. Aluminum isopropoxide (4.08 g) was put in a flask containing 133 ml toluene and 60 ml ethanol and stirred for one hour. After complete dissolution, the Cu solution was added into the mixture. The hydrolysis was accomplished by adding about 2 ml deionized water, followed by vigorous stirring at room temperature for 12 h. Afterwards, an autoclave procedure was used to dry the gel under hypercritical conditions. After being flushed with a flow of N_2 gas, the Parr (autoclave) mini reactor was then pressurized with N_2 gas to obtain the initial pressure of 100 psi. The reactor was slowly heated from room temperature to 265 °C at a rate of

1°C/min by a PID controller. The overall heating time was about 4 h. The temperature was allowed to equilibrate at 265 °C for 15 min before the reactor was vented to release the pressure. The reactor was immediately removed from the heater and then flushed with N_2 for 10 –15 min to remove any remaining organic solvent. During the heating, the pressure inside the reactor increased from 100 psi to 1000 psi. After it was allowed to cool to room temperature, the product was ground using an agate mortar. The powder was calcined at 500°C for 4 h in air. The final activation step was conducted at 700°C under vacuum for 3 h to promote auto-reduction of Cu^{2+} to Cu^{+}.

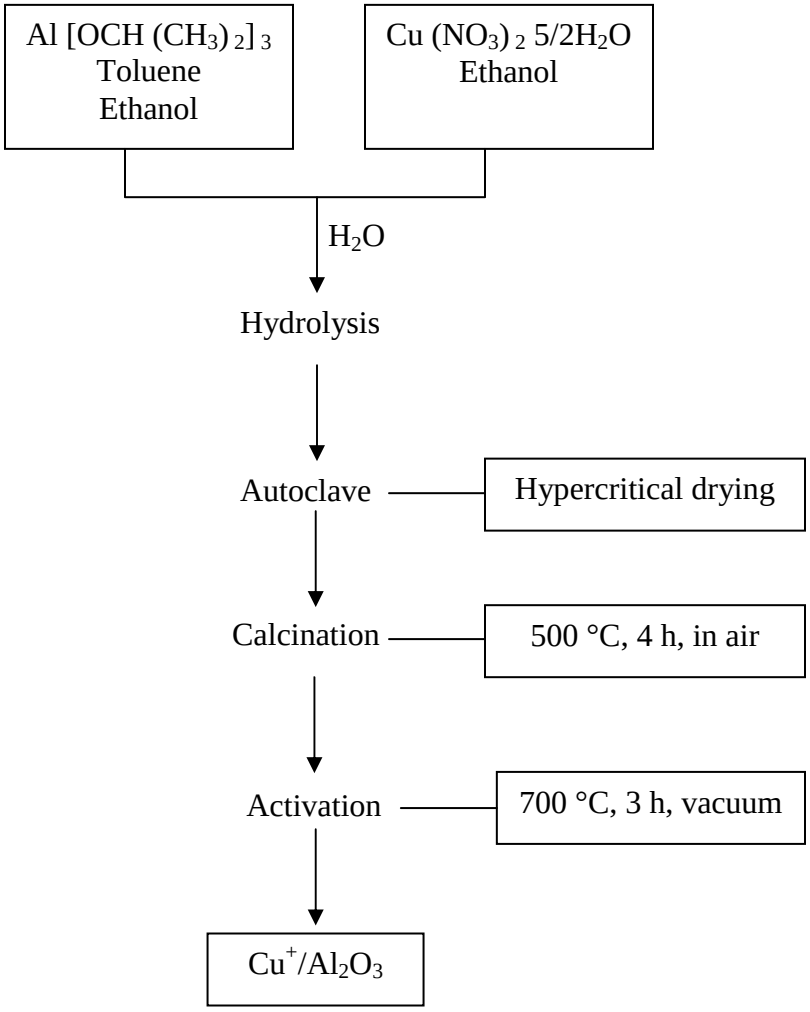

Figure 3.1 General procedure for preparation of adsorbents

3.3 Characterization of Adsorbent

The specific surface area, pore volume, and average pore size of the samples were estimated using the N_2 adsorption-desorption isotherm at -196°C by the multi-point Brunauer-Emmet-Teller (BET) method using a NOVA 1000 adsorption instrument (Quantachrome, USA). Before adsorption, all the samples were degassed for 1 h at 150°C under vacuum. The surface area and pore volume were calculated using the adsorption isotherms. The desorption isotherms were used to calculate pore size distributions.

X-Ray powder diffraction patterns were obtained with a Bruker D8 diffractometer, using Cu Kα radiation (1.5406Å) at 40 kV and 40 mA and a secondary graphite monochromator. The measurements were recorded in steps of 0.025° with a count time of 1 s in the 2θ range of 20-80°. Identification of the phases was made with the help of the Joint Committee on Powder Diffraction Standards (JCPDS) files.

UV-Visible spectra measurements were carried out on a Cary 500 spectrophotometer equipped with a Cary 4/5 diffuse reflection sphere, in the 200-800 nm wavelength range. The baseline was recorded using a polytetrafluoroethylene reference. All spectra were taken under atmospheric conditions.

FT-IR spectra were recorded on Nicolet NEXUS 870 infrared spectrometer using in situ DRIFTS cell attached to a gas supply system. The sample was placed into the ceramic cup of a commercial DRIFTS cell (Spectra-Tech) with a ZnSe window. Gases used for studies were He (99.99%), CO (99.99%), and O_2 (99.996%). The FT-IR spectrometer

with a liquid nitrogen cooled MCT detector allows the surface characterization to be performed. At room temperature, ppm CO in helium was pulsed in the cell. Spectra were collected after each step of the adsorption procedure. The spectrum of the sample before CO adsorption was subtracted from all the spectra obtained after adsorption for better evaluating the surface species.

3.4 Adsorption experiments

Adsorption experiments were performed by a batch method. After the activation, the adsorbent was cooled down to room temperature and quickly mixed with 40 ml model fuel consisting of pentane and thiophene (the S concentration of the model fuel is 20 ppmw). The mixture was kept in a sealed tube at room temperature with stirring for a desired time. The liquid phase was separated from the adsorbent, and the sulfur concentration in the solution was measured by UV-Vis spectrophotometry (thiophene has an absorption band at about 230 nm and the absorbance corresponds to the residual thiophene content).

3.5 Results and discussion

Figure 3.2 shows thiophene adsorption results on Cu/Al_2O_3 adsorbents with different loadings. In this figure, the smallest absorbance means the largest amount of thiophene was adsorbed. The adsorbent with 5 wt% Cu showed the highest capacity, 1.8 mg/g. The sulfur content of the solution after adsorption was 2.0 ppmw. The capacities were 1.5 and 0.9 mg/g for 2 wt% and 10 wt% Cu adsorbents respectively. The corresponding sulfur contents were 5 and 11 ppmw for the remaining solutions. It was clear that sol-gel prepared Cu/Al_2O_3 held considerable promise for thiophene adsorption.

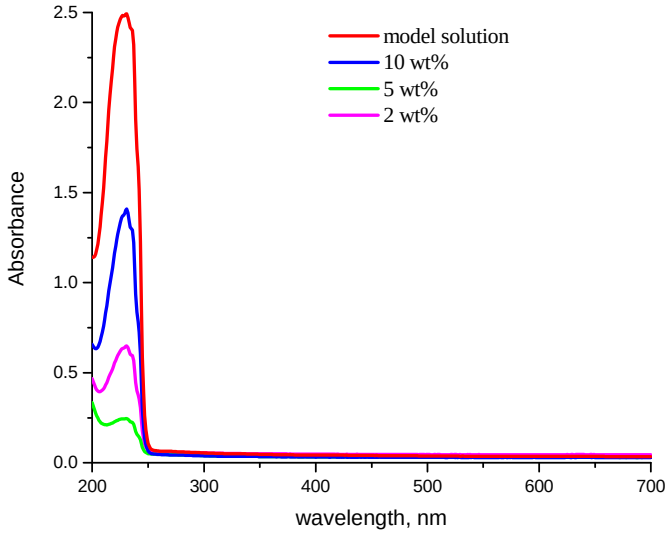

Figure 3.2 Adsorption of thiophene on Cu/Al_2O_3 with different Cu loadings

Figure 3.3 shows the kinetics of thiophene adsorption on the 5 wt% Cu/Al_2O_3 adsorbent. The adsorption was very fast during the first 30 min, and equilibrium was nearly achieved after 1.5 h.

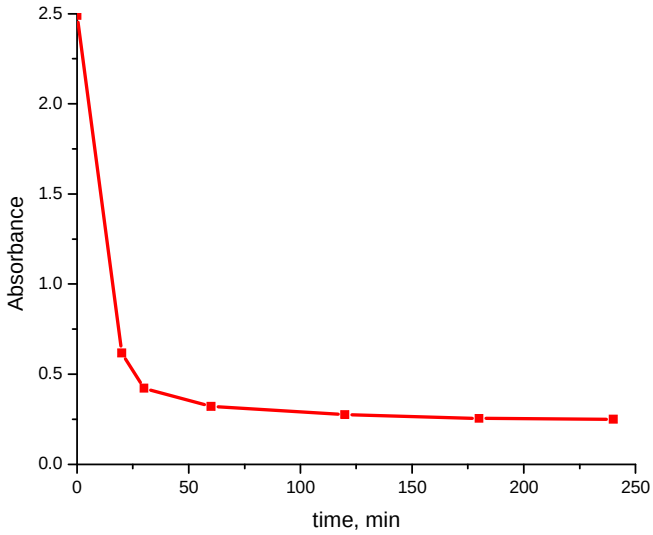

Figure 3.3 Kinetics of thiophene adsorption on 5 wt% Cu/Al_2O_3 adsorbent

3.5.1 Morphology of the Cu/Al_2O_3 adsorbents

The adsorption/desorption isotherms for various adsorbents were typical of type IV, which was characteristic of mesoporous solids.[1] Quantitative comparisons of the pore structure of various samples are reported in Table 3-1. The copper loading had a great influence on the textural properties. The BET surface area, pore volume and pore diameter did not change with lower loading, showing that the structure of the support was preserved. The small decrease of these parameters was attributed to plugging by very fine crystallites of CuO. At higher loading, the insertion of copper decreased the pore diameter greatly, which was presumably the result of blockage of some pores by CuO particles as shown later by XRD results.

Table 3-1 Pore structure of Cu/Al_2O_3 adsorbents

Adsorbents	Surface area (m^2/g)	Pore Volume (cm^3/g)	Pore diameter (nm)
0 wt% Cu/Al_2O_3	452	2.1	17
2 wt% Cu/Al_2O_3	425	1.9	16
5 wt% Cu/Al_2O_3	385	1.9	12
10 wt% Cu/Al_2O_3	357	1.5	5

3.5.2 X-ray Diffraction

Figure 3.4 shows XRD patterns of the Cu/Al_2O_3 samples before calcination, after calcination and after thermovacuum treatment. Metallic copper diffraction lines were observed for the samples before calcination treatment, indicating that much of the Cu^{2+} was reduced during the hypercritical drying step. The intensity of the XRD peaks due to copper increased as the copper content increased. After calcination at 500°C, no peaks

due to copper species were observed for samples with less than 5 wt% copper loading, suggesting that copper was highly dispersed on the support surface, or the crystallite size of the copper species was so small that they were undetectable as a consequence of sensitivity and size limits of the XRD technique. Weak diffraction lines of crystalline CuO (2θ = 35.5° and 38.7°) were confirmed on 5 wt% Cu/Al_2O_3. More intensive diffraction lines were noticed for 10 wt% Cu/Al_2O_3. This showed that the bulk structure of samples with low copper content was rather similar to that of alumina which had a defective spinel phase with low crystallinity.[2] Auto-reduction of Cu^{2+} to Cu^{+} after thermovacuum treatment was confirmed by the Cu_2O diffraction lines observed for 10 wt% Cu/Al_2O_3. The lack of Cu_2O peaks in the lower copper loading samples was also attributed to the small crystal size of Cu_2O or the limit of XRD. Compared with the black color observed in $Cu(II)/Al_2O_3$ (calcined samples), the color of $Cu(I)/Al_2O_3$ (after thermovacuum treatment) was light gray, which was also evidence of auto reduction;[3] Cu(I) species are usually colorless except where color results from charge transfer to the anion.[4] The mechanism of thermal reduction of Cu^{2+} was assumed as follows: the coordinated hydroxyl groups of the isolated Cu^{2+} ions were desorbed as water during calcination. The evolution of two oxygen ligands as an oxygen molecule from the dehydrated Cu^{2+} monomer caused the thermal reduction of Cu^{2+} into the low-coordinated Cu^{+} ion.[5]

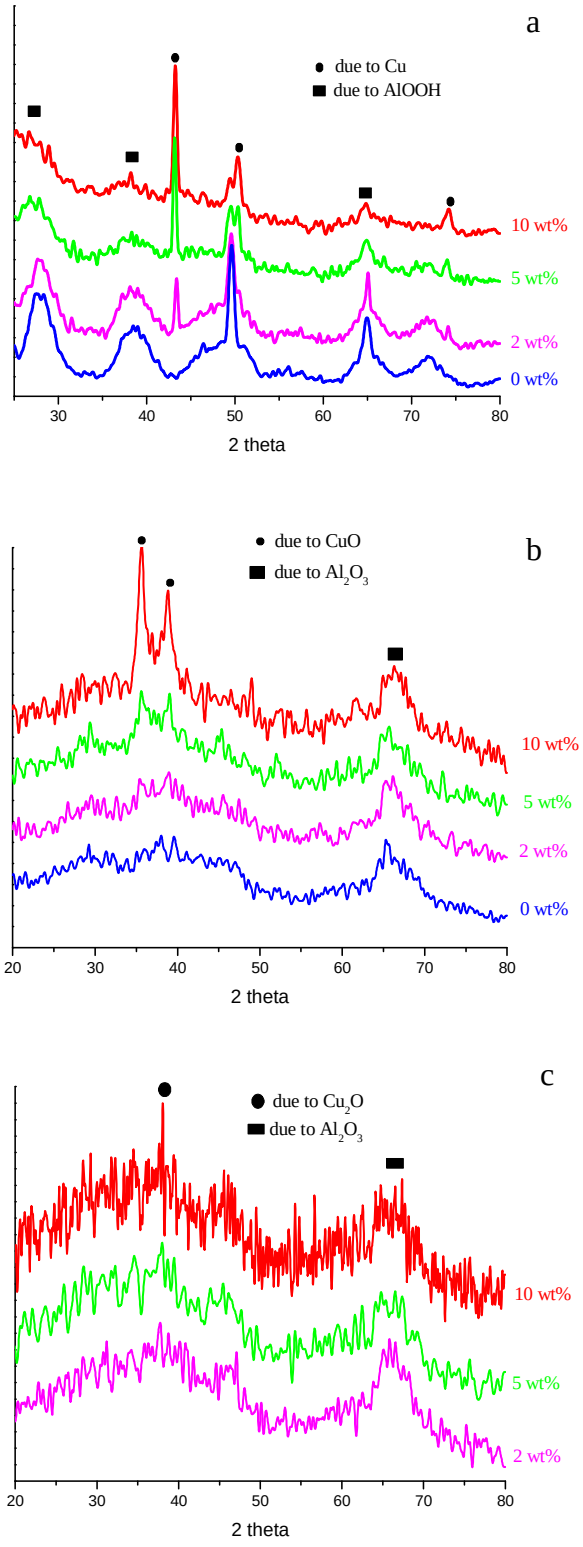

Figure 3.4 XRD patterns of Cu/Al_2O_3 adsorbents with different Cu loadings (a) before calcination, (b) after calcination, and (c) after thermovacuum treatment

3.5.3 UV-Vis spectroscopy

Figure 3.5 shows the diffuse reflectance UV-Vis spectra of Cu-Al_2O_3 samples before calcination, after calcination and after thermovacuum treatment. According to literature, the strong absorption between 200 and 300 nm were due to the LMCT (ligand to metal charge transfer) band of Cu^{2+} species. Absorption between 600 to 800 nm corresponded to the d-d transition band of Cu^{2+} situated in an octahedral O_h configuration more or less tetragonally distorted. Fine Cu metallic particles exhibited absorption in the 580-590 nm range corresponding to the conduction band.[6,7,8]

Before calcination, absorption bands in the spectrum of the sample without copper (support) were observed at 210 and 270 nm. This might be due to trace impurities in the aluminum isopropoxide. A small peak in this region assigned to a LMCT transition from oxygen to contaminant transition metal cations was previously reported by Yamamoto.[6] For samples with copper, we could not rule out the existence of Cu^{2+} species because the LMCT absorption band of Cu^{2+} species overlapped with that of contaminant of the support in the region of 200-300 nm. Also, another band around 600 nm was observed, showing that Cu^{2+} was reduced to Cu^0 during the hypercritical drying process, which was in good agreement with XRD results.

After calcination, the diffuse reflectance spectra showed strong absorption bands at 240 nm and a broad absorption from 350 nm to 800 nm. The band at 240 nm might be the LMCT band. We assigned the broad absorption to CuO or bulk-like spinel $CuAl_2O_4$ species because both showed absorption in this range. The three-dimensional Cu^+ cluster

in the CuO matrix was also reported to show some absorption in this range (400-500 nm).[9] Since the samples were calcined and the spectra measured in air, the existence of Cu^{+} species was less likely. With the increase of copper loading, the LMCT band shifted to the higher wavelength and the intensity increased, indicating the less tetragonal distortion of the copper species in the octahedral environment.[9] The intensity of the absorption in the 350-800 nm range increased and the strong absorption band between 200 and 300 nm decreased when copper loading increased from 5 to 10 wt%, showing the increase of crystalline and bulk CuO.[6] This was consistent with the observation that the intensities of the XRD peaks increased with the increase of copper loading. The absorption band at 270 nm in the spectrum of the support was also due to metal oxide impurities.

After the thermovacuum treatment, a new absorption band appeared at 320 nm, which was assigned to the electron transition $d^{10} \rightarrow d^{9}s^{1}$ of Cu^{+} species (Cu_2O). Although the 3d orbitals of Cu_2O were fully occupied and no d-d transition band should be observed, Cu_2O could give transitions from the valence band to excited levels involving the emission and absorption of a photon.[9] The appearance of Cu_2O was also observed by XRD. It was obvious that reduction ($Cu^{2+} \rightarrow Cu^{+}$) was not complete from the UV-vis spectra because there still existed Cu^{2+} species absorption band after thermovacuum treatment. The degree of the Cu^{2+} dispersion determined the auto-reducibility. The isolated Cu^{2+} ions were more easily reduced to Cu^{+} in vacuum.[5] This was in good agreement with the results of our adsorption experiments. For adsorbents with copper loadings of 2 and 5 wt%, copper ions were highly dispersed and easy to reduce in

vacuum. The 5 wt% Cu/Al_2O_3 adsorbent showed higher capacity. More aggregates were formed in the case of 10 wt% Cu/Al_2O_3 and Cu^{2+} ions were more difficult to reduce, so capacity was also lower. At the present time, we are not able to quantify the percentage of reduced copper.

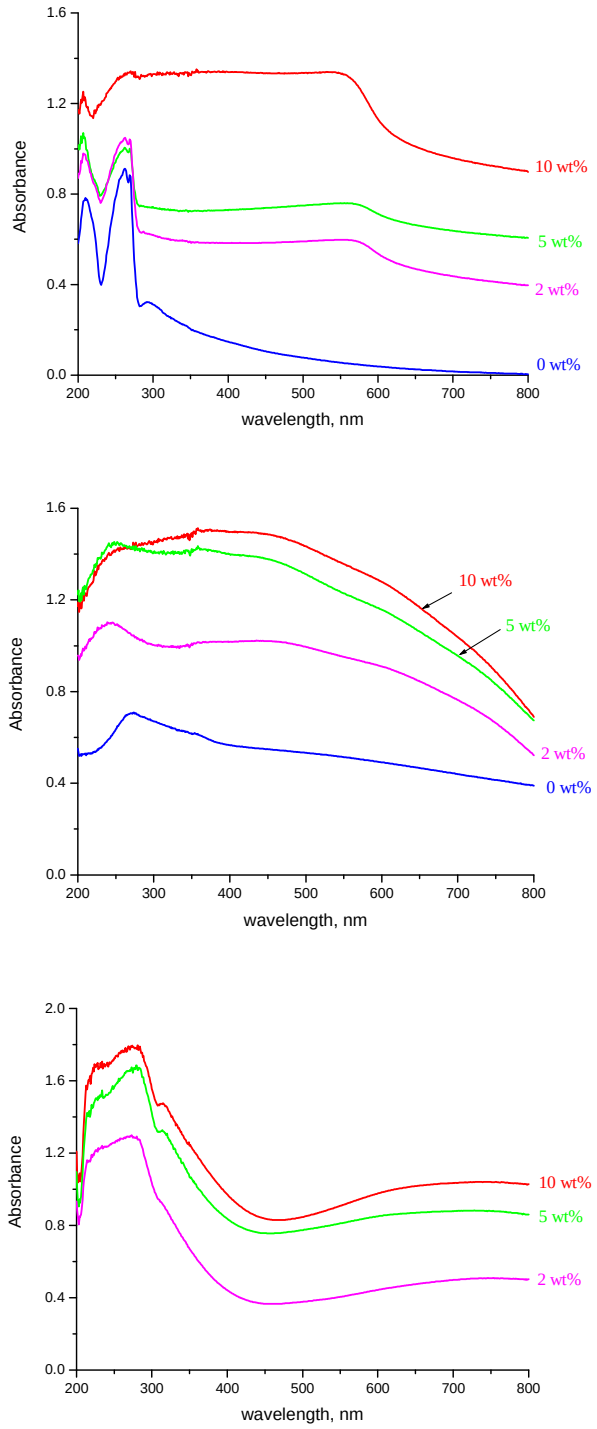

Figure 3.5 Diffuse reflectance UV-Vis spectra of Cu/Al_2O_3 adsorbents with different Cu loadings (a) before calcination, (b) after calcination, and (c) after thermovacuum treatment

3.5.4 FT-IR

Infrared spectroscopy of CO absorption is the widely applied method to obtain information about the oxidation and coordination state of the surface copper atoms/cations. According to the literature[10,11,12,13], CO is bonded via σ- and π-back bonds in Cu^{n+}-CO complexes. Strong σ-type donation of the C lone pair of CO is reinforced by a relevant π-type back bonding from the d orbitals of Cu^{+} to the antibonding orbitals of CO. As a result of the synergistic effect between the two bonds, the Cu^{+}-CO species are characterized by a high stability. In contrast, CO is bonded to Cu^{2+} ions mainly by electrostatic forces and the σ component of the bond is negligible and there is no π back-donation. The carbonyls of Cu^{2+} ions are unstable and are detectable only at low temperature or at high equilibrium CO pressure. The low stability of Cu^{0}-CO is due to both the σ and π components of the Cu^{0}-C bond are weak. It can be concluded that, at room temperature, only Cu^{+} cations form stable complexes; no stable carbonyls are formed with the participation of Cu^{2+} and Cu^{0}. Peak positions of CO adsorbed on Cu have been assigned in the following regions for each oxidation state: the band at 2220-2150 cm^{-1} can be assigned to the Cu^{2+}-CO species. The band at 2160-2080 cm^{-1} can be assigned to CO adsorbed over Cu^{1+} species. The Cu^{0}-CO carbonyls are characterized by absorption frequency below 2130 cm^{-1}.

Figure 3.6 shows the IR spectra of CO adsorbed on the activated samples after exposure to CO followed by purging with helium at room temperature. The adsorption of CO leads to the appearance of a band with a maximum centered at 2110 cm^{-1}. Purging with helium at room temperature causes the decrease of the intensity, while the maximum position of

the band does not shift, showing CO species are strongly bound to the surface. We attribute this to the formation of Cu^{+}-CO complexes. Although bands for Cu^{+}-CO and Cu^{0}-CO complexes overlap, we rule out the possibility of Cu^{0}-CO carbonyl for its weak stability. After purging with O_2 at 473 k, the absorption peak disappears completely; the spectrum is the same as that of the sample before activation. No formation of Cu^{2+}-CO complexes is due to the weakness of the coordination bond.

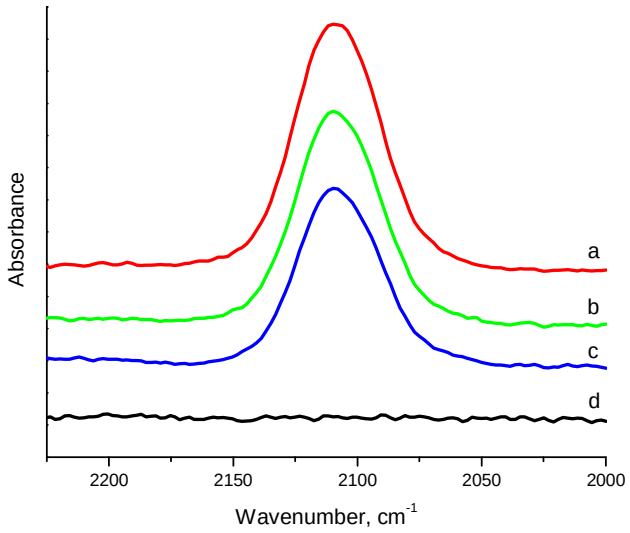

Figure 3.6 IR spectra of CO at room temperature on Cu/Al_2O_3 absorbent (a) after contact with gas, (b) after 1 min purging with He, (c) after 15 min purging with He, (d) after oxidation at 473 K. The spectrum of the adsorbent was subtracted.

3.6 Mechanism of adsorption

Although mechanistic research has been carried out by experiments and simulations, debate continues over the role of metal ions and the identity of the active sites. Thiophene has two lone pairs of electrons on sulfur atom. One pair lies on the six-electron system and the other lies in the plane of the ring. Thiophene can act either as an n-type donor by donating the lone pair of electrons (direct S-M σ bond) or as π-type donor by utilizing the

delocalized electrons of the aromatic ring (π bond) to form π-type complex with the metal ions (Figure 3.7).[27] Based on the molecular orbital theory calculation, Yang et al.[16] suggested the π-complexation mechanism. In this mechanism, the cations can form the usual σ bonds with their s orbitals and, in addition, their d orbitals back-donate electron density to the antibonding π orbitals of the sulfur rings. Song et al.[2] reported that there exists a direct interaction between the metal atom and sulfur atom of the thiophenic molecules, known to be possible with some organometallic complexes. Among the known coordination geometries of thiophene in organometallic complexes, only two types of interaction of thiophene with metal involved sulfur in thiophene (the sulfur atom interacted with one metal atom or two metal atoms). These two possibilities are shown in Figure 3.7.

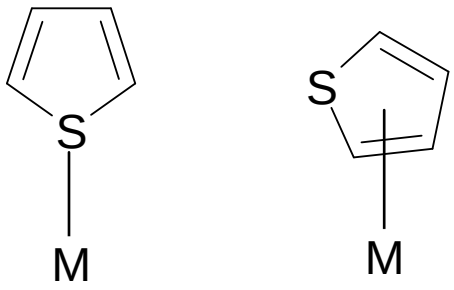

Figure 3.7 Two possible interactions between thiophene and metal ion

Figure 3.8 shows the thiophene adsorption results of three adsorbents: Cu^0/Al_2O_3 (no calcination, heating in vacuum), Cu^{2+}/Al_2O_3 (calcination, heating in air), Cu^+/Al_2O_3 (calcination, heating in vacuum). All three adsorbents had 5 wt% copper loading. Both Cu^{2+} and Cu^0 were ineffective for thiophene removal. Only Cu^+ showed high adsorption capacity towards thiophene. The π-complexation mechanism suggests that Cu^0 could selectively bind to π-system of thiophene and remove it; however, our data does not support this expectation. The inconsistency might be due to the preparation methods,

supports, pretreatments, or the interactions among the coexisting molecules in the fuel. It appears that thiophene coordinated to the metal ion (Cu^{+}) through its sulfur atom in our experiments, but it has not been proven at this point. Based on the difference of NMR chemical shifts between the DBT in the $AgBF_4$-DBT solution and those of the free DBT, McKinley[14] found that DBT coordinated to Ag^{+} through the sulfur atom instead of the arene ring.

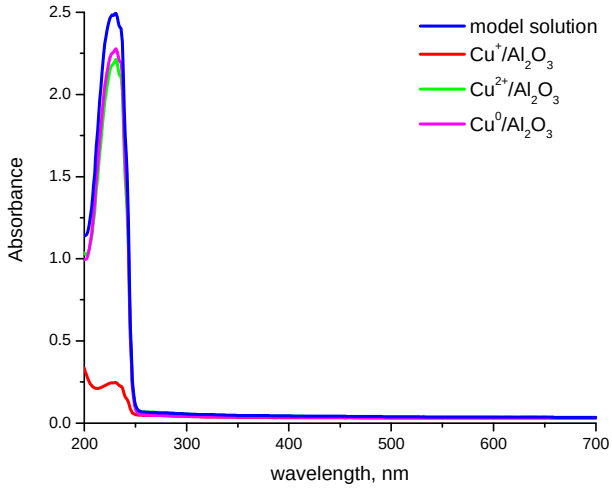

Figure 3.8 Adsorption of thiophene on 5 wt% Cu/Al_2O_3 adsorbent with different Cu oxidation states

3.7 Regeneration of adsorbent

The regeneration of adsorbents after adsorption was studied by heating the adsorbent in vacuum (700 °C, 3 h) to remove the adsorbed sulfur compounds and to reduce Cu^{2+} to Cu^{+}, using 5 wt% Cu/Al_2O_3 adsorbent. In Figure 3.9, the effect of regeneration on adsorption is illustrated. The thiophene uptake reaches more than 95% when the adsorption equilibrium was attained. Even after the second regeneration, the adsorption

capacity is 1.7 mg/g, 95% of the capacity of the fresh adsorbent. Thus, the adsorbent could be easily regenerated without losing its capacity.

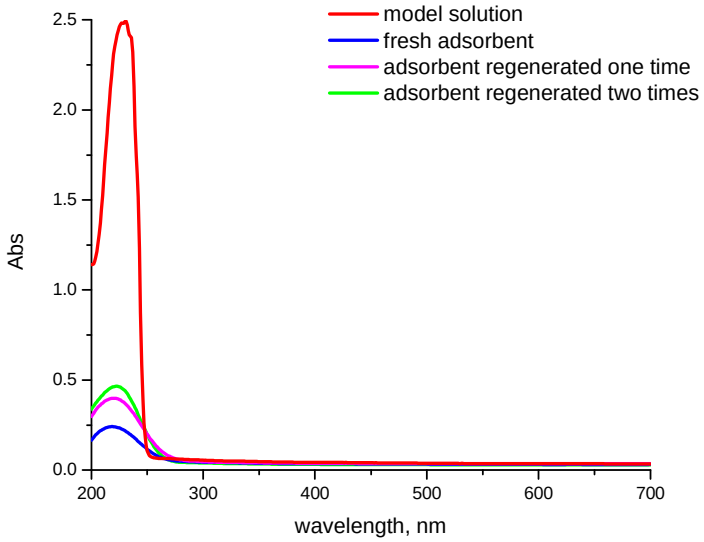

Figure 3.9 Adsorption of thiophene on fresh and regenerated 5 wt% Cu/Al_2O_3 adsorbent

3.8 Conclusions

Sol-gel prepared Cu/Al_2O_3 adsorbents were effective in the removal of thiophene from a hydrocarbon liquid. The adsorption experiments, along with characterization results suggested that Cu^{2+} and Cu^0 did not adsorb thiophene; Cu^+ was the active adsorption site. The kinetic study suggested that the adsorption equilibrium was attained after 1.5 h and most of the adsorption occurred in the first 30 min. The adsorbents had good regenerative properties; 95% of the capacity remains after two adsorption cycles. Future work will investigate the mechanism further, test different sol-gel materials for their thiophene adsorption capacities, and evaluate the adsorbents for desulfurization of real fuels.

References

[1] Z. H. Zhu, H. Y. Zhu, S. B. Wang, G. Q. Lu, Catalysis Letters, 91 (2003) 73

[2] K. Shimizu, H. Maeshima, H. Yoshida, Phys. Chem. Chem. Phys., 2 (2000) 2435

[3] A. J. Hernandez-R. T. Yang, Ind. Eng. Chem. Res., 42 (2003) 123

[4] http://wwwchem.uwimona.edu.jm:1104/courses/copper.html

[5] F. Amano, T. Tanaka, T. Funabiki, J. Mol. Catal. A: Chem., 221 (2004) 89

[6] K. V. R. Chary, G. V. Sagar, D. Naresh, K. K. Seela, B. Sridhar, J. Phys. Chem. B, 109 (2005) 9437

[7] T. Yamamoto, T. Tanaka, R. Kuma, S. Suzuki, F. Amano, Y. Shimooka, Y. Kohno, T. Funabika, S. Yoshida, Phys. Chem. Chem. Phys., 4 (2002) 2449

[8] L. Y. Chen, T. Horiuchi, Applied Catalysis B: Enviromental, 23 (1999) 259

[9] H. Praliaud, S. Mikhalienko, Z. Chajar, M. Primet, Applied Catalysis B: Environmental, 16 (1998) 359

[10] K. Hadjiivanov, H. Knozinger, Phys. Chem. Chem. Phys. 3 (2001) 1132

[11] A. Dandekar, M. A. Vannice, Journal of Catalysis, 178 (1998) 621

[12] M. Turco, G. Bagnasco, U. Costantino, F. Marmottini, T. Montanari, G. Ramis, G. Busca, Journal of Catalysis, 228 (2004) 43

[13] K. I. Hadjiivanov, M. M. Kantcheva, D. G. Klissurski, J. Chem. Soc., Faraday Trans., 92 (1996) 4595

[14] S. G. McKinley, R. J. Angelici, Chem. Commun., 2003, 2620

CHAPTER 4 Zn-based nanoscrystalline Al_2O_3 adsorbent

4.1 Introduction

From the previous chapter, we know that Cu^+ provided active sites for thiophene adsorption and Cu^+ is air-sensitive. Also, the preparation was complicated. So we tried to find a suitable alternative to copper. Zinc is a good option since it has been used in high temperature gas phase desulfurization and zinc-zeolite has been used for liquid phase desulfurization. Therefore, this chapter is devoted to alumina-supported zinc adsorbent, beginning with preparation and characterization of the adsorbent and following with experimental testing of desulfurization activities. In particular, descriptions are provided:

1. To prepare Zn/Al_2O_3 adsorbent with different zinc loading by sol-gel.
2. To characterize the adsorbents.
3. To run the desulfurization experiments and study mechanisms.

4.2 Preparation of Zn/Al_2O_3 adsorbent

The Zn/Al_2O_3 adsorbents were prepared by a xerogel process using zinc acetate and aluminum isopropoxide (98.0 %, Aldrich). The general procedure consisted of the following steps. Aluminum isopropoxide (4.08 g, 0.02 mol) was dissolved in a mixture of 133 ml toluene and 79 ml ethanol. An appropriate amount of zinc acetate necessary to give the desired Zn loading was dissolved in 3 ml deionized water. When this zinc solution was added into the above solution, the hydrolysis started, followed by vigorous stirring at room temperature for 12 h. The final step was to dry the gel at around 70˚C, and the dry powder was ground and saved for later heating and use.

4.3 Characterization of adsorbents

X-Ray powder diffraction (XRD) patterns were obtained with a Bruker D8 diffractometer, using Cu Kα radiation (1.5406Å) at 40 kV and 40 mA and a secondary graphite monochromator. Samples were packed into a plastic holder. The measurements were recorded in steps of 0.04° with a count time of 10 s in the 2θ range of 20-80°. Identification of the phases was made with the help of the Joint Committee on Powder Diffraction Standards (JCPDS) files.

X-ray photoelectron spectroscopy (XPS) data were recorded using a Perkin-Elmer PHI 5400 electron spectrometer. The spectrometer utilizes monochromatized Al *Kα* radiation (1486.6 eV, 15kV×300W). The instrument operates at a pressure of about 2.0×10^{-9} torr. The XPS binding energies were measured with a precision of 0.1 eV. Analyzer pass energy was set to 17.9 eV and the contact time was 50 ms. Before testing the samples, the spectrometer was calibrated by setting the binding energies of the Au $4f_{7/2}$ and Cu $2p_{3/2}$ values to 84.0 and 932.7 eV, respectively. Binding energies for the samples were referenced to the C 1*s* line (284.6 eV).

N_2 adsorption-desorption isotherms were obtained at -196°C using a computer-controlled NOVA 1000 instrument (Quantachrome, USA). Before adsorption, all the samples were degassed for 1 h at 150°C under vacuum. The specific surface areas were estimated by the multi-point Brunauer-Emmet-Teller (BET) method. The Barett-Joyner-Halenda (BJH) method was applied to calculate the pore volume and pore diameter.

Transmission electron microscopy (TEM) measurements were made with a JOEL 2000 EX electron microscope, equipped with a top entry stage. The powder was ultrasonically dispersed in acetone and the suspension deposited on a thin copper grid coated with a porous carbon film that supports the sample to be viewed. The grid was then placed in the electron beam between the filament and a phosphorus plate that lights up as electrons hit the surface. Electrons localized on atoms in the sample would block the passage of the electron beam and appeared as dark areas on an otherwise illuminated image. The residual pressure at the specimen region was approximately 1×10^{-6} mbar.

4.4 Adsorption Experiments

Adsorption experiments were performed by a batch method. 0.3 g adsorbent was put in a heating tube and calcined under vacuum at 500 °C for 3 h, and then the furnace was removed and the heating tube was cooled down to room temperature. 40 ml model fuel consisting of pentane and thiophene (the sulfur level was 20 ppmw) was added and the heating tube was sealed immediately. The mixture was kept at room temperature with vigorous stirring for a desired time, and the liquid phase was separated from the adsorbent. The final weight of different zinc loading adsorbents after the thermal vacuum treatment was in the range of 0.15-0.2 g because of the removal of organic impurities. The sulfur concentration in the solution was monitored by UV-Vis spectrophotometry (thiophene has an absorption band at 231 nm and the absorbance corresponds to the residual thiophene content). The experimental error was about ± 2% based on our reproducible experiments.

4.5 Results and Discussion

Figure 4.1 shows the adsorption results on 10 wt% Zn/Al_2O_3 adsorbent. The intensity of absorbance at 231 nm decreased significantly after adsorption, suggesting that most of the thiophene was adsorbed out of the model fuel. It was clear that zinc-based alumina could be a good adsorbent for use in liquid phase desulfurization at ambient conditions. The capacities of adsorbents with different zinc loadings, which are listed in Table 4-1, show that 20 wt% Zn/Al_2O_3 has the highest capacity. For adsorbents having zinc loading below 20 wt%, the capacity increases with higher zinc loadings. At zinc loading greater than 20 wt%, the capacity decreases.

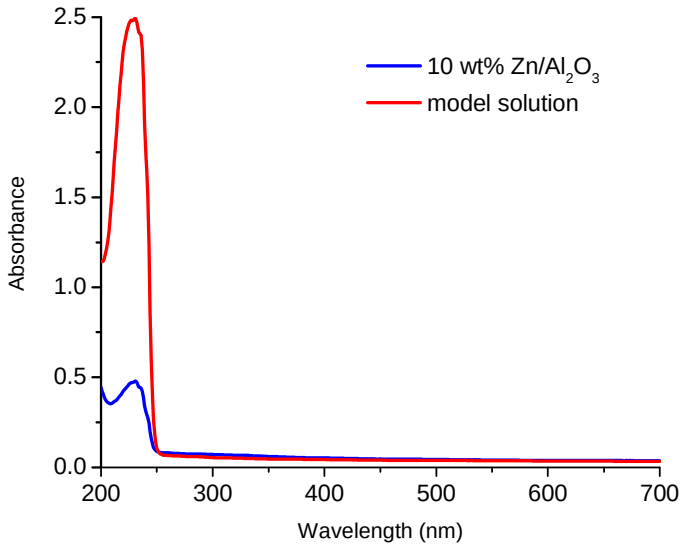

Figure 4.1 Adsorption of thiophene on 10 wt% Zn/Al_2O_3

Table 4-1 Capacities for adsorbents with different zinc loadings (thermal treatment performed under vacuum for all samples)

	Capacity (mg S/g adsorbent)
5 wt% Zn/Al_2O_3	1.5
10 wt% Zn/Al_2O_3	2.0
15 wt% Zn/Al_2O_3	2.2
20 wt% Zn/Al_2O_3	2.8
25 wt% Zn/Al_2O_3	2.3

4.5.1 X-ray diffraction (XRD)

XRD can be used to identify crystalline bulk phases, the crystallinity, and to estimate particle size.[1] It was reported that when transition metal ions were supported on alumina, two reactions occurred concurrently: one led to the formation of a spinel and the other to segregation of an oxide.[2] It was easy to identify the segregated oxide phase by the analysis of the XRD data. The identification of the spinel phases was rather difficult because alumina had a defect spinel structure and its lattice parameters were almost identical to those of the spinel. It was found that the intensities of lines at d=2.4 and 2.8 Å (strong lines for spinel, 2θ = 32, 37˚) increased in the zinc metal ion containing alumina as compared with the pure alumina. Relative intensities of these two diffraction lines were used to identify the formation of the spinel-like structure.[2]

The experimental XRD patterns obtained for different zinc loadings are shown in Figure 4.2. All samples give broad diffraction lines, suggesting low crystallinity. The intensities

of the diffraction lines at about 31.4 and 36.8˚ for zinc-containing samples began to increase relative to the main alumina line (2θ=46.0, 66.8˚). With increased zinc loading, the two lines became narrower and more intense, consistent with formation of a spinel-like phase. Although ZnO had diffraction lines at around 32 and 37˚, other major lines in ZnO patterns (34.4 and 47.5˚) were absent even for higher zinc loading sample (25 wt%, not shown here). However we could not rule out the possible formation of ZnO (the crystallite size of ZnO was small and undetectable as a consequence of sensitivity and size limits of the XRD technique). It was obvious that when calcined in air, the zinc ions interacted strongly with the Al_2O_3 support and formed a "surface spinel" which was similar in structure to bulk $ZnAl_2O_4$. In contrast, only two broad peaks appeared in the pattern when samples were treated under vacuum. The intensity of the broad peak in the 25-40˚ range increased with higher zinc loading relative to peak at 60-75˚. We believe that a surface spinel was also formed during vacuum treatment, but a more defective structure with more exposed zinc ions was formed, which resulted in broader peaks in the XRD pattern. XPS and BET data discussed next show further evidence of the formation of surface spinel and its smaller size.

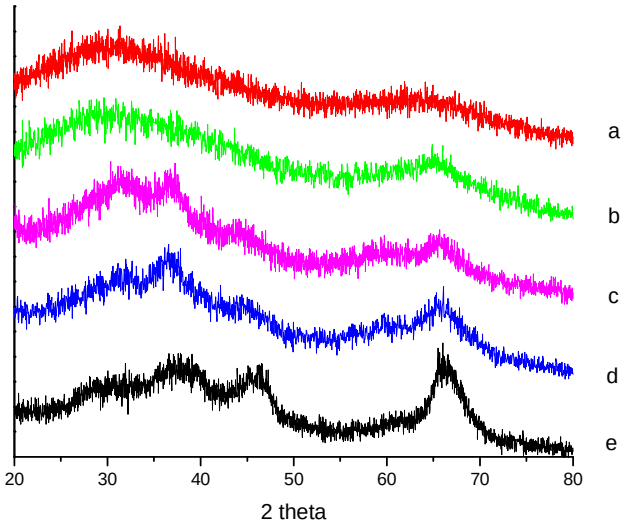

Figure 4.2 X-ray powder diffraction patterns of different zinc loading samples: (a) 20 wt% Zn/Al_2O_3; (b) 10 wt% Zn/Al_2O_3; (c) 20 wt% Zn/Al_2O_3; (d) 10 wt% Zn/Al_2O_3; (e) Al_2O_3 (support); (a and b are samples calcined under vacuum at 500 ˚C for 3 h; c, d, and e are samples calcined in air at 500 ˚C for 3 h)

4.5.2 X-ray photoelectron spectroscopy (XPS)

XPS binding energies provide a means to identify the chemical composition of a sample as well as the difference in the oxidation state and molecular environment of identified elements. The Zn $2p_{1/2}$ and Zn $2p_{3/2}$ lines for 20 wt% Zn/Al_2O_3 with different treatments and reference compounds, Zn and ZnO, are shown in Figure 4.3.

The XPS binding energies for Zn $2p_{1/2}$ and Zn $2p_{3/2}$ were 1045.3 and 1022.2 eV, respectively for the vacuum treatment sample; the respective values were 1045.5 and 1022.3 eV for the air treatment sample. As can be seen, calcination in air or under vacuum resulted in little chemical shift for Zn $2p_{1/2}$ and Zn $2p_{3/2}$ lines, indicating no

change in oxidation state of zinc for these two different thermal treatments. This also suggested that Zn^{2+} was not easily reduced, though auto-reduction of many supported transition metals could occur under vacuum treatment.[3,4,5,6] The binding energies for Zn $2p_{3/2}$ on the two 20 wt% Zn/Al_2O_3 samples were 0.7 eV and 0.8 eV higher than that of ZnO, and 0.9 eV and 1.0 eV higher than that of metallic Zn. The binding energies for both Zn $2p_{3/2}$ and Zn $2p_{1/2}$ lines were virtually identical to the values for $ZnAl_2O_4$ (1022.0 and 1045.1 eV)[7] and in good agreement with formation of a surface spinel (bulk-like $ZnAl_2O_4$) as indicated by XRD.

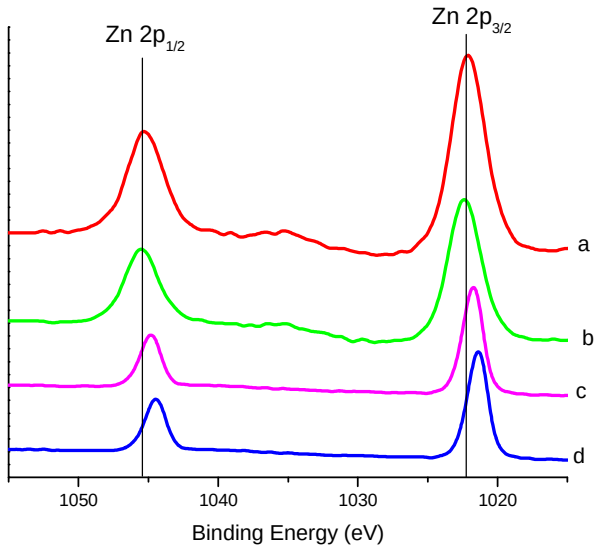

Figure 4.3 XPS spectra of Zn $2p_{3/2}$ and Zn $2p_{1/2}$ for different samples: (a) 20 wt% Zn/Al_2O_3 (500 ˚C, vacuum); (b) 20 wt% Zn/Al_2O_3 (500 ˚C, air); (c) ZnO; (d) Zn

4.5.3 N_2 adsorption-desorption

The results in Table 4-2 show the textural properties of adsorbents. The specific surface area decreases with an overall zinc content increase. The results show that vacuum treatment greatly affected the textural properties of the adsorbent. For an adsorbent with

20 wt% zinc loading, the surface area is about 20 % higher when thermal treatment was conducted under vacuum compared with that in air. In addition, the pore volume was almost the same and pore diameter is smaller, suggesting a smaller particle size. This was also consistent with XRD indications.

Table 4-2 Pore structure of Zn/Al_2O_3 adsorbents

	Surface area (m^2/g)	Pore Volume (cm^3/g)	Pore Diameter (nm)
5 wt% Zn/Al_2O_3 [a]	437	2.0	9
10 wt% Zn/Al_2O_3 [a]	377	1.4	4
20 wt% Zn/Al_2O_3 [a]	336	0.9	4
25 wt% Zn/Al_2O_3 [a]	278	0.8	4
20 wt% Zn/Al_2O_3 [b]	400	1.0	3

thermal treatment: in air (a); under vacuum (b)

4.5.4 Transmission electron microscopy (TEM)

TEM is one of the primary tools of materials chemists and is essential to accurately describe the size, and shape of particles. Electron micrographs of 20 wt% Zn/Al_2O_3 (calcined in air or under vacuum) are shown in Figure 4.4. It can be seen that the prepared samples had agglomerated to form larger particles. The zinc is well dispersed on the surface of the support and the samples consisted of agglomerates of primary particles with an average diameter of ca. 10 nm. There is no visible difference between these two samples with different thermal treatments. A deeper understanding of the difference in the surface structure and the particle size might be obtained with the help of a high resolution TEM.

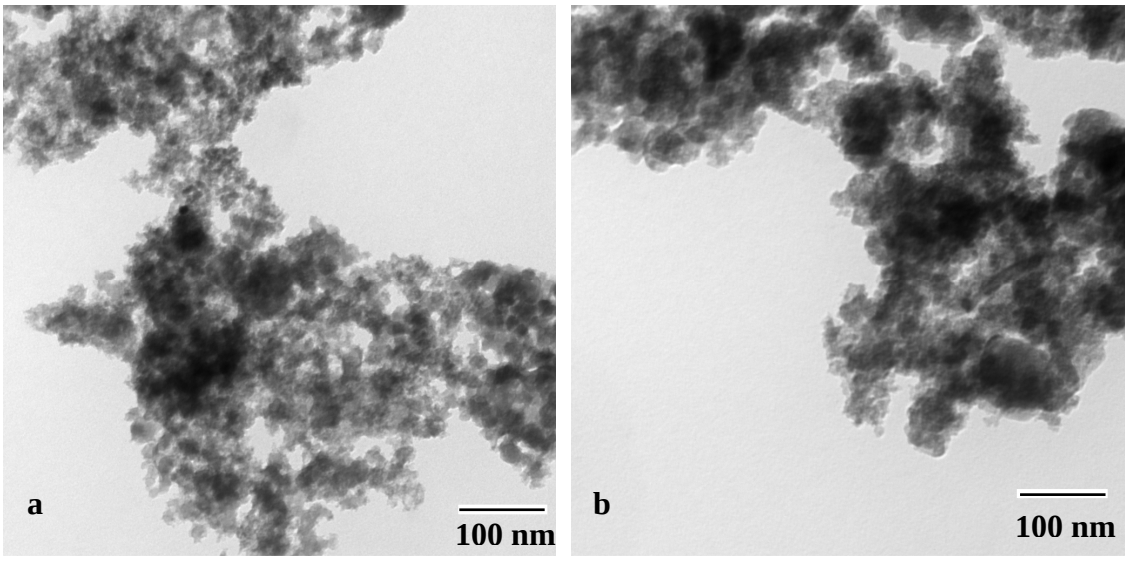

Figure 4.4 Electron micrographs of 20 wt% Zn/Al_2O_3 adsorbent (a) calcined in air and (b) calcined under vacuum

Importance of Vacuum Treatment

Figure 4.5 shows the performance of ZnO and 20 wt% Zn/Al_2O_3 adsorbent with different treatments. It is obvious that pure ZnO did not adsorb thiophene, and vacuum treatment was crucial for the adsorption of thiophene on the zinc-based adsorbents. In order to explain these particularly interesting results for zinc-based adsorbents treated under vacuum, we propose that a less ordered surface $ZnO\text{-}Al_2O_3$ structure is responsible for the adsorption of thiophene from the model fuel. When the thermal treatment was conducted in air, more ordered (crystalline) structure, probably with fewer surface exposed zinc ions, forms. On the other hand, zinc ions mixed less strongly with alumina because of the absence of oxygen when treatment was carried out under vacuum, which resulted in the stronger interaction between zinc ions and thiophene molecules during adsorption. In addition, when zinc loading increaseed from 20 to 25 wt%, the capacity decreased due to the formation of new zinc species, such as ZnO. Zinc ions preferably

diffused into the vacant tetrahedral sites of the alumina lattice. If all of the available lattice sites were saturated, further addition of zinc could be accommodated only by segregation of a separate ZnO phase,[7] which was not very effective for thiophene adsorption.

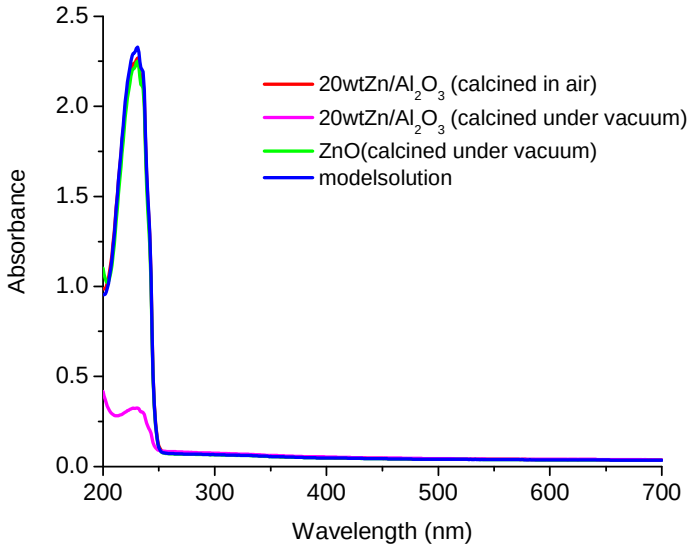

Figure 4.5 Adsorption of thiophene on ZnO and 20 wt% Zn/Al_2O_3 with different treatments

4.6 Adsorbent regeneration

The 20 wt% Zn/Al_2O_3 adsorbent was tested for regeneration after one adsorption cycle. The regeneration was achieved by heating the spent adsorbent at 500˚C for 1 h under vacuum to remove the adsorbed thiophene molecules. After the regeneration was completed, the adsorbent was mixed with fresh model solution at room temperature and the second adsorption cycle was performed. Figure 4.6 shows that more than 96 %

desulfurization capacity is recovered with the regeneration scheme. Thus, the adsorbent could be easily regenerated without losing capacity.

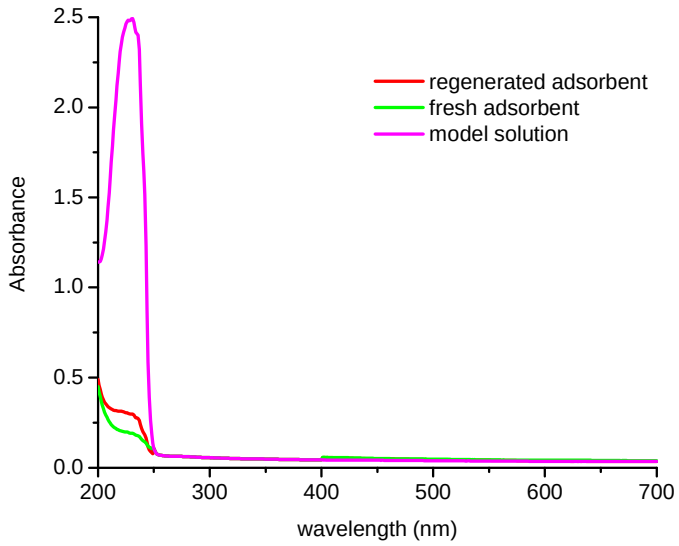

Figure 4.6 Adsorption of thiophene on fresh or regenerated 20 wt% Zn/Al_2O_3 adsorbent

4.7 Conclusions

Xerogel prepared zinc-based nanocrystalline alumina adsorbents have been demonstrated to be effective in the liquid phase desulfurization at room temperature and pressure based on the batch method. Surface spinel was formed during thermal treatment because of the interaction between zinc ions and alumina. Compared with thermal treatment conducted in air, thermal vacuum treatment created a more defective structure with weaker interaction between zinc ions and alumina support, which resulted in the possibility of stronger interaction between zinc ions and thiophene molecules in the adsorption process and the removal of thiophene from the hydrocarbon solution. The experimental results showed the excellent regenerative property of the adsorbent by a simple regeneration scheme.

References

[1] B. E. Warren, X-ray Diffraction, Addison-Wesley, 1969

[2] M. Lo Jacono, M. Schiavello, Preparation of Catalysts, Elsevier, Amsterdam, 1976

[3] A. J. Hernandez-Maldonado, R. T. Yang, Catalysis Reviews, 46 (2004) 111

[4] R. T. Yang, Adsorbents: Fundamentals and Applications, Wiley, New York, 2003, Chap. 10

[5] A. J. Hernandez-R. T. Yang, Ind. Eng. Chem. Res., 42 (2003) 123

[6] X. Yang, L. Erickson, K. Hohn, P. Jeevanandam, K. Klabunde, Ind. Eng. Chem. Res., 45 (2006) 6169

[7] B. R. Strohmeier, D. M. Hercules, Journal of Catalysis 86 (1984) 266

CHAPTER 5 Review on photocatalysis

5.1 Introduction

In 1972, Fujishima and Honda discovered the photocatalytic splitting of water into hydrogen and oxygen under ultraviolet (UV) irradiation on a TiO_2 electrode. Since then, photocatalysis, through the use of semiconductor powders, has drawn much attention for its potential in the conversion of light energy into chemical energy.[1,2,3,4] In recent years, photocatalysis has also been actively used in environmental applications, since the semiconductor can be photoexcited to form electron-donor sites (reducing sites) and electron-acceptor sites (oxidizing sites), providing redox reagents which can drive the degradation of organic compounds in polluted air and water.

Semiconductors can act as sensitizers for light-induced redox processes owing to their electronic structure, which is characterized by a filled valence band (VB) and an empty conduction band (CB).[5] As illustrated in Figure 5.1, a photon with an energy (hν) corresponding to or exceeding the band gap energy (Eg) of the semiconductor provides excitation, an electron (e_{cb}^-) is promoted into the conduction band, leaving a hole (h_{vb}^+) in the valence band. Several pathways can occur for the departed electrons and holes. They can recombine together on the surface (pathway A) or in the volume of semiconductor particle (pathway B) and dissipate the input energy as heat. The electron and hole can migrate to the surface. At the surface, electrons can be donated to electron acceptors (pathway C) while holes can get electrons from electron donors and oxidize the donor species (pathway D).

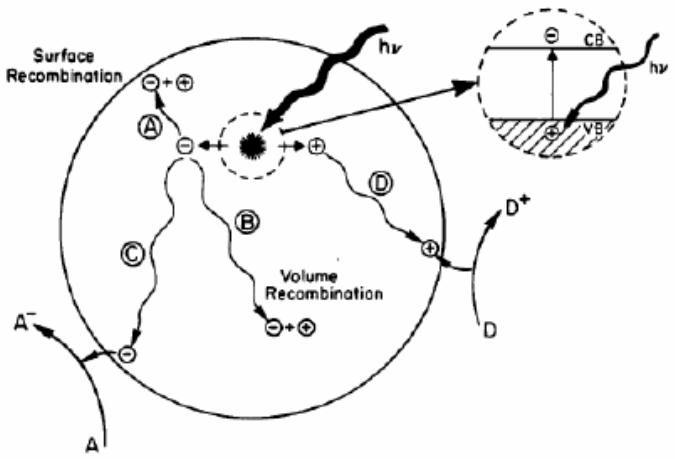

Figure 5.1 Schematic photoexcitation in a solid followed by deexcitation events[3]

5.2 Efficiency of photocatalytic process

The efficiency of the photocatalytic process is measured as a quantum yield which is defined as the number of events occurring per photon absorbed. The ability to measure the actual absorbed light is very difficult in heterogeneous systems due to scattering of light by the semiconductor surface. It is usually assumed that all the light is absorbed and the efficiency is quoted as an apparent quantum yield. If several products are formed from the photocatalytic reaction then the efficiency is sometimes measured as the yield of a particular product. To determine the efficiency or quantum yield, a combination of all the pathway probabilities for the electron and hole must be considered. The quantum yield for an ideal system, ø, given by the simple relationship:

$$\phi \propto \frac{k_{CT}}{k_{CT} + k_R}$$

As seen in this equation, ø is proportional to the rate of the charge transfer processes (k_{CT}) and inversely proportional to the sum of the charge transfer rate (k_{CT}) and the electron-hole recombination rate (k_R) both inside the volume and on the surface of

semiconductor. It is clear that electron and hole recombination is detrimental to the efficiency of a semiconductor photocatalyst. Many efforts have been made to retard the recombination of holes and electrons within the semiconductor particle and promote charge transfer at the semiconductor surface, thereby increasing the quantum yield of the photocatalytic process.

5.3 Electronic band structure in semiconductor for photocatalysis

The ability of a semiconductor to undergo photoinduced electron transfer to adsorbed species on its surface is governed by the band energy positions of the semiconductor and the redox potentials of the adsorbate. Thermodynamically, the relevant potential level of the acceptor species is required to be below (more positive than) the conduction band potential of the semiconductor. The potential level of the donor needs to be above (more negative than) the valence band position of the semiconductor in order to donate an electron to the vacant hole. The band edge positions of several semiconductors are presented in Figure 5.2. The internal energy scale is given on the left for comparison to the vacuum level and on the right for comparison to the normal hydrogen electrode (NHE). The positions are derived from the flat band potentials in a contact solution of aqueous electrolyte at pH=1.0. The pH of the electrolyte solution influences the band edge positions of the various semiconductors compared to the redox potentials for the adsorbate.

Among those semiconductors in Figure 5.2, TiO_2 has been considered as the most promising photocatalyst for its biological and chemical inertness, stability with respect to

photo- and chemical corrosion, and relative inexpensiveness.[6,7,8] Although ZnO seems to be a suitable alternative to TiO_2 since it has the same value of band gap, it degrades during the repeated catalytic cycles usually involved in heterogeneous photocatalysis and can therefore not be used for technical applications. Other semiconductors, such as CdS, absorb larger fractions of the solar spectrum than TiO_2 and can form chemically activated surface-bond intermediates, but unfortunately, such catalysts suffer from photocorrosion induced by self-oxidation, leading to depressed photoactivity and the release of potential dangerous metal ions, such as Cd^{2+}.

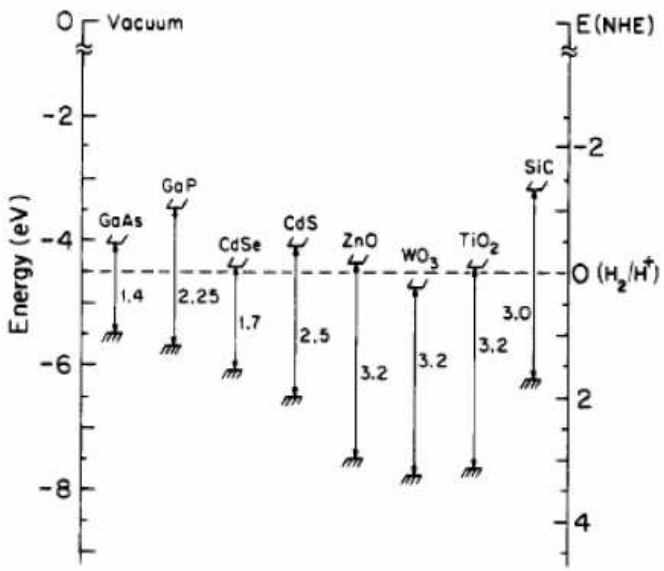

Figure 5.2 Energies for various semiconductors in aqueous electrolytes at pH = 1[3]

5.4 Photocatalysis on TiO_2

Two different crystal structures of TiO_2, rutile and anatase, are commonly used in photocatalysis, with anatase showing a higher photocatalytic activity.[9] Figure 5.3 shows the unit cell structures of the rutile and anatase TiO_2. Both structures can be described in terms of chains of TiO_6 octahedra. The two crystal structures differ by the distortion of

each octahedron and by the assembly pattern of the octahedral chains. Each Ti^{4+} ion is surrounded by an octahedron of six O^{2-} ions. The octahedron in rutile is not regular, showing a slight orthorhombic distortion. The octahedron in anatase is significantly distorted so that its symmetry is lower than orthorhombic. The Ti-Ti distances in anatase are greater whereas the Ti-O distances are shorter than in rutile. In the rutile structure each octahedron is in contact with 10 neighbor octahedrons (two sharing edge oxygen pairs and eight sharing corner oxygen atoms), while in the anatase structure each octahedron is in contact with eight neighbors (four sharing an edge and four sharing a corner). These differences in lattice structures cause different mass densities and electronic band structure between the two forms of TiO_2. The band gap energies are approximately 3.2 eV for anatase and 3.0 eV for rutile. Anatase is thermodynamically less stable than rutile, but its formation is kinetically favored at low temperature (<600 °C), which could explain its higher surface area, and its higher surface density of active sites for adsorption and for catalysis.

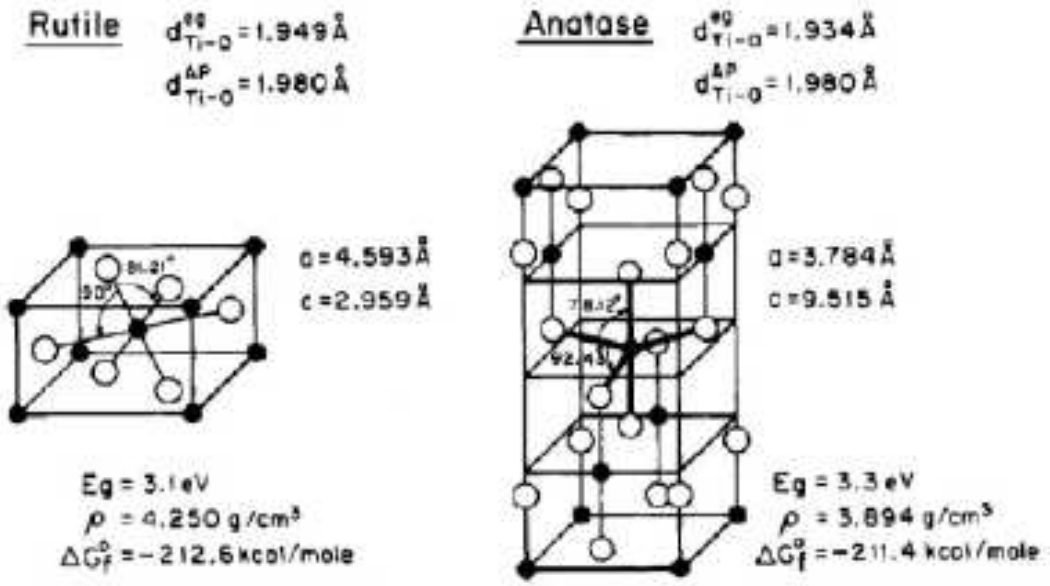

Figure 5.3 Lattice structure of rutile and anatase TiO_2[1]

As shown in Figure 5.4, after the absorption of UV radiation (<387 nm), the initial step is the generation of electrons and holes separated between the conduction and valence band.

$$TiO_2 + h\nu \rightarrow TiO_2 (e^- + h^+)$$

The holes are proposed to oxidize the surface adsorbed hydroxyl ion or water, forming hydroxyl radicals.

$$TiO_2 (h^+) + {}^-OH_{ad} \rightarrow TiO_2 + {}^{\bullet}OH_{ad}$$

$$TiO_2 (h^+) + H_2O \rightarrow TiO_2 + {}^{\bullet}OH_{ad} + H^+$$

$${}^{\bullet}OH + R \rightarrow \text{intermediates} \rightarrow\rightarrow CO_2 + H_2O$$

Electrons are believed to react with surface adsorbed molecular oxygen to produce superoxide anion, $O_2^{\bullet-}$, which can react with its protonated form to generate hydrogen peroxide and hydroxyl radicals.

$$TiO_2 (e^-) + O_2 \rightarrow TiO_2 + O_2^{\bullet-}$$

$$O_2^{\bullet-} + H^+ \rightarrow HO_2^{\bullet}$$

$$O_2^{\bullet-} + HO_2^{\bullet} \rightarrow {}^{\bullet}OH + O_2 + H_2O_2$$

$$2\, HO_2^{\bullet} \rightarrow O_2 + H_2O_2$$

It has been shown that hydrogen peroxide considerably enhance the photodegradation.

$$TiO_2 (e^-) + H_2O_2 \rightarrow TiO_2 + OH^- + {}^{\bullet}OH$$

Most photodegradation of organic compounds can be attributed to the high oxidizing power of hydroxyl radicals. After a series of reactions, organic compounds are finally degraded into CO_2 and H_2O.

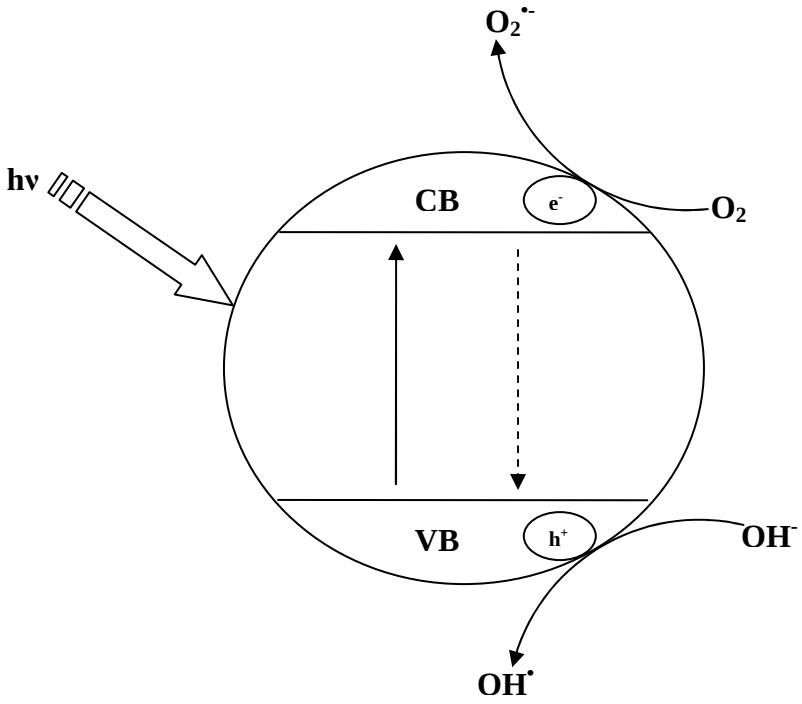

Figure 5.4 TiO_2 photocatalysis process

5.4.1 Limitations of TiO_2 and surface modification

Application of TiO_2 in the remediation of contaminants has been successful for a wide variety of compounds. However, as shown in Figure 5.5, TiO_2 shows poor absorption of visible light, which constitutes 45% of solar energy and 90% of indoor light; it can only use about 5% of solar energy that reaches the earth, since it requires UV activation due to its large band gap.

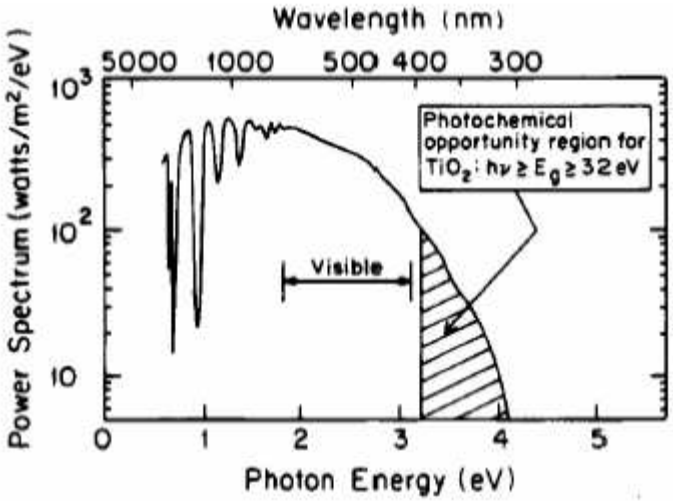

Figure 5.5 Solar spectrum at sea level with the sun at zenith[1,3]

Significant effort has been directed towards the shift of optical response of TiO_2 from UV to visible light region through modifications to TiO_2 surfaces, including addition of metal, dopants, surface sensitization, and combinations with other lower band gap semiconductors. These modifications are beneficial in decreasing the recombination rate of electrons and holes, indicating increased quantum yield of photocatalytic process.

(1) Metal semiconductor modification

In photocatalysis the addition of noble metals to a semiconductor can change the photocatalytic process by changing the semiconductor surface properties. The metal can enhance the yield of a particular product or the rate of the photocatalytic reaction. The addition of a metal to a semiconductor surface can also change the reaction products.

Figure 5.6 is an illustration of the electron capture properties at the Schottky barrier of the metal in contact with a semiconductor surface. The picture illustrates the small area of the semiconductor surface that the metal actually covers.

Transmission electron microscopy measurements have found that when the added metal is Pt, the Pt particles form clusters on the surface. After excitation the electron migrates to the metal where it becomes trapped and electron-hole recombination is suppressed.

The migration of electrons to the metal particles was confirmed by studies showing the reduction in the photo conductance of the semiconductor for the Pt deposited TiO_2 compared to TiO_2 alone. The hole is then free to diffuse to the semiconductor surface where organic species are oxidized. The metal is important because of its modification on the semiconductor by changing the distribution of electrons, i.e., the decrease in electron density within the semiconductor. This leads to an increase in the hydroxyl group and therefore affects the photocatalytic process on the semiconductor surface. Because of the catalytic activity of Pt, Pt/TiO_2 was the most commonly studied metal-semiconductor system for photocatalytic reactions with evolving gas, especially hydrogen.

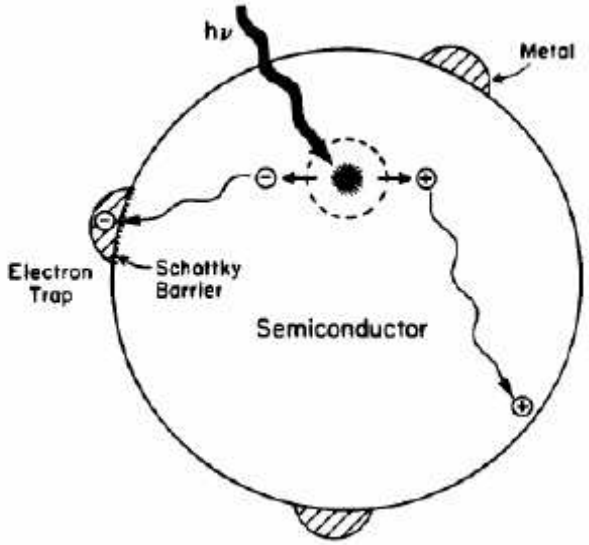

Figure 5.6 Metal-modified semiconductor photocatalyst particle[3]

(2) Composite semiconductors

Coupled semiconductor photocatalysts provide an interesting way to increase the efficiency of a photocatalytic process by increasing the charge separation, and extending the energy range of photoexcitation for the system. Figure 5.7 illustrates the photoexcitation process for the composite (coupled) semiconductor photocatalyst CdS-TiO_2. The energy of the excitation light is too small to directly excite the TiO_2 portion of the photocatalyst, but it is large enough to excite an electron from the valence band across the band gap of CdS (E_g = 2.5 eV) to the conduction band. The hole produced in the CdS valence band from the excitation process remains in the CdS particle while the electron transfers to the conduction band of the TiO_2 particle. The electron transfer from CdS to TiO_2 increases the charge separation and efficiency of the photocatalytic process. The separated electron and hole are then free to undergo electron transfer with adsorbates on the surface. The coupling of semiconductors with the appropriate energy levels can produce a more efficient photocatalyst via better charge separation.

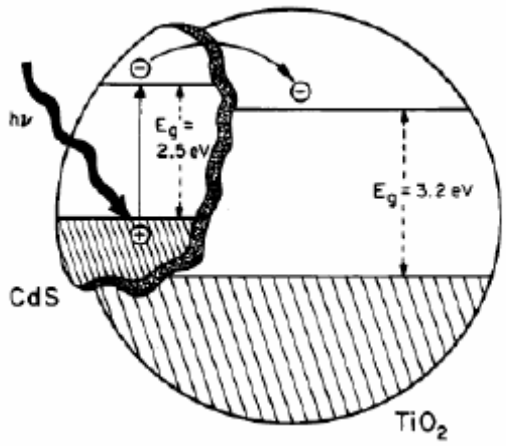

Figure 5.7 Photoexcitation in composite semiconductor photocatalyst[3]

(3) Surface sensitization

Surface sensitization of a wide band-gap semiconductor photocatalyst (TiO_2) via

chemisorbed or physisorbed dyes can increase the efficiency of the excitation process.

The photosensitization process can also expand the wavelength range of excitation for the photocatalyst through excitation of the sensitizer followed by charge transfer to the semiconductor. Figure 5.8 illustrates the excitation and charge injection steps involved for the regenerative dye sensitizer surface process. Excitation of an electron in the dye molecule occurs to either the singlet or triplet excited state of the molecule**.** If the oxidative energy level of the excited state of the dye molecule with respect to the conduction band energy level of the semiconductor is favorable (i.e., more negative), then the dye molecule can transfer the electron to the conduction band of the semiconductor. The surface acts as a quencher accepting an electron from the excited dye molecule. The electron in turn can be transferred to reduce an organic acceptor molecule adsorbed on the surface.

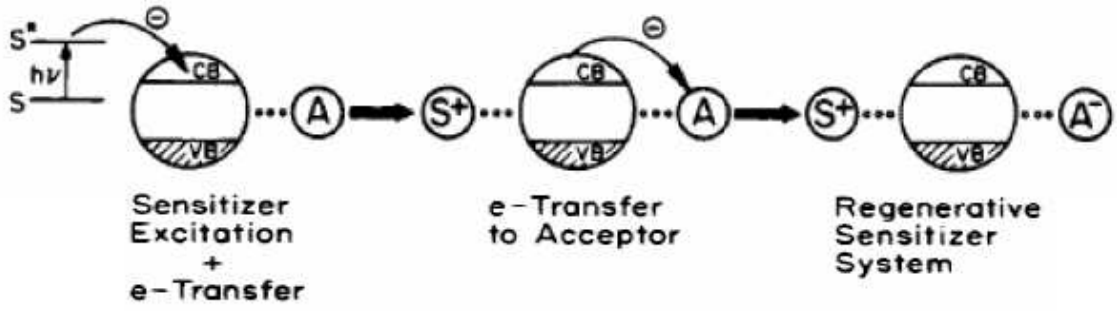

Figure 5.8 Excitation steps using dye molecule sensitizer[3]

(4) Transition metal doping

The influence of dissolved transition metal impurity ions on the photocatalytic properties of TiO_2 has become another interesting area of semiconductor modification. Different metals have been employed to tune the electronic structure of TiO_2-based material. The benefit of transition metal doping species is the improved trapping of electrons to inhibit

electron-hole recombination during illumination. Metal-ion-implantation method with various transition metal ions, including V, Cr, Mn, Fe, and Ni, enabled a large shift in the absorption band of TiO_2 toward the visible light region and V showed the highest effectiveness in the red-shift.[4] Choi et al.[10] systematically studied TiO_2 nanoparticles doped with 21 metal ions by the sol-gel method and discovered the presence of metal dopants significantly influenced the photoreactivity, charge carrier recombination rates, and interfacial electron-transfer rate. The photoreactivity of doped TiO_2 appeared to be a complex function of the dopant concentration, the energy level of dopants within the TiO_2 lattice, their d electronic configuration, the distribution of dopants, the electron donor concentration, and the light intensity.[10] Plasma-enhanced chemical vapor deposition (CVD) was used to synthesize Sn-doped TiO_2 and the doped catalyst had more surface defects on the surface.[11] Wang et al. prepared Fe-doped TiO_2 through oxidative pyrolysis of liquid-feed organometallic precursors and found that iron dopant significantly promoted the transformation of anatase to rutile phase.[12] The photocatalytic reactivity of metal-doped TiO_2 depends on many factors, including the dopant concentration, the energy level pattern of the dopants within the TiO_2 lattice, their d-electronic configuration, and the distribuion of the dopants.

(5) Non-metal atom doping

Non-metal atoms, such as C, N, S, and F, have been successfully doped into TiO_2 catalyst. C-doped TiO_2 has been synthesized by hydrolysis of titanium isopropoxide in a urea and/or thiourea solution or by oxidative annealing of titanium carbide or by direct burning of titanium metal sheet in a natural gas flame or by calcination of the mixture of thiourea, urea, and TiO_2 powder.[6,13,14,15] The chemical state of carbon dopant was

different for each different method. Oxidation of TiC or burning Ti metal in natural gas flame resulted in the substitution of oxygen atom by carbon, while the wet chemical method induced elemental carbon inside the bulk of TiO_2 and carbonate species was doped into TiO_2 lattice by the calcination of mixed powder. The carbon substitution or doped elemental carbon or carbonate species caused the absorbance edge of TiO_2 to be shifted to the visible light region.

S-doped TiO_2 was obtained by mixing titanium isopropoxide with ethanol containing thiourea or by heating sulfide powder or by ion-implanting with S^+ ion flux.[16,17,18,19] Direct oxidation of titanium sulfide induced the S^{2-} anion into the lattice of TiO_2 and sulfur cation (S^{4+} or S^{6+}) was introduced from thiourea. Theoretical calculations showed that the mixing of the S 3p states with the valence band contributed to an increase in the width of the valence band, leading to the band gap narrowing in the sulfur anion doped TiO_2. The absorption of sulfur cation doped TiO_2 in the visible light region was much stronger than that of sulfur anion doped TiO_2.

N-doped TiO_2 was prepared by heating TiO_2 with NH_3 flux at 500-600 ºC or by hydrolysis of titanium isopropoxide in an amine solution and the post treatment of the TiO_2 sol with amines or by mixing titanium isopropoxide with ethanol containing thiourea.[20,21,22,23] High temperature annealing of TiO_2 resulted in less than 2% nitrogen incorporation, while direct amination of titania particles enhanced nitrogen concentration up to 8%.The visible light response was usually attributed to the narrowing band gap, which was due to either the mixing of N p states and O 2p states[24]or the introduction of

the formed N-induced midgap level lightly above the oxygen 2p valence band[25,26] or some impurity species (NO_x or NH_x).[7,27] F-doped TiO_2 catalyst was synthesized by mixing titanium isopropoxide with ethanol containing H_2O-NH_4F or by spray pyrolysis from an aqueous solution of H_2TiF_6.[28,29,30] Photoluminescence (PL) spectra revealed oxygen vacancies (F and F^+) were formed by F-doping and the visible photocatalytic activity was ascribed to the creation of these oxygen vacancies. The effect of transition metal and nonmetal atoms on TiO_2 catalyst was also studied. Zhao et al.[31] prepared a visible-light-driven $Ni_2O_3/TiO_{2-x}B_x$ photocatalyst; the incorporation of boron atoms into TiO_2 extended the spectral response to the visible light region, and the loaded Ni_2O_3 species acted as electron traps and thus facilitated the charge separation. Lanthanum and nitrogen were reported to enhance the degradation of methyl orange. The substitution of nitrogen for oxygen was responsible for the band gap narrowing of TiO_2, and La^{3+} doping prevented the aggregation of powder in the process of preparation.[32]

5.4.2 Particle size effect

As discussed before, the recombination of e^-/h^+ inside the volume of a semiconductor or on the surface is detrimental to the photocatalytic efficiency. Volume recombination is a dominating process in well-crystallized large TiO_2 particles[10], which can be decreased by reducing particle size. Therefore, a higher photonic efficiency can be obtained from a higher interfacial charge carrier transfer rate. However, when the particle size becomes extremely small, surface recombination becomes an important process. In the regime of ultrafine particle size, most of the e^-/h^+ pairs are generated sufficiently close to the surface that they may quickly reach the surface, and undergo rapid surface recombination mainly due to abundant surface trapping sites and the lack of driving force for e-/h+

separation. Since the characteristic time for surface e^-/h^+ recombination is much faster than that of the interfacial charge carrier transfer processes, the increase in the interfacial transfer rate will be out-weighed by the increased surface recombination rate in ultrafine particles beyond a certain size. Therefore, an optimal particle size may exist. Evidence showed that photo reactivity of pure TiO_2 increases when particle size is reduced from 21 to 11 nm, but decreases when it is further reduced to 6 nm.[33] Serpone et al. studied the lifetime of e-/h+ pairs in nanocrystalline TiO_2 particles with different sizes by transient photoabsorption spectroscopy and found that TiO_2 particles with a diameter of 13.3 nm had the longest emission decay time.[34]

The existence of optimal dopant concentration is also expected for transition metal doped TiO_2. It is accepted that Fe^{3+} doping increases the photocatalytic efficiency as Fe^{3+} acts as shallow trapping sites for the charge carriers, thereby trapping one charge carrier of the e^-/h^+ pair temporarily, while the other migrates to the surface first and transfers to the adsorbate (oxidant for e^- and reductant for h^+), with the trapped charge carrier migrating to the surface soon afterward for reaction as well. At low concentration below the optimal value, photoreactivity increases with an increasing dopant concentration because there are fewer trapping sites available. At higher concentration than the optimal value, a h^+ or e^- maybe trapped more than once on its way to the surface so that its apparent mobility way became extremely low and it will likely recombine with e^- or h^+ generated by subsequent photons before it can reach the surface.

Also, with a smaller particle size, the surface area of the particle increases, implying more reactants could be possibly adsorbed on the surface. The electron transfer process is more efficient if the reactants are spread and adsorbed on the surface.[35]

5.4.3 Optical property of transition metal doped TiO_2 nanomaterials

A visible light absorption was usually observed in metal-doped TiO_2 and the absorption was attributed to the charge-transfer transition between the d electrons of the dopant and the conduction or valence band of TiO_2. Figure 5.9 shows the UV-vis absorption spectra of Cr-ion-implanted TiO_2.[4] It is clear that the absorption shifts toward the visible light region and the extent of the red shift is related to the amount of Cr ion implanted. Chemically Cr-doped TiO_2 showed no shift in the absorption edge of TiO_2; however, a new absorption band appeared as a shoulder peak around 420 nm was attributed to the formation of an impurity level within the band gap, with intensity increasing with the number of chemically doped Cr ions.

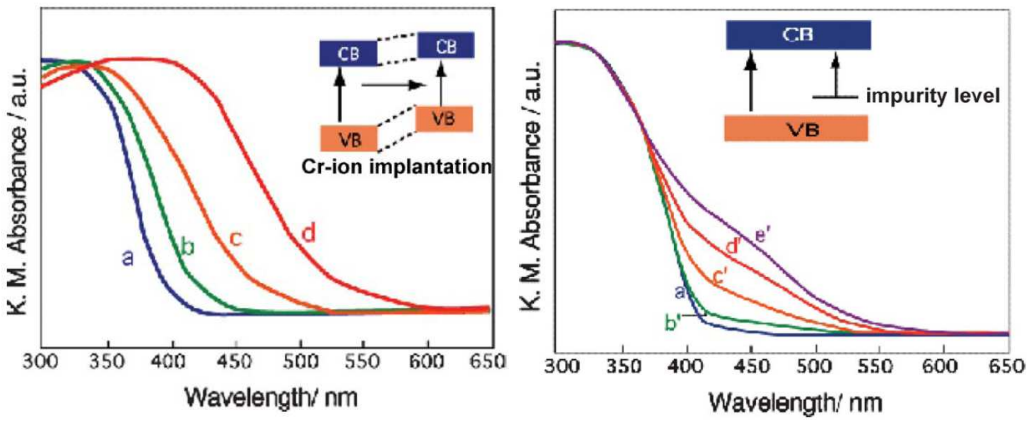

Figure 5.9[4] The UV-vis absorption spectra of TiO_2 (a) and Cr ion-implanted TiO_2 photocatalysts (b-d). the number of implanted Cr ions (μmol/g): (a) 0, (b) 0.22, (c) 0.66, (d) 1.3. (B) The UV-vis absorption spectra of TiO_2 (a) and Cr-doped TiO_2 (b'-d') prepared by an impregnation method. The amount of doped Cr ions (wt%) was (a) 0, (b') 0.01, (c') 0.1, (d') 0.5, (e') 1

Umebayashi et al.[36] analyzed the electronic structure of TiO_2 doped 3d transition metals (V, Cr, Mn, Fe, Co, and Ni) by ad initio band calculation based on the density functional theory. They found that the t_{2g} state of the dopant played a significant role in the photoresponse of TiO_2 under visible light irradiation. The visible light absorption of V-doped TiO_2 was due to the transition between the valence band and the V t_{2g} level and it was attributed to the optical transition from the impurity band tail into the conduction band. The visible light absorption for Cr-doped TiO_2 was due to a donor transition from the Cr t_{2g} level into the conduction band and the acceptor transition from the valence band to the Cr t_{2g} level.

5.4.4 Optical property of non-metal atom doped TiO_2

Figure 5.10 shows UV-vis absorption spectra of N-doped TiO_2 and S^{4+}-doped TiO_2, respectively. The band gap absorption onset of N-doped TiO_2 shifts toward 600 nm from 380 nm for the undoped TiO_2. The S^{4+}-doped TiO_2 also exhibits strong absorption in the visible light region from 400 nm to 600 nm. With the increase of the calcination temperature above 500 ºC, the absorption in the visible light region decreases gradually. When it reaches 700 ºC, the absorption decreases drastically. The shift from UV to visible light region for doped TiO_2 points to the narrowing of band gap, which enhances its photosensitivity.

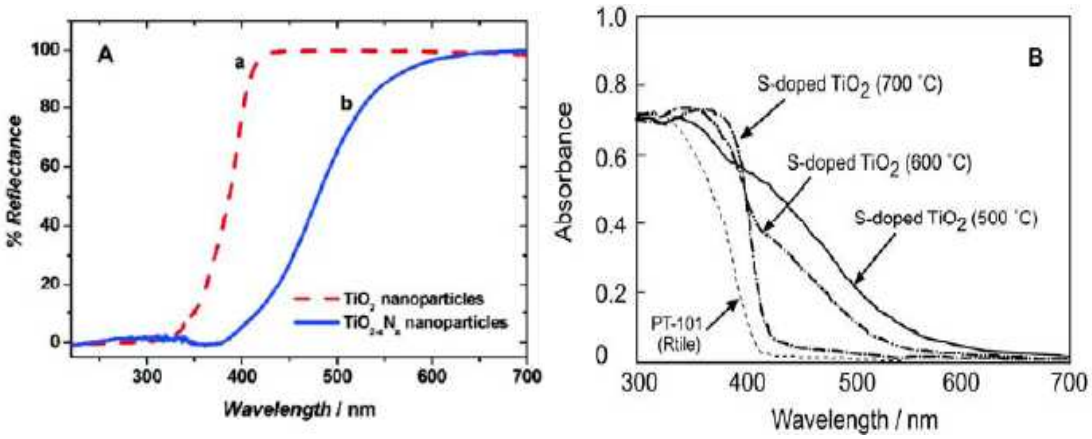

Figure 5.10 (A) Reflectance spectra of N-doped TiO_2 and pure TiO_2[20] (B) Diffuse reflectance spectra of S-doped TiO_2 and TiO_2[17]

5.5 Goal of this research

From the above discussion, in order to shift the optical response of TiO_2 from UV to visible light region and improve the photocatalytic efficiency, transition metal ions or nonmetal atoms can be incorporated into the lattice of TiO_2. Therefore, the goal of this research is to develop highly visible-light-active photocatalysts, namely nano-sized TiO_2 doped catalysts with transition metal (V) and nonmetal atom (C), that can efficiently use solar or indoor light with applications in the environmental and energy field.

References

[1] X. Chen and S. S. Mao, Chem. Rev., 107 (2007) 2891

[2] M. A. Fox and M. T. Dulay, Chem. Rev., 93 (1993) 341

[3] A. L. Linsebigler, G. Lu, and J. T. Yates Jr., 95 (1995) 735

[4] M. Anpo, S. Dohshi, M. Kitano, Y. Hu, M. Takeuchi, and M. Matsuoka, Annu. Rev. Mater. Res., 2005 1

[5] M. R. Hoffmann, S. T. Martin, W. Choi, and D. W. Bahnemann, Chem. Rev., 95 (1995) 69

[6] X. Yang, C. Cao, K. Hohn, L. Erickson, R. Maghirang, D. Hamal, and K. Klabunde, Journal of Catalysis, 252 (2007) 296

[7] O. Diwald, T. L. Thompson, T. Zubkov, Ed. G. Goralski, S. D. Walck, and J. T. Yates Jr., J. Phys. Chem. B, 108 (2004) 6004

[8] R. Nakamura, T. Tanaka, and Y. Nakato, J. Phys. Chem. B, 108 (2004) 10617-10620

[9] J. Augustynski, J. Electrochim. Acta, 38 (1993) 43

[10] W. Choi, A. Termin, and M. R. Hoffmann, J. Phys. Chem., 98 (1994) 13669

[11] Y. Cao, W. Yang, W. Zhang, G. Liu, and P. Yue, New J. Chem., 28 (2004) 218

[12] X. Wang, J. Li, H. Kamiyama, M. Katada, N. Ohashi, Y. Moriyoshi, T. Ishigaki, J. Am. Chem. Soc., 127 (2005) 10982

[13] T. Ohno, T. Tsubota, K. Nishijima, and Z. Miyamoto, Chemistry Letters, 33 (2004) 750

[14] H. Irie, Y. Watanabe, and K. Hashimoto, Chemistry Letters, 32 (2003) 772

[15] S. U. M. Khan, M. Al-Shahry, W. B. Ingler, Science, 297 (2002) 2243

[16] T. Umebayashi, T. Yamaki, S. Yamamoto, A. Miyashita, S. Tanaka, T. Sumita, and K. Asai, J. Appl. Phys., 93 (2003) 5156

[17] T. Ohno, T. Mitsui, and M. Matsumura, Chemistry Letters, 32 (2003) 364

[18] T. Ohno, Water Science and Technology, 49 (2004) 159

[19] T. Umebayashi, T. Yamaki, H. Itoh, and K. Asai, Applied Physics Letters, 81 (2002) 454

[20] C. Burda, Y. Lou, X. Chen, A. C. S. Samia, J. Stout, and L. Gole, NanoLetters, 3 (2003) 1049

[21] O. Diwald, T. L. Thompson, T. Zubkov, E. Goralski, S. D. Walck, J. T. Yates, Jr., J. Phys. Chem. B, 108 (2004) 6004

[22] X. Chen, Y. Lou, A. C. S. Samia, C. Burda, and J. L. Gole, Advanced Functional Materials, 15 (2005) 41

[23] S. Sakthivel, M. Janczarek, and H. Kisch, J. Phys. Chem. B, 108 (2004) 19384

[24] R. Asahi, T. Morikawa, K. Aoki, Y. Taga, Science, 293 (2001) 269

[25] C. D. Valentin, G. Pacchioni, A. Selloni, Phys. Rev. B, 70 (2004) 085116

[26] R. Nakamura, T. Tanaka, Y. Nakato, J. Phys. Chem. B, 108 (2004) 10617

[27] J. A. Rodriguez, T. Lindgren, J. Lu, C. G. Granquist, S. E. Lindquist, J. Phys. Chem. B, 104 (2004) 319

[28] A. Hattori, M. Yamamoto, H. Tada, S. Ito, Chemistry Letters, 8 (1998) 707

[29] J. Yu, W. Ho, Z. Jiang, L. Zhang, Chem. Mater., 14 (2002) 3808

[30] D. Li, H. Haneda, N. K. Labhsetwar, S. Hishita, N. Ohashi, Chemical Physics Letters, 401 (2005) 579

[31] W. Zhao, W. ma, C. Chen, J. Zhao, Z. Shuai, J. Am. Chem. Soc., 126 (2004) 4782

[32] H. Wei, Y. Wu, N. Lun, F. Zhao, J. Mater. Sci., 39 (2004) 1305

[33] Z. Zhang, C. Wang, R. Zakaria, J. Ying, J. Phys. Chem. B, 102 (1998) 10871

[34] N. Serpone, D. Lawless, R. Khairutdinov, J. Phys. Chem., 99 (1995) 16655

[35] R. W. Matthews, Journal of Catalysis, 113 (1988) 549

[36] T. Umebayashi, T. Yamaki, H. Itoh, K. Asai, J. Phys. Chem. Solids, 63 (2002) 1909

CHAPTER 6 C- and V-doped TiO_2 photocatalyst

6.1 Introduction

This chapter will focus on preparing and characterizing C- and V-doped TiO_2 catalyst. Acetaldehyde will be used as a probe molecule in the photocatalytic experiments. In particular, descriptions are provided:

1. To prepare C-doped and C-, V-codoped TiO_2 catalyst.
2. To characterize the catalysts.
3. For the activity test and mechanistic study.

6.2 Preparation of catalysts

C- and V-codoped TiO_2 was prepared using the following procedure: titanium isopropoxide (97%, Aldrich), vanadyl acetylacetonate (98%, Aldrich), urea (99.0-100.5%, Aldrich), and thiourea (99% Aldrich) were used as raw materials. 3.8 g (0.05 mole) thiourea and 3.0 g (0.05 mole) urea were dissolved in 75 mL deionized water. While under vigorous stirring in an ice bath, the desired amount of vanadyl acetylacetonate (corresponding to 0.5, 1, 2, and 3% of vanadium) was added to the solution. Then 11 mL (0.0375 mole) titanium isopropoxide was added drop-wise. The mixture was stirred for 24 h and aged for 48 h. The water was removed by drying in air at 80 °C. The dried powder was crushed and calcined at 500 °C for 2 h in air. The preparation of C-doped TiO_2 used the same procedure without the vanadium precursor. For pure TiO_2, urea, thiourea, and vanadyl acetylacetonate were not used. Commercial

Degussa P25 TiO_2 (anatase/rutile = 75/25) with a specific surface area of 50 m^2/g and primary particle size of 20 nm was selected for comparison purposes.

6.3 Characterization

X-Ray powder diffraction (XRD) patterns were obtained with a Bruker D8 diffractometer, using Cu Kα radiation (1.5406Å) at 40 kV and 40 mA and a secondary graphite monochromator. Samples were packed into a plastic holder. Measurements were recorded in step of 0.025° with a count time of 4 s in the 2θ range of 20-65°. Identification of the phases was made with the help of the Joint Committee on Powder Diffraction Standards (JCPDS) files.

X-ray photoelectron spectroscopy (XPS) data were recorded using a Perkin-Elmer PHI 5400 electron spectrometer. The spectrometer utilizes acrochromatic Al Kα radiation (1486.6 eV) and employs Ar+ sputtering to remove the surface layer of the sample. All spectra were obtained under vacuum at a pressure of about 2.0×10^{-9} Torr. The XPS binding energies were measured with a precision of 0.1 eV. The analyzer pass energy was set to 17.9 eV and the contact time was 50 ms. Before the samples were tested, the spectrometer was calibrated by setting the binding energies of Au $4f_{7/2}$ and Cu $2p_{3/2}$ to 84.0 and 932.7 eV, respectively. Binding energies for the samples were normalized with respect to the position of the C 1s peak resulting from adsorbed hydrocarbon fragments.

Diffuse reflectance spectra (DRS) were recorded with a Cary 500 Scan UV-vis NIR spectrophotometer with an integrating sphere attachment for their diffuse reflectance in the range of 200-800 nm. All spectra were referenced to polytetrafluoroethylene.

N_2 adsorption-desorption isotherms were obtained at -196°C on a NOVA 1000 series instrument (Quantachrome, USA). The specific surface areas were calculated according to the multi-point Brunauer-Emmet-Teller (BET) method. Before adsorption, all the samples were degassed for 1 h at 150°C under vacuum.

6.4 Degradation of acetaldehyde

Acetaldehyde, a good model of typical indoor air pollutant formaldehyde, was chosen as a probe molecule for testing the catalyst activity. Experiments were performed in a cylindrical air filled static reactor (305 mL total volume). The reactor is made of glass and had a quartz window. The light source was a 1000 W high pressure Hg arc lamp (Oriel Corporation). The combination of a vis-NIR long pass filter (400 nm) and colored glass filter (>420 nm) was used to eliminate ultraviolet radiation during visible light experiments. The catalyst (100 mg) was placed in a circular glass dish and then mounted in the reactor. Then, 100 µL of liquid acetaldehyde was introduced into the reactor, which rapidly vaporized. The gaseous mixture of acetaldehyde and air inside the reactor was magnetically stirred constantly. Prior to analysis, the catalyst and acetaldehyde were kept in the reactor for about 30 min to obtain a uniform gas phase concentration. The reactor was cooled by water circulation and experiments are performed at 25 °C. Gaseous samples (35 µL) were periodically (every 10 min) extracted from the reactor and analyzed by GCMS (gas chromatograph equipped with a mass selective detector GCMS-QP5000 from Shimadzu). The temperatures of the column, injector, and detector were maintained at 40, 200, and 280°C respectively.

6.5 Results and discussion

6.5.1 Catalyst activities

The evolution of CO_2 during acetaldehyde degradation was used to estimate the activity of the catalysts. Before shining the light, the activity was measured for 40 min in the dark. Figure 6.1 shows the CO_2 evolution on different catalysts. The photocatalytic activity of doped TiO_2 was greatly enhanced by incorporating it with carbon and vanadium. Most important, the carbon and vanadium co-doped TiO_2 had high activity in the dark: the higher values at zero time were likely due to reaction in the dark occurring during the 30 min period before sampling. In order to enable quantitative comparison, the initial rates for the initial 40 min (with or without irradiation) were calculated to represent the activities. These values are shown in Table 6-1. In the dark, P25 TiO_2 and C-doped TiO_2 showed no activity. However, with the addition of vanadium, the co-doped TiO_2 catalysts were highly active for the degradation of acetaldehyde, especially when the vanadium loading was 2%. Under visible irradiation, the photo catalytic reactivity of C-doped TiO_2 was 8.2 times higher than that of P25 TiO_2 and 6.6 times higher for co-doped TiO_2 for a 2.0% loading (however, a 3.0% loading was less effective). Moreover, for co-doped TiO_2 with 2% vanadium content, the activity was comparable in the dark and under visible irradiation. The different activities among these catalysts likely resulted from different physical properties and reaction mechanisms, as discussed later.

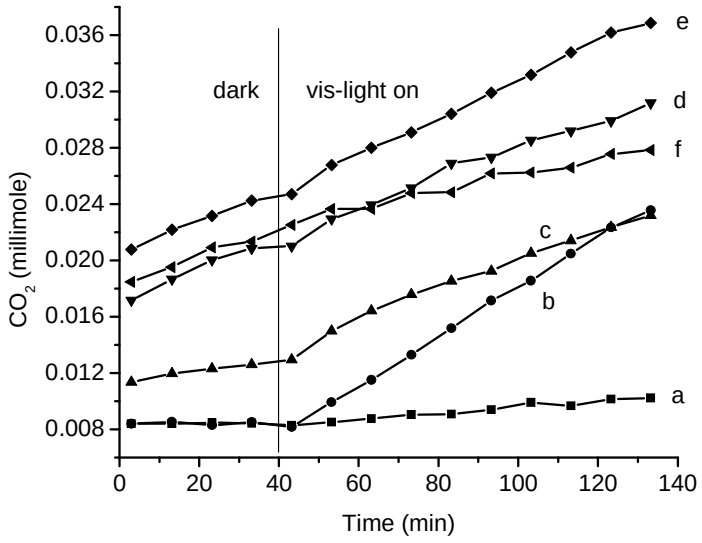

Figure 6.1 CO_2 evolution during CH_3CHO oxidation on P25 TiO_2 and doped TiO_2: (a) P25 TiO_2, (b) C-doped TiO_2, (c) C-, V-doped TiO_2 (0.5%V), (d) C-, V-doped TiO_2 (1.0%V), (e) C-, V-doped TiO_2 (2% V), (f) C-, V-doped TiO_2 (3.0%V)

Table 6-1 Initial rate of CO_2 evolution (mmol/min)

Catalyst	In the dark	Under visible irradiation
P25 TiO_2	0	2.13×10^{-5}
C-doped TiO_2	0	1.74×10^{-4}
C-, V-doped TiO_2 (0.5% V)	3.81×10^{-5}	1.38×10^{-4}
C-, V-doped TiO_2 (1.0% V)	9.85×10^{-5}	1.40×10^{-4}
C-, V-doped TiO_2 (2.0% V)	1.26×10^{-4}	1.37×10^{-4}
C-, V-doped TiO_2 (3.0% V)	6.9×10^{-5}	5.75×10^{-5}

6.5.2 X-ray diffraction

Figure 6.2 shows the XRD patterns of pure TiO_2 and doped TiO_2. TiO_2 anatase diffraction lines can be seen in all XRD patterns. No other crystal phase (rutile or brookite) can be detected. The strongest peak at $2\theta = 25.3°$ is representative of (101) anatase phase reflections. The inset of Figure 6.2 is an enlargement of the (101) plane of all these samples. Compared with pure TiO_2, the peak position of the (101) plane of C-doped TiO_2 shifted slightly to higher 2θ value and the peak was broader, which suggested the distortion of the crystal lattice of doped TiO_2 by the incorporation of elemental carbon and the smaller particle size of C-doped TiO_2. Greater distortion of the structures were observed with the addition of vanadium, indicating vanadium (V^{4+}) was incorporated into the lattice and substituted for Ti^{4+} as suggested by the XPS spectra (see later discussion). From the full width at half maximum (FWHM) of the diffraction pattern, the particle sizes were calculated using Scherrer's equation. Pure TiO_2 had the particle size of 14 nm, while doped TiO_2 had a particle size of 9 nm (Table 6-2). No diffraction lines due to TiC, TiN, and TiS were found, consistent with the XPS results discussed later. Furthermore, no separate VO_x phases were observed even for all vanadium-containing samples possibly due to the high dispersion or the very small crystallite size of vanadia species that may be present.

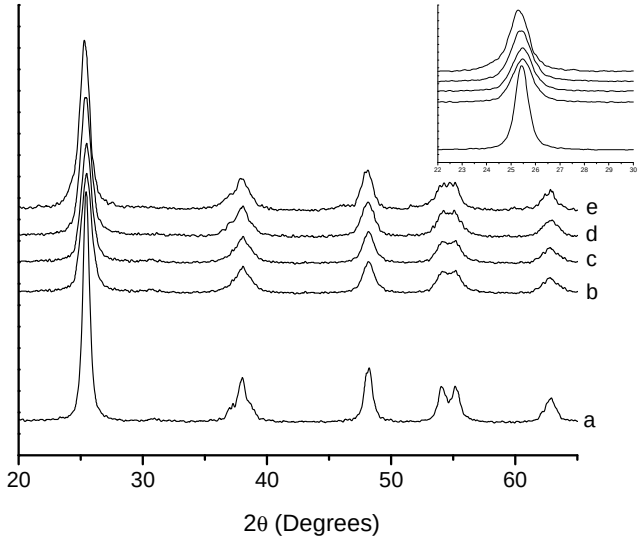

Figure 6.2 X-Ray diffraction patterns of un-doped and doped TiO_2: (a) un-doped TiO_2, (b) co-doped TiO_2, (c) C-doped TiO_2 (0.5 % V), (d) co-doped TiO_2 (2.0 % V), (e) co-doped TiO_2 (3.0 % V)

Table 6-2 Surface areas and particle sizes of samples

Sample	Surface area[a] (m^2/g)	Particle size[b] (nm)
TiO_2	57	14.0
C-doped TiO_2	98	8.9
C-, V-doped TiO_2 (0.5% V)	96	8.9
C-, V-doped TiO_2 (1.0% V)	94	9.0
C-, V-doped TiO_2 (2.0% V)	94	9.2
C-, V-doped TiO_2 (3.0% V)	59	10.3

[a] by BET; [b] by XRD

6.5.3 Raman spectroscopy

Raman spectroscopy was applied to probe the phase formation of TiO_2. It was reported that six modes A_{1g} (519 cm^{-1}), B_{1g} (399 and 519 cm^{-1}), and E_g (144, 197, and 639 cm^{-1}) were Raman-active of anatase phase. Four modes A_{1g} (612 cm^{-1}), B_{1g} (143cm^{-1}), B_{2g} (826 cm^{-1}), and E_g (447cm^{-1}) were Raman-active of rutile.[1,2,3] Four peaks at 148, 399, 519, and 638 cm^{-1} were observed for two samples in Figure 6.3, suggesting that anatase was the predominant phase structure. Measuring the Raman band shape (peak position and linewidth) of the main feature at 144 cm^{-1}, it is possible to determine the crystal dimensions since the particle size can cause large shifts in the location of the scattered Raman peaks and their widths, namely, the quantum size confinement effect.[4,5] The peak at 148 cm^{-1} of C-doped TiO_2 had greater intensity and broader width, indicating enhanced crystallinity and smaller particle size, which was consistent with the results of the XRD measurement.

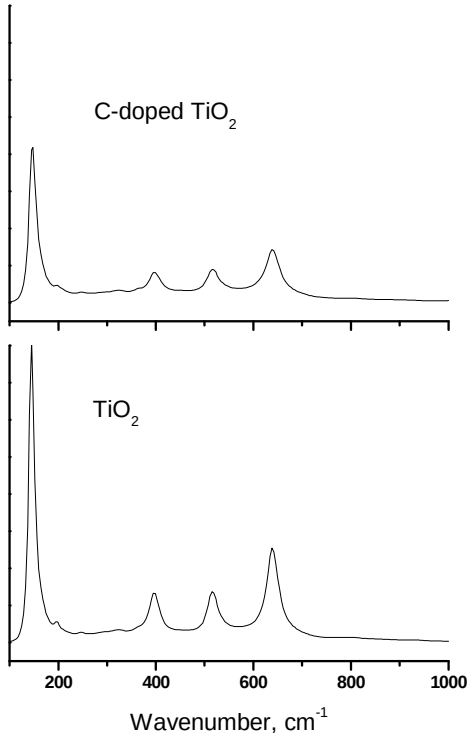

Figure 6.3 Raman spectra of C-doped TiO_2 and pure TiO_2

6.5.4 X-ray photoelectron specstroscopy (XPS)

To investigate the chemical states of the possible dopants incorporated into TiO_2, Ti 2p, C 1s, S 2p3/2, N 1s, and V 2p3/2 binding energies were studied by measuring the XPS spectra. The results are shown in Figure 6.4.

Two peaks for Ti 2p XPS spectrum were observed at 464.2 and 458.5 eV, assigned to Ti 2p(1/2) and 2p(3/2), respectively. These values agree well with published XPS data and are known to be due to Ti^{4+} in pure anatase titania form.[6]

The C 1s XPS spectrum shows one peak at 284.8 eV and a shoulder at around 288.6 eV. The feature at 284.8 eV can be assigned to elemental carbon and the shoulder at around

288.6 eV suggests the existence of carbonate species.[13,7] After sputtering, the shoulder at around 288.6 eV disappeared, indicating carbonate species existed only on the surface. The peak at 284.8 eV still remained and the intensity decreased only slightly. These results strongly imply that elemental carbon deposits not only on the surface but also in the bulk of the TiO_2 powder. A peak at around 281 eV, which was reported to result from the Ti-C bond[14], was not observed for our sample.

The S 2p3/2 XPS spectrum showed a peak at around 168.3 eV. A broad peak attributed to S 2p3/2 at around 168 eV was reported to consist of several oxidation states of S atoms: the peak of the S^{6+} state appeared at 168.2 eV by studying the XPS spectra of pure TiO_2 immersed in H_2SO_4 aqueous solution followed by calcinations at 500 ˚C for 3 h and the peak at 167.5 eV was assigned to S^{4+}.[16,18] Sayago et al.[8] reported that the peak of the S 2p state was in the region of 166-170 eV for adsorbed SO_2 molecules on a TiO_2 surface. Since our samples were calcined in air at 500 ˚C, the S 2p3/2 peak can be attributed to the S^{6+} state. The S 2p peak between 160-163 eV, coming from S atoms substituting for O atoms on the TiO_2 surface[9], was not observed in our case. The disappearance of the S 2p3/2 peak after sputtering indicates that sulfur species appeared only on the surface. The formation of carbonate (1448 cm^{-1}) and sulfate species (1100 cm^{-1}) is supported by the FTIR spectra showing their characteristic band structures (not presented here).

The N 1s XPS spectrum showed a peak at around 399 eV. The value is consistent with XPS data from chemisorbed N_2 molecules[10] or molecularly adsorbed N-containing compounds (NOx and NH_3, which formed during the decomposition and oxidation of the

N-precursors).[11] The feature at around 396 eV, generally assigned to N^{2-} anions resulting from substitution for oxygen sites by nitrogen atoms in the TiO_2 lattice[7,10 ,12], was not observed. Based on our preparation process, the peak at around 399 eV can be assigned to adsorbed NO_x or NH_3. Clearly, however, these nitrogen species existed only on the surface of TiO_2 because of the disappearance of the peak after sputtering.

The O 1s satellite interfered with the V 2p3/2 XPS peak. The magnitude of the V 2p3/2 peak was small and the peak appeared as two shoulders. The shoulder at a binding energy of 516.9 eV suggests V^{5+} species, while the shoulder at 516.3 eV can be assigned to V^{4+}. These values are consistent with binding energy of V 2p3/2 measured for V_2O_5/TiO_2 catalyst.[13,14] V^{4+} ions were incorporated into the crystal lattice of TiO_2 and no vanadium-titanium phase was present from the previous XRD discussion, thus, V^{4+} ions substituted for Ti^{4+} ions and formed Ti-O-V bond. Obviously, some V^{4+} ions were oxidized into V^{5+} in the preparation process since vanadium existed only as V^{4+} in the precursor; the formation of V^{5+} possibly occurred during the annealing.

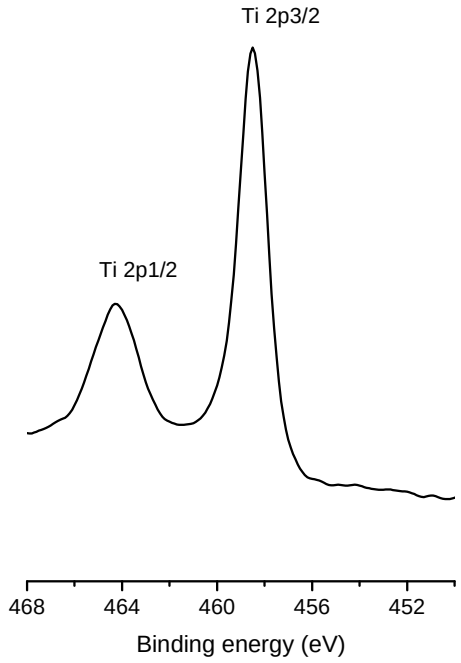
Ti 2p3/2
Ti 2p1/2
468
464
460
456
452
Binding energy (eV)

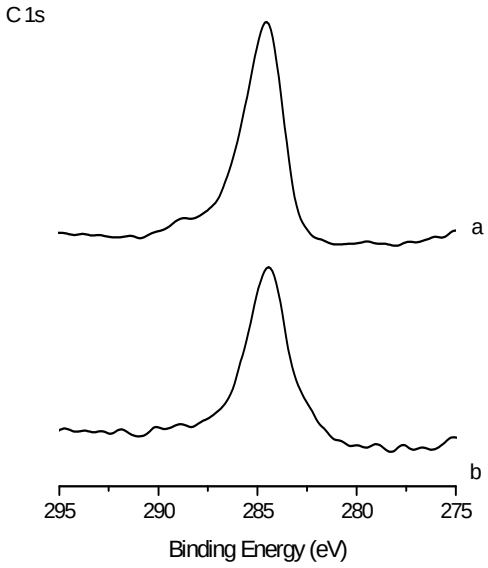
C 1s
a
b
295
290
285
280
275
Binding Energy (eV)

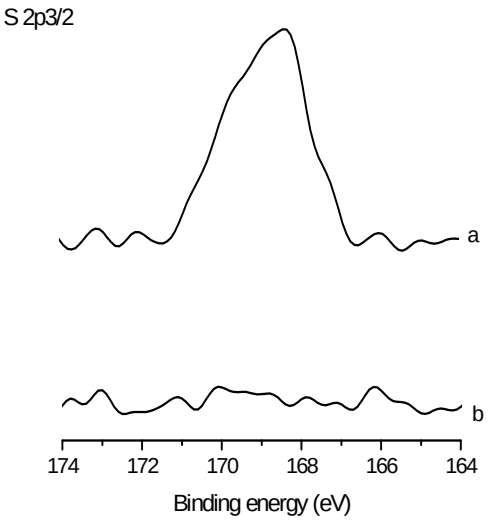
S 2p3/2
a
b
174
172
170
168
166
164
Binding energy (eV)

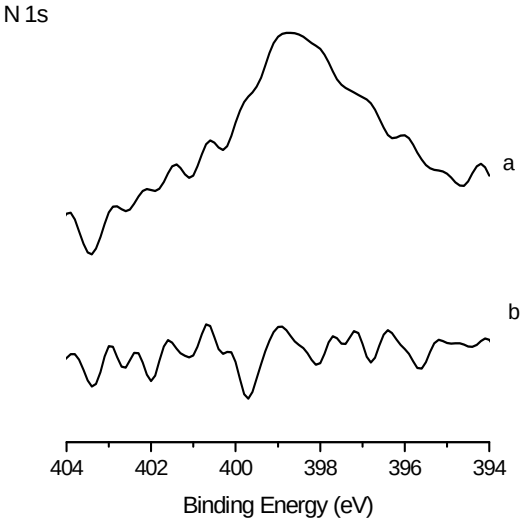
N 1s
a
b
404
402
400
398
396
394
Binding Energy (eV)

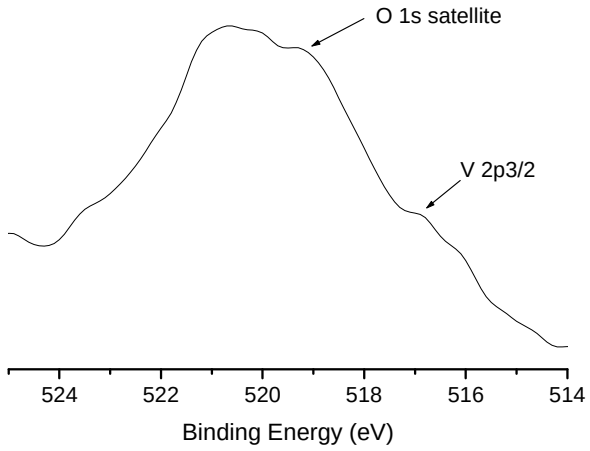

Figure 6.4 XPS spectra of C-doped TiO_2: Ti 2p, C 1s, S 2p3/2, N 1s (a: before sputtering; b: after sputtering) and C-, V-doped TiO_2 (2.0% V): V 2p3/2

6.5.5 UV-vis reflectance spectroscopy

Figure 6.5 shows the UV-Vis absorption spectra of the un-doped and doped TiO_2. Commercial Degussa P-25 TiO_2 has absorption only in the UV region. The onset absorption spectrum of pure TiO_2 shows a very weak red shift. On the other hand, photoabsorption in the visible region of the doped TiO_2 is very large. C-doped TiO_2 absorbs the photo energy in the visible region up to 600 nm, indicating that the incorporated elemental carbon was acting as a photosensitizer.[15] With the addition of vanadium, the absorption curve of the co-doped TiO_2 extended to 800 nm. It has been reported that V^{5+} shows absorption at < 570 nm and that V^{4+} has an absorption band centered at 770 nm,[16] therefore the spectra suggest the co-existence of V^{5+} and V^{4+}, consistent with XPS spectra. The tailing of absorption band can be assigned to the charge-transfer transition from the d orbital of V^{4+} to the conduction band of TiO_2.[10] In the presence of visible light, it appears that this photoexcited electron enabled chemical

reactions to occur at the surface of V-doped TiO_2 because the oxidation of V^{4+} to V^{5+} occurred 2.1 eV below the TiO_2 conduction band.[17] The extended visible absorption obviously suggests modified electronic properties by incorporation of vanadium, forming impurity energy levels between the valence band and conduction band of TiO_2.[4]

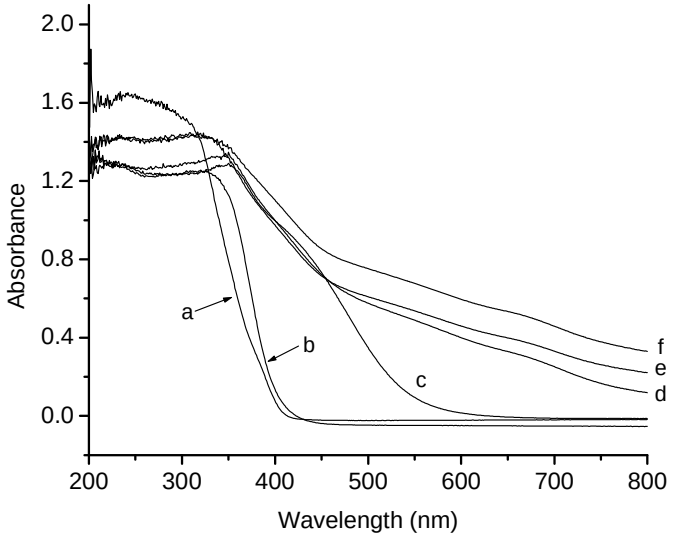

Figure 6.5 Diffuse reflectance spectra of P25 TiO_2, un-doped and doped TiO_2: (a) P25, (b) TiO_2, (c) C-doped TiO_2, (d) C-, V-doped TiO_2 (0.5 % V), (e) C-, V-doped TiO_2 (2.0 % V), (f) C-, V-doped TiO_2 (3.0 % V)

6.6 Mechanistic studies

Figure 6.1 illustrates that P25 TiO_2 and C-doped TiO_2 were inactive in the dark for the degradation of acetaldehyde. With the introduction of vanadium, modified TiO_2 showed high activity in the dark. XRD spectra indicated no new vanadium-titanium compound was present; thus the increase in the activity must be due to a change in the surface of the catalyst resulting from vanadium substitution. Based on the characterization results, the following explanation for the high activity in the dark can be considered. During the

preparation of catalysts, V^{4+} ions are incorporated into the bulk and on the surface of TiO_2 in the gelation stage. It is possible that V^{4+} in the sublayers of TiO_2 is oxidized to V^{5+} during water-removal and/or calcination in air. As shown in Figure 6.6, if pentavalent V^{5+} ions are present at tetravalent sites (Ti^{4+} or V^{4+}), the substitution could induce a free electron.[18] V^{5+} ion only shares four valence electrons with four O^{2-} neighbor ions. The fifth electron cannot be shared and is delocalized around the V^{5+} positive center. Only a small amount of thermal energy is needed to delocalize this electron and promote it into the conduction band.[18] In the dark, the promoted electron can be transferred to triplet oxygen to generate the superoxide radical anion $O_2^{\bullet -}$, which is known to degrade organic compounds.[15,19] When the loading of vanadium increases from 0.5 to 2.0%, more V^{4+} ions in the sublayer of TiO_2 are possibly oxidized into V^{5+}, enhancing the activity. However, further increasing the vanadium content could deteriorate the dispersion and lead to the aggregation of vanadium, as indicated by the smaller surface area. That is why, as shown in Figure 6.1, the activity decreased when the vanadium loading increased from 2.0 to 3.0%.

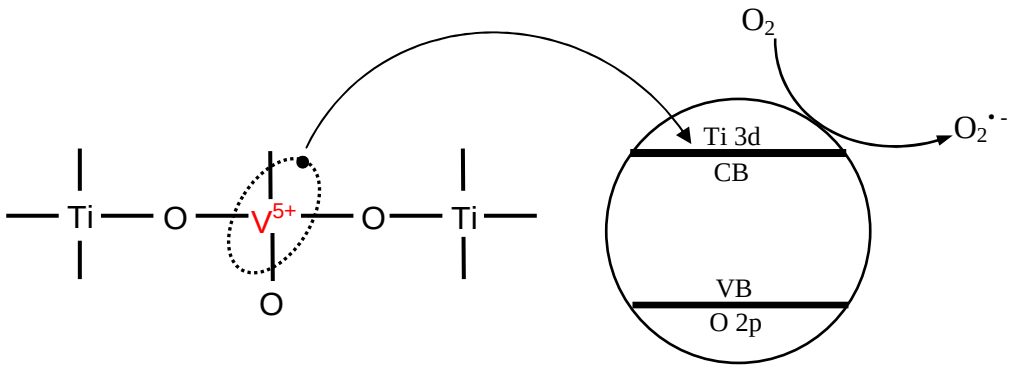

Figure 6.6 Proposed electron transfer pathway to produce superoxide radical anion, $O_2^{\bullet -}$, when V^{5+} was present at tetravalent site

Under visible light irradiation, two major reaction pathways can be considered.

(1) The elemental carbon acts as a photosensitiser. As shown in Figure 6.7, in the presence of visible light, the excited photosensitiser injects an electron into the conduction band of titanium dioxide. Subsequently, the electron is transferred to oxygen adsorbed on the TiO_2 surface producing $O_2^{\bullet -}$, which is capable of degrading organic compounds.[15] After a series of reactions, acetaldehyde molecules are finally degraded into CO_2 and H_2O.

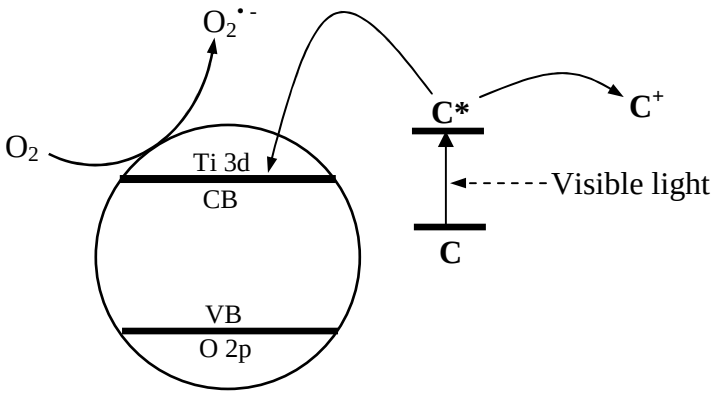

Figure 6.7 Proposed electron transfer pathway to produce superoxide radical anion, $O_2^{\bullet -}$, on C-doped TiO_2 particles under visible light irradiation (C refers to elemental carbon).

(2) The incorporation of vanadium into the crystal lattice of TiO_2 modifies the electronic properties of TiO_2. Because the oxidation V^{4+} to V^{5+} occurs 2.1 eV below the TiO_2 conduction band, a 3d electron from a V^{4+} center is easily photoexcited into the TiO_2 conduction band under visible light irradiation[17], generating $O_2^{\bullet -}$ similarly as mentioned in parthway 1. It is assumed that this photoexcited electron initiates chemical reactions.

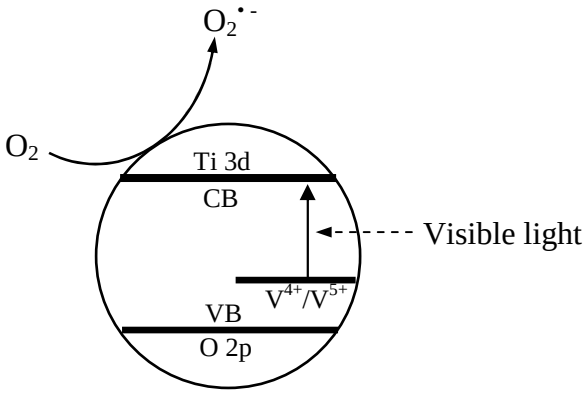

Figure 6.8 Proposed electron transfer pathway to produce superoxide radical anion, $O_2^{\bullet -}$, when impurity level was introduced between the valence and conduction band of TiO_2.

For C-doped TiO_2, pathway 1 is involved in the photoreaction. Both pathways are included for C-, V- co-doped TiO_2. In contrast to the transition metal loading level in the range of 0.1-0.5% for the purpose of enhancement of TiO_2 photo reactivitivity[10], the content of vanadium in our samples is much higher. As shown in Table 6-2, the effective samples have much higher surface areas. Therefore, in addition to the function as a photosensitizer, the doped elemental carbon also increases the surface area, which significantly increases the dispersion of vanadium and possibly provides more possibly accessible active sites, enhancing activity. Additionally, high surface areas are beneficial for the sorption of acetaldehyde on the surface of catalysts. The decrease of activity for the co-doped TiO_2 when the vanadium loading increases from 2% to 3% is possibly the result of poor dispersion reduced surface area, and aggregation of vanadium, such as V_2O_5. Pure V_2O_5 and TiO_2-supported V_2O_5 then failed to enter the structure of the solid solution did not show any photocatalytic activity.[20]

6.7 Conclusions

C-doped and C-, V-doped TiO_2 catalysts were successfully synthesized by a sol-gel process. The C-doped TiO_2 showed high activity for the degradation of acetaldehyde under visible irradiation. The doped elemental carbon acted as photosensitizer and increased the surface area, resulting in the high dispersion of vanadium for the co-doped TiO_2 catalysts, which had high activity both in the dark and under visible light irradiation. The insertion of pentavalent V^{5+} into tetravalent sites induced a free electron that could be delocalized and promoted into the conduction band of TiO_2 by small thermal energy. The superoxide radical anion $O_2^{\bullet-}$, produced when the free electron was transferred to adsorbed O_2, was responsible for the degradation of acetaldehyde. We report here for the first time that the activities were comparable in the dark and under visible light irradiation for the co-doped TiO_2, especially with a vanadium content of 2.0%. Under visible light irradiation, the incorporation of vanadium introduced impurity levels between the valence and conduction band of TiO_2 so that electrons could be easily photoexcited into the conduction band, initiating the chemical reaction.

References

[1] H. Berger, H. Tang, F. Kevy, J. Cryt. Growth, 130 (1993) 108

[2] S. P. S. Porto, P. A. Fbeury, T. C. Damen, Phys. Rev., 154 (1967) 522

[3] S. C. Pillai, P. Periyat, R. George, D. E. McCormack, M. K. Seery, H. Hayden, J. Colreavy, D. Corr, S. J. Hinder, J. Phys. Chem. C, 111 (2007) 1605

[4] Y. Cong, J. Zhang, F. Chen, M. Anpo, J. Phys. Chem. C, 111 (2007) 6976

[5] D. Bersani, P. P. Lottici, X. Ding, Appl. Phys. Lett., 72 (1998) 73

[6] S. Joung, T. Amemiya, M. Murabayashi, K. Itoh, Chem. Eur. J., 12 (2006) 5526

[7] S. Sakthivel, H. Kisch, Angew. Chem. Int. Ed., 42 (2003) 4908

[8] D. I. Sayago, P. Serrano, O. Bohme, A. Goldoni, G. Paolucci, E. Roman, J. A. Martin-Gago, Phys. Rev. B, 64 (2001) 205402

[9] E. L. D. Hebenstreit, W. Hebenstreit, U. Diebold, Surf. Sci., 470 (2001) 347

[10] N. C. Saha, H. G. Tompkins, J. Appl. Phys., 72 (1992) 3072

[11] D. Li, N. Ohashi, S. Hishita, T. Kolodiazhnyi, H. Handea, J. Solid State Chem., 178 (2005) 3293

[12] H. Irie, Y. Watanabe, K. Hashimoto, J. Phys. Chem. B, 107 (2003) 5483

[13] M. Kobayashi, R. Kuma, S. Masaki, N. Sugishima, Appl. Catal. B: Environmental, 60 (2005) 173

[14] S. L. T. Anderson, Catal. Lett., 7 (1990) 351

[15] C. Lettmann, K. Hildenbrand, H. Kisch, W. Macyk, W. Maier, Appl. Catal. B: Environmental, 32 (2001) 215

[16] H. Ozaki, S. Iwamoto, M. Inoue, catal. Lett., 113 (2007) 95

[17] K. Mizushima, M. Tanaka, A. Asai, S. Iida, J. B. Goodenough, J. Phys. Chem. Solids, 40 (1979) 1129

[18] J. M. Herrmann, J. Disdier, G. Deo, I. E. Wachs, J. Chem. Soc. Faraday Trans., 93 (1997) 1655

[19] M. M. Mohamed, M. M. Al-Esaimi, J. Mol. Catal. A: Chem., 255 (2006) 53

[20] J. C. Yu, J. Lin, R. W. M. Kwork, J. Photochem. Photobiol. A: Chem., 111 (1997) 199

CHAPTER 7 C and N co-doped TiO_2 photocatalyst

7.1 Introduction

In Chapter 6, we synthesized highly visible-light-active C- and V-co-doped TiO_2 catalysts, which also showed comparable high activity in the dark for the degradation of acetaldehyde. The synergetic effects of doped C and V on the optical shift, surface area, crystallinity, and activity of TiO_2 were studied. The possible disadvantage of doping with transition metal ions is that these doped ions can also act as recombination centers for electrons and holes, thus decreasing the photocatalytic efficiency. Also, thermal stability of these transition metal ion doped materials should be considered. So this chapter will focus on preparing and characterizing C and N co-doped TiO_2 catalyst. The activity of the catalyst will be tested by degrading methylene blue (MB), which is known to be difficult to degrade under visible light and is often used as a model dye contaminant to evaluate the activity of a photocatalyst. In particular, descriptions are provided:

1. To prepare C and N co-doped TiO_2 catalyst.
2. To characterize the catalysts.
3. To degrade Methylene Blue.

7.2 Preparation of the catalyst

30 milliliters of deionized water was put in a water-ice bath. While under vigorous stirring, 8 milliliters of titanium isopropoxide (97%, Aldrich) was added drop-wise. The mixture was stirred for 12 h and aged for 24 h. The water was removed by drying in air at 80 °C. The as-obtained sample was thoroughly ground with an agate mortar pestle and

calcined under NH_3 flow at 500 °C for 2 h, then treated in air at 200 °C for 1 h. The sample was denoted as CN-TiO_2. Pure TiO_2 was prepared by treating the as-obtained sample in air at 500 °C for 2 h.

7.3 Catalyst characterization

N_2 adsorption-desorption isotherms were obtained at -196°C on a NOVA 1000 series instrument (Quantachrome, USA). The specific surface areas were calculated according to the multi-point Brunauer-Emmet-Teller (BET) method. The pore size distributions were calculated from the desorption curve. The Barett-Joyner-Halenda (BJH) method was used to determine the pore volume and pore size. Before adsorption, samples were degassed at 150 °C for 1 h under vacuum.

Raman spectra were recorded using a Nicolet Nexus 670 Fourier transform IR (FT-IR) with a Raman module. The system consisted of a continuous Nd-YAG (yttrium aluminum garnet) laser (1064 nm) and a liquid nitrogen cooled germanium or InGaAs detector in the 4000-100 cm^{-1} range. The laser power used was in the range of 0.2-0.6 W with a data point spacing of 3.5 cm^{-1}. The sample was placed in a glass cylindrical Raman cuvette (Nicolet) and a typical spectrum contained 128 scans.

X-ray photoelectron spectroscopy (XPS) data were recorded using a Perkin-Elmer PHI 5400 electron spectrometer. The spectrometer utilized acrochromatic Al *Kα* radiation (1486.6 eV). All spectra were obtained under vacuum at a pressure of about 2.0×10^{-9} torr. The XPS binding energies were measured with a precision of 0.1 eV. Analyzer pass energy was set to 17.9 eV and the contact time was 50 ms. Before testing the samples, the

spectrometer was calibrated by setting the binding energies of Au $4f_{7/2}$ and Cu $2p_{3/2}$ to 84.0 and 932.7 eV, respectively. Binding energies for the samples were normalized with respect to the position of the C 1*s* peak resulting from adsorbed hydrocarbon fragments.

X-Ray powder diffraction (XRD) patterns were obtained with a Bruker D8 diffractometer, using Cu Kα radiation (1.5406Å) at 40 kV and 40 mA and a secondary graphite monochromator. Samples were packed into a plastic holder. The measurements were recorded in steps of 0.025° with a count time of 2 s in the 2θ range of 20-65°. Identification of the phases was made with the help of the Joint Committee on Powder Diffraction Standards (JCPDS) files.

Diffuse reflectance spectra (DRS) were recorded with a Cary 500 Scan UV-vis NIR spectrophotometer with an integrating sphere attachment for their diffuse reflectance in the range of 200-800 nm. All spectra were referenced to polytetrafluoroethylene.

Photoluminescence (PL) spectra were measured with a fluorospectrophotometer (SPEX Fluoromax-2) by using the 280 nm line of a Xe lamp as the excitation source at room temperature.

7.4 Photocatalytic activity measurement

The photocatalytic activities of CN-TiO_2 and TiO_2 catalysts were evaluated by the degradation of methylene blue (MB) in an aqueous solution. The light source was a 1000 W high pressure Hg arc lamp (Oriel Corporation). The combination of a Vis-NIR long pass filter (400 nm) and colored glass filter (>420 nm) was used to eliminate UV

radiation during visible light experiments. A general procedure was carried out as follows: 100 mL aqueous MB solution (10 mg/L) was contained in a water-jacketed reactor, which was kept at 25 °C. Thirty milligram of catalyst was suspended in the solution. The suspension was kept under vigorous stirring for 60 min in the dark to establish the adsorption-desorption equilibrium of MB. Then, the suspension was irradiated under visible light. Samples were withdrawn every 30 min and centrifuged and analyzed for the degradation of MB using a UV-vis Cary 500 Spectrophotometer. MB has maximum absorbance at 664 nm and that was taken as a way for following the MB degradation. The absorbance was converted to the MB concentration in accordance with a standard curve showing a linear relationship between the concentration and the absorbance at this wavelength. The same procedure was followed for the UV light experiment by using two cut-off filters ($320 < \lambda < 420$ nm).

7.5 Results and discussion

7.5.1 N_2 adsorption-desorption

Figure 7.1 shows the pore size distribution curves and nitrogen isotherms of TiO_2 and CN-TiO_2. Both isotherms are type IV with an H2 hysteresis loop, which is characteristic of a mesoporous structure. The textural properties of both samples are listed in Table 7-1, which shows that the surface area of doped TiO_2 was significantly larger. Also the larger pore size and pore volume and smaller crystallite size possibly provided more accessible active sites and enhanced the activity of the catalyst.

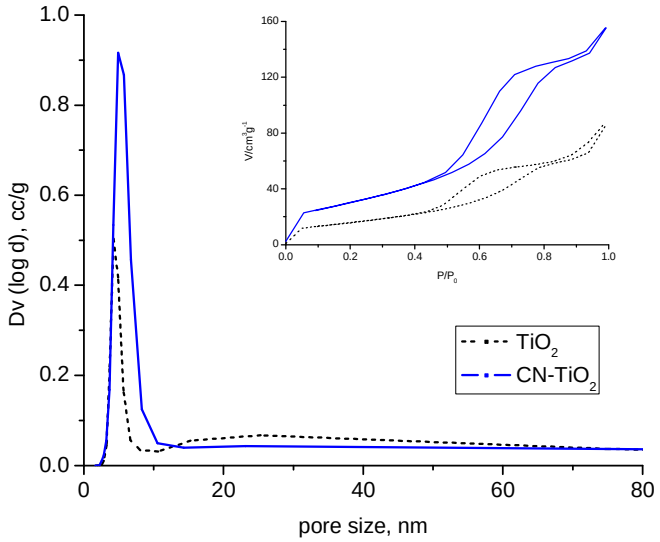

Figure 7.1 Pore size distribution and the corresponding isotherm of TiO_2 and CN-TiO_2

Table 7-1 Textural properties of TiO_2 and CN-TiO_2

Sample	S_{BET} (m^2/g)	Pore size (nm)	Pore volume (cm^3/g)
TiO_2	57	4.2	0.14
CN-TiO_2	109	4.9	0.26

7.5.2 FT-Raman

Raman spectroscopy was successfully applied to probe the phase formation of titanium oxide. It has been reported that six modes A_{1g} (519 cm^{-1}), B_{1g} (399 and 519 cm^{-1}), and E_g (144, 197, and 639 cm^{-1}) were Raman-active for the anatase phase, while four modes A_{1g} (612 cm^{-1}), B_{1g} (143cm^{-1}), B_{2g} (826 cm^{-1}), and E_g (447cm^{-1}) were Raman-active for the rutile phase. [1,2,3] Figure 7.2 shows Raman spectra of TiO_2 and CN-TiO_2. Four peaks at 148, 399, 519, and 638 cm^{-1} are present for both samples, suggesting that anatase was the

predominant phase structure. From the the measurement of the Raman band shape (peak position and line width) of the main feature at 144 cm^{-1}, it is possible to determine the crystal dimensions since the particle size can cause large shifts in the location of the scattered Raman peaks and their widths, namely, the quantum size confinement effect.[4,5] It was obvious that the peak at 148 cm^{-1} of CN-TiO_2 had stronger intensity and broader width, indicating enhanced crystallinity and smaller particle size, which was consistent with the results of later XRD measurement. An additional peak also appeared at 320 cm^{-1} in the spectrum of CN-TiO_2 and this feature was attributed to the first-order scattering of a non-stoichiometric titanium nitride.[6] In order to better understand the change in the Raman spectrum, the spectra in the range of 300-700 cm^{-1} were fitted. In the fitting curves, another two peaks at 460 and 570 cm^{-1} were observed for CN-TiO_2. The peak at 460 cm^{-1} was related to second-order acoustic mode of titanium nitride and peak at 570 cm^{-1} was related to transverse optical mode.[7] Consequently, when nitrogen was doped, it replaced oxygen atoms in the titanium oxide crystal lattice.

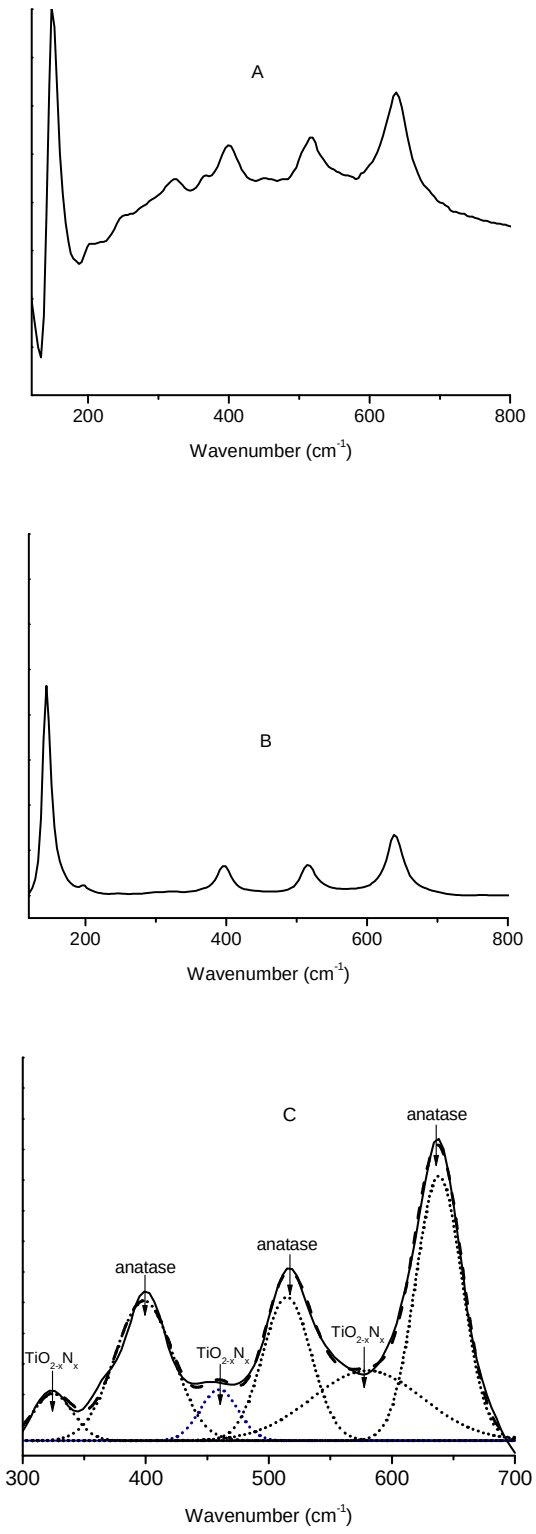

Figure 7.2 Raman spectra of CN-TiO_2 (A) TiO_2 (B), and fitting curves for CN-TiO_2 (C)

7.5.3 X-ray photoelectron spectroscopy (XPS)

XPS measurements were carried out to determine the chemical state of N or C incorporated into the TiO_2 catalysts. Three forms of carbon species have been previously detected: elemental carbon (285 eV) located within the tetrahedral and octahedral interstices existing within the anatase crystal, Ti-C bond resulting from substituting oxygen atoms by carbon (281.5 eV), and the carbonate species adsorbed on the surface (288 eV).[8,9] Figure 7.3 shows the XPS spectra for CN-TiO_2. The C 1s spectrum showed one strong peak at 284.6 eV and a weak shoulder at around 288.5 eV. Therefore, most of the carbon incorporated in the TiO_2 matrix was present as elemental carbon and a small amount of carbonate species was on the surface. A peak at around 281 eV, reportedly resulting from Ti-C bonds, was not observed in the sample, suggesting that carbon did not substitute for oxygen atom in the lattice of TiO_2.

The N 1s spectra showed a peak at 396.2 eV and another at 399.5 eV. It has been reported that a N 1s peak at 400 eV is related to molecular chemisorbed nitrogen or molecularly adsorbed NO_x or NH_3, and a peak at 397.5 eV has been observed in TiN.[10,11,12] However, the assignment of the XPS peak of N 1s is somewhat controversial. Cong et al.[4] attributed the peak at 399.2 eV to anionic N in O-Ti-N linkages. Prokes et al.[13] found that the N 1s peak for the doped TiO_2-based nanocolloid was broad and centered at 401.3 eV. We attribute the peak at 396 eV to the presence of Ti-N bond resulting from substitution for oxygen sites by nitrogen atoms in the TiO_2 lattice, which was consistent with the literature.[14, 15,16] The results also coincided with Raman data in

Figure 7.2. The feature at 399.5 eV was assigned to adsorbed NH_3 based on our preparation method.

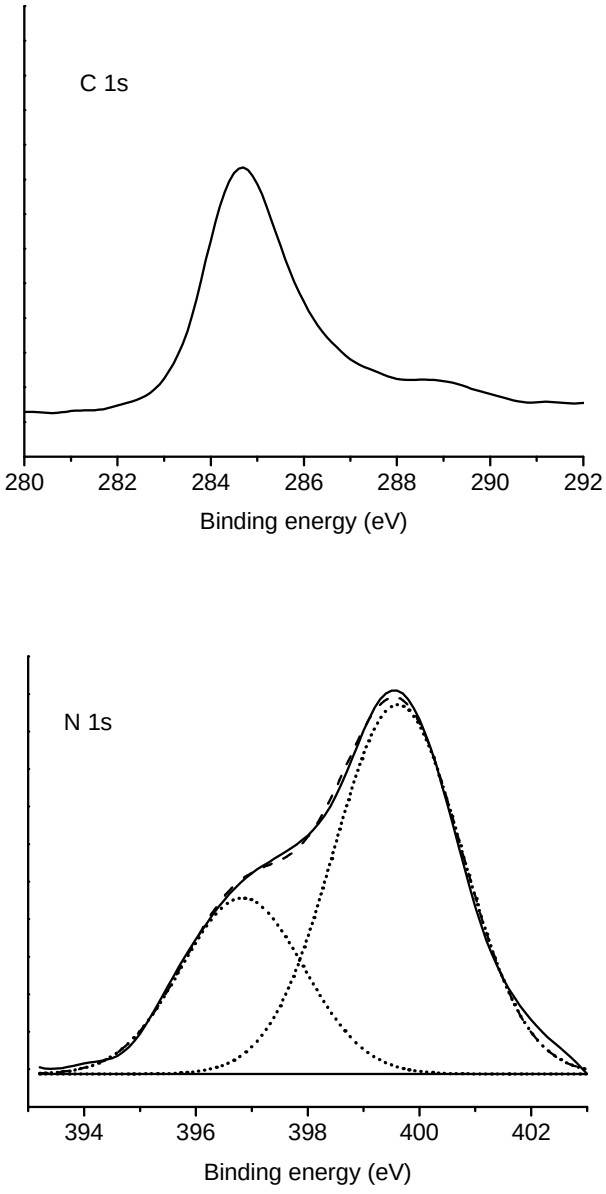

Figure 7.3 XPS spectra for C 1s, N 1s of CN-TiO_2

7.5.4 X-ray diffraction (XRD)

Crystal structures of CN-TiO_2 and pure TiO_2 were determined with XRD. Both samples only showed the anatase phase; no other crystal phase (rutile or brookite) can be detected. The strongest peak at $2\theta = 25.3°$, representative of (101) anatase phase reflections, is shown in Figure 7.4. Compared with pure TiO_2, the peak position shifted slightly toward a higher 2θ value, which suggests that the crystal lattice of TiO_2 was distorted by the carbon or nitrogen dopants, probably most by nitrogen since it substituted for oxygen atoms in the lattice of TiO_2. It can also be seen that doped TiO_2 had broader peak than pure TiO_2, indicating smaller crystallite size of the doped TiO_2. From the full width at half maximum (FWHM) of the diffraction pattern, the crystallite sizes were calculated using Scherrer's equation. Pure TiO_2 was 14 nm and doped TiO_2 had a size of about 9 nm. In addition, no diffraction lines due to TiC or TiN appeared, consistent with the XPS results discussed earlier.

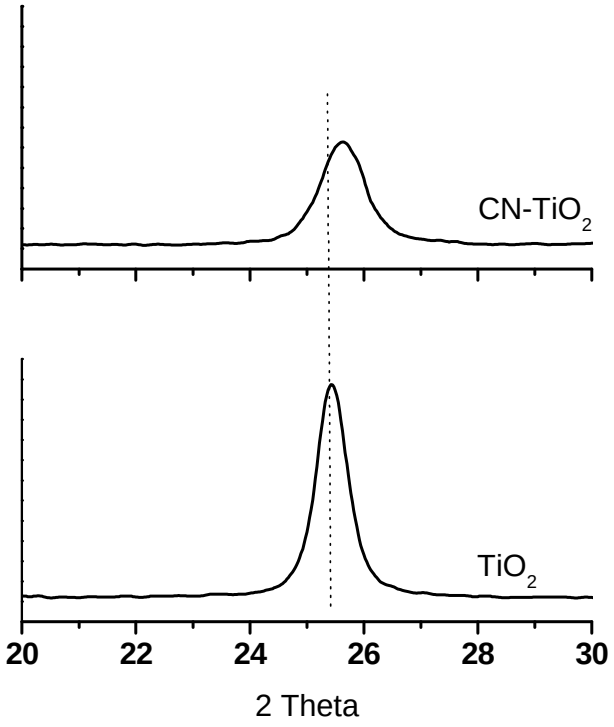

Figure 7.4 XRD patterns of CN-TiO_2 and TiO_2

7.5.5 Diffuse reflectance spectroscopy (DRS)

Figure 7.5 shows the diffuse reflectance spectra of CN-TiO_2 and TiO_2. As expected, pure TiO_2 only exhibited absorption in the UV region. However, the optical response of CN-TiO_2 was extended into the visible light region. The visible light absorption for CN-TiO_2 was associated with doped nitrogen and carbon: carbon can act as a photosensitizer[17], and nitrogen can introduce an impurity level between the valence and conduction band of TiO_2[18] or narrow the band gap by mixing the N 2p and O 2p states.[19] The band gap energies were calculated according to the following equation, $E_g = hc/\lambda$, where E_g is the band gap energy (eV), h is the Planck's constant (4.135667×10^{-15} eV·s), c is the velocity of light (3×10^8 m/s), and λ is the wavelength (nm) of absorption onset. The band gap energies were 3.05 and 2.12 eV for TiO_2 and CN-TiO_2, respectively.

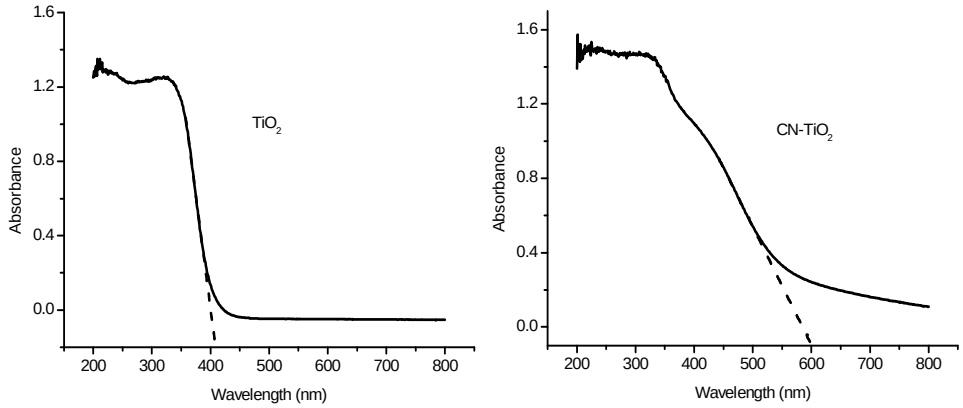

Figure 7.5 Diffuse reflectance spectra of TiO_2 and CN-TiO_2

7.5.6 Photoluminescence (PL)

The PL emission spectra have been widely used to investigate the efficiency of charge carrier trapping, migration, and transfer and to understand the fate of electron-hole pairs in semiconductor particles since PL emission results from the recombination of free carriers.[20,21] Figure 7.6 shows the PL spectra of TiO_2 and CN-TiO_2. The peak at 470-550 nm can be assigned to emission signals originating from the charge transfer transition of an oxygen vacancy trapped electron.[20,21] The PL intensity of pure TiO_2 was significantly stronger than that of CN-TiO_2. Because the PL emission is the result of the recombination of excited electrons and holes, the lower PL intensity indicates a lower recombination rate of these electrons and holes under light irradiation.[20,22,23] Therefore, the dopants (nitrogen or carbon) quenched the luminescence and enhanced the separation of photoexcited electrons and holes. Since the efficiency of photocatalysis is proportional to the charge carrier (e^- or h^+) transfer rate and inversely proportional to the sum of charge

carrier transfer rate and electron-hole recombination rate,[24] CN-TiO_2 should have a higher photonic efficiency than the pure TiO_2.

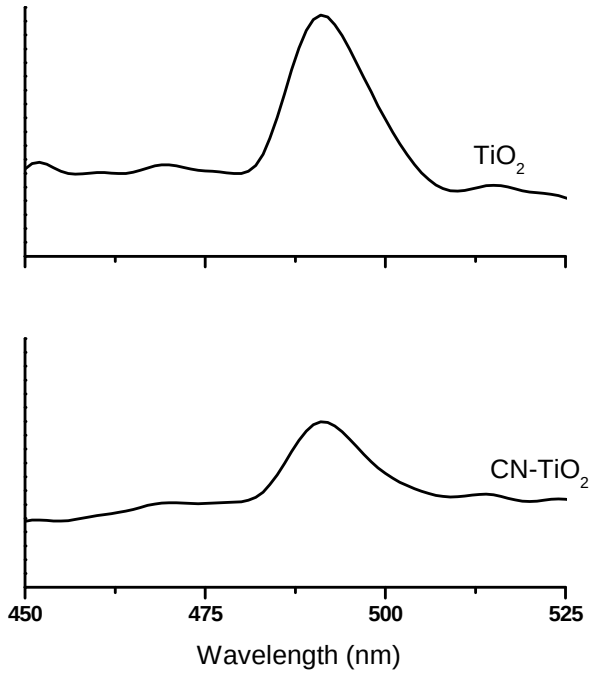

Figure 7.6 Photoluminescence emission spectra for TiO_2 and CN-TiO_2 measured at room temperature (excitation wavelength 280 nm)

7.6 Degradation of methylene blue (MB)

7.6.1 Under visible light irradiation

According to diffuse reflectance UV-vis spectra, the optical response of TiO_2 was shifted slightly from UV to the visible light region due to the introduction of carbon and nitrogen. This implied that CN-TiO_2 might be active under visible light irradiation. Figure 7.7 depicts the results of degradation of MB in the presence of CN-TiO_2 and TiO_2 under visible light irradiation. CN-TiO_2 showed much higher activity in the presence of

visible light than pure TiO_2, which exhibited little activity as expected. Results suggest that doping of C and N was an effective way to shift the optical response from UV to the visible light region and improve the visible-light-induced activity of TiO_2-based catalyst for the degradation of MB. It was assumed that dopants carbon and nitrogen functioned differently for absorption in the visible light region in our case: carbon acted as a photosensitizer, which can be excited and inject electrons into the conduction band of TiO_2. Subsequently, the electrons can be transferred to surface adsorbed oxygen molecules and form superoxide anions, which can further transform to $OH^{\bullet}$ and initiate the degradation of MB. Also, carbon increased the surface area of the TiO_2 catalyst and improved the adsorption of MB. It is well known that organic compounds should be preconcentrated on the surface of the semiconductor particles to effectively utilize the photo-excitation.[25] The substitution of nitrogen for oxygen atoms in the crystal structure of TiO_2 improved the visible light sensitivity by mixing the N 2p and O 2p states or introducing a mid-gap (N 2p) level, which formed slightly above the top of the (O 2p) valence band.

7.6.2 Under UV irradiation

The PL emission spectra indicated that the dopants carbon and nitrogen enhanced the separation of photoexcited electrons and holes. Therefore, more electrons and holes should also available in the degradation of MB for CN-TiO_2 under UV irradiation. Figure 7.8 shows the degradation of MB in the presence of CN-TiO_2 and TiO_2 under UV irradiation. As expected, CN-TiO_2 had higher activity than pure TiO_2.

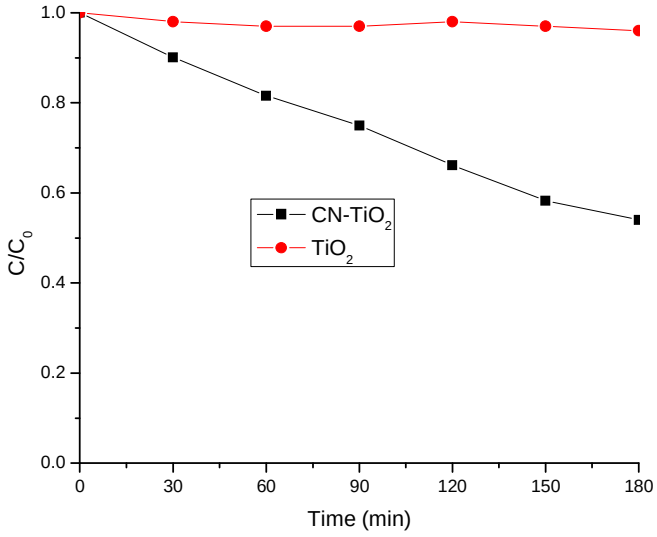

Figure 7.7 Degradation of MB on CN-TiO_2 and TiO_2 under visible light irradiation

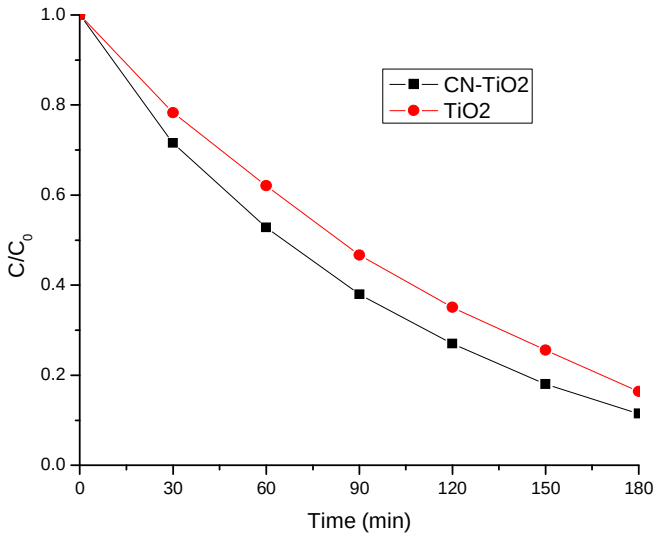

Figure 7.8 Degradation of MB on CN-TiO2 and TiO2 under UV irradiation

7.7 Conclusions

In this study, carbon and nitrogen co-doped TiO_2 catalysts were successfully synthesized by a simple method. Carbon doping resulted in the improvement of visible light absorption and higher surface area of the TiO_2 catalyst. Nitrogen doping narrowed the band gap by mixing the N 2p and O 2p states or introducing a mid-gap (N 2p) level,

which formed slightly above the top of the (O 2p) valence band. Carbon and nitrogen dopants enhanced the separation of photoexcited electrons and holes and improved the photocatalytic efficiency of the TiO_2 catalyst. The co-doped TiO_2 showed higher activity than pure TiO_2 for the degradation of MB under visible light as well as UV irradiation. The high activity was attributed to the several beneficial effects associated with the introduction of carbon and nitrogen.

References

[1] H. Berger, H. Tang, F. Kevy, J. Cryst. Growth 130 (1993) 108

[2] S. P. S. Porto, P. A. Fbeury, T. C. Damen, Phys. Rev. 154 (1967) 522

[3] S. C. Pillai, P. Periyat, R. George, D. E. McCormack, M. K. Seery, H. Hayden, J. Colreavy, D. Corr, S. J. Hinder, J. Phys. Chem. C 111 (2007) 1605

[4] Y. Cong, J. Zhang, F. Chen, M. Anpo, J. Phys. Chem. C 111 (2007) 6976

[5] D. Bersani, P. P. Lottici, X. Ding, Appl. Phys. Lett. 72 (1998) 73

[6] E. Gyorgy, A. P. D. PinoP. Serra, J. L. Morenza, Applied Surface Science 186 (2002) 130

[7] Y. Cheng, B. K. Tay, S. P. Lau, H. Kupfer, F. Richter, Journal of Applied Physics 92 (2002) 1845

[8] X. Wang, S. Meng, X. Zhang, H. Wang, W. Zhong, Q. Du, Chemical Physics Letter 444 (2007) 292

[9] Z. Shi, X. Ye, K. Liang, S. Gu, F. Pan, J. Mater. Sci. 22 (2003) 1255

[10] H. Irie, Y. Watanabe, K. Hashimoto, J. Phys. Chem. B 107 (2003) 5483

[11] D. Li, N. Ohashi, S. Hishita, T. Kolodiazhnyi, H. Handea, Journal of Solid State Chemistry 178 (2005) 3293

[12] N. C. Saha, H. C. Tomkins, J. Appl. Phys. 72 (1992) 3072

[13] S. M. Prokes, J. L. Gole, X. Chen, C. Burda, W. E. Carlos, Advanced Functional Materials 15 (2005) 161

[14] Y. Xie, Q. Zhao, X. Zhao, Y. Li, Catalysis Letters 118 (2007) 231

[15] Q. Li, R. Xie, J. Shang, J. Am. Ceram. Soc. 90 (2007) 1045

[16] O. Diwald, T. L. Thompson, T. Zubkov, E. G. Goralski, S. D. Walck, J. T. Yates, J. Phys. Chem. B 108 (2004) 6004

[17] C. Lettmann, K. Hildenbrand, H. Kisch, W. Macyk, W. Maier, Applied Catalysis B: Environmental 32 (2001) 215

[18] R. Nakamura, T. Tanaka, Y. Nakato, J. Phys. B 108 (2004) 10617

[19] R. Asahi, T. Morikawa, T. Ohwaki, K. Aoki, Y. Taga, Science 293 (2001) 269

[20] Y. Cong, J. Zhang, F. Chen, M. Anpo, J. Phys. Chem. C 111 (2007) 6976

[21] D. Li, H. Haneda, S. Hishita, N. Ohashi, Chem. Mater. 17 (2005) 2596

[22] H. tang, K. Prasad, R. Sanjines, P. Schmid, F. Levy, J. Appl. Phys. 75 (1994) 2042

[23] F. B. Li, X. Z. Li, Chemosphere 48 (2002) 1103

[24] A. L. Linsebigler, G. Lu, J. T. Yates Jr., Chem. Rev. 93 (1993) 341

[25] W. Wang, P. Serp, P. Kalck, J. L. Faria, Appl. Catal. B 56 (2005) 305